ELECTRON BEAM MEASUREMENTS OF THE SHOCK WAVE STRUCTURE

PART I

DETERMINATION OF THE INTERACTION POTENTIAL OF THE NOBLE GASES FROM SHOCK WAVE STRUCTURE EXPERIMENTS

PART II

FEASIBILITY OF A MODIFIED ELECTRON BEAM DENSITOMETER TECHNIQUE TO MEASURE DIFFUSIVE SEPARATION IN SHOCK WAVES IN HELIUM-ARGON MIXTURES

Thesis by

Brian T. Barcelo

In Partial Fulfillment of the Requirements

For the Degree of

Doctor of Philosophy

California Institute of Technology

Pasadena, California

1971

(Submitted December 4, 1970)

ACKNOWLEDGMENTS

The author wishes to express his appreciation to his advisor, Professor B. Sturtevant, for his guidance and direction of the present research. His constructive criticism of the original manuscript is also sincerely appreciated. In addition, the counseling of Professors Liepmann, Roshko and Coles is gratefully acknowledged.

Special thanks go to Mr. Eric Steinhilper for his assistance and contribution to the research. In particular, the interaction potential experiments were a joint effort in which Mr. Steinhilper performed most of the Monte Carlo calculations as well as assisting in the experiments. The author appreciates the use of the Monte Carlo computer program formulated by Professor G.A. Bird.

It is a pleasure to thank my wife Gail for her assistance in correcting the manuscript and to Mrs. Jacquelyn Beard for typing the manuscript.

The author is indebted to the California Institute of Technology and the National Aeronautics and Space Administration for their financial assistance. The work in the GALCIT 17-inch shock tube was supported by the National Aeronautics and Space Administration.

ABSTRACT

Shock wave experiments were conducted in the GALCIT* seventeen-inch low density shock tube to measure the interaction potential of the following nonradioactive noble gases: neon, argon, krypton, and xenon. The experimental shock profiles obtained by employing the electron beam densitometer technique were compared to the Monte Carlo numerical simulation of the shock wave structure. The comparison determined the intermolecular potential for these gases, a potential assumed to be of the form $\Phi = \text{const}/r^s$. The values resulting for the free parameter s in the inverse repulsive power law were 9, 10, 11, and 12 for xenon, krypton, argon, and neon, respectively.

In a second phase of the experiments, the feasibility of a modified electron beam densitometer technique was investigated for measuring the shock wave structure in a binary mixture of helium and argon. It was desired to obtain both the argon and helium density profiles through the shock wave by varying the electron beam energy in two experiments of identical shock conditions (gas concentrations, Mach number, initial pressure, etc.). Theoretical calculations of the collision cross-section indicated only a slight possibility of separating the density profiles of

---

*Graduate Aeronautical Laboratories California Institute of Technology.

the two species with the range of electron energy possible in the experimental apparatus (7000 to 15000 volts). Experiments conducted with initial gas concentrations of 10%, 20%, 50%, and 80% argon in shock waves with a Mach number of approximately four confirmed these suspicions but permitted qualitative conclusions in agreement with other similar investigations.

TABLE OF CONTENTS

TABLE OF CONTENTS (cont.)

TABLE OF CONTENTS (cont.)

LIST OF FIGURES

LIST OF FIGURES (cont.)

LIST OF FIGURES (cont.)

I. DETERMINATION OF THE INTERACTION POTENTIAL OF THE NOBLE GASES FROM SHOCK WAVE STRUCTURE EXPERIMENTS

1.1 Introduction

Studies of the structure of a normal shock wave have long been undertaken by a number of investigators. The shock wave suits the purpose of so many investigators because it is the simplest flow in which large departures from equilibrium occur. It is one dimensional, boundary effects are absent, and the nonequilibrium processes occur within a narrow region in space bordered on both sides by areas of uniform flow. Hence the shock wave problem has often served as the test case for new theories and experimental techniques which have the solution of more complex problems as their ultimate goal. Today, many in the area of fluid mechanics concern themselves not with the shock wave itself but rather the far-reaching consequences that can be realized from a more complete understanding of the processes involved. One such field of endeavor is the subject of this investigation, namely the measurement of the interaction potential of the noble gas atoms.

The actual processes which occur within a shock wave involve a transfer of both energy and momentum. An attempt to describe these phenomena in order to develop a theory for the structure (density profile) of a normal shock wave has lead to two distinct points of view (Ref. 1). The

most fundamental approach describes the transfer processes in terms of atomic collisions, hence leads to a formulation based on the kinetic theory. The other approach treats the gas as a continuum with stresses and heat transfer properties governed by laws which describe the relationship between these properties and the gradients of velocity and temperature. Because of the difficulty in solving the Boltzmann equation (necessary to the general kinetic theory solution), the Navier-Stokes approach, continuum theory (Ref. 2), received much of the early attention. This method is sufficient for weak shocks but its validity is doubtful for shocks of arbitrary strengths.

The kinetic theory approach has been complicated by the approximations necessary to solve the Boltzmann equation. The net result is a variety of schemes, the most notable of which are the Chapman-Enskog (Ref. 3), Grad thirteen-moment (Ref. 4), BGK (Ref. 5), and Mott-Smith (Ref. 6) techniques. Recently, a superior method, the Monte Carlo direct simulation (Ref. 7), has been developed which models a gas as a representative sample of particles and calculates the shock wave structure from collision dynamics. Arguments concerning these various approximations have lead to numerous experiments in an attempt to select the most appropriate theory since "the sole test of the validity of an idea is experiment".*

*R.P. Feynman et al., The Feynman Lectures on Physics, v.1, chap. 2, p. 7.

The experiments can be arranged in three groups according to the specific technique employed. The earliest method measures the optical reflectivity of the shock front. This technique developed by Hornig, et al. around 1950 (Refs. 8 - 12) has been used primarily for shock thickness measurements, hence is inconclusive in establishing the best theory for the shock structure. The second method is a hot wire technique initiated by Sherman in wind tunnel experiments of the shock wave (Refs. 13, 14). This approach requires stationary shocks and has been used only for weak shocks in which deviations from the Navier-Stokes theory are small. In addition, all theoretical approximations seem to agree in this region. Finally, there are the electron beam investigations. The earliest experiments in the mid 1950's (Refs. 15, 16, 17) measured the transmission of an electron beam through the shock wave to determine its thickness. Camac (Ref. 18) has measured large angle scattering with a 100 kv electron beam to infer the shock thickness. The use of the technique in the present investigation stems from the experiments of Russell (Ref. 19), Schultz-Grunow and Frohn (Ref. 20), and Schmidt (Refs. 21, 22). These latter two investigations report accurate shock wave density profiles for strengths up to $M_s \simeq 10$. Conclusions based on these experiments recognize the Monte Carlo technique as the most adequate theoretical approach to the shock wave structure problem. In addition, the experiments have

demonstrated the inconclusiveness of shock thickness measurements. Thus, the latest electron beam densitometer technique (with only minor changes in the data reduction procedure) has been chosen in conjunction with the Monte Carlo technique to investigate the interaction potential which accounts for the density profile of the shock wave.

The connection between atomic forces and shock wave structure may not be immediately apparent, but the essential link involves the collisional nature of the shock wave. As a shock propagates, it conveys its presence to the undisturbed gas via collisions, during which "information" is exchanged between the molecules. Since the interaction potential explains the nature of the influence one atom exerts on its environment, it is the basic building block for the shock wave structure.

The present investigation links the two phenomena by experimentally measuring the structure (density profile) of a shock wave in the noble gases (neon, argon, and krypton) and comparing the results with theoretical profiles obtained by a Monte Carlo direct simulation technique developed by G.A. Bird (Ref. 7). In the latter theory the only adjustable parameter is the interaction potential for the gas atoms in the shock wave. However, the analytical expressions used to represent the true potential of the atom, in order to reduce the complications (the collision integrals) involved in computing the scattering process, are not valid

over the full range of intermolecular separations, but rather, can be regarded as approximating the potential, $\Phi(r)$, over a finite range of separation, r . The many attempts to model this potential have resulted in varying degrees of success and complexity. For the present investigation, one of the simpler models, namely the inverse power law of repulsion ($\Phi = c/r^s$) , is chosen with the hope of being able to determine the exponent s for the repulsive potential of the gases tested. This is only one analytical model for the atomic potential, a potential known to include both an attractive and repulsive field, but in the energy range of shock structure measurements it is assumed that the attractive forces would be negligible.

Once the structure of the shock wave has been obtained by experimental measurement and by numerical computations using different power laws for the interaction potential, the resulting profiles can be compared. The similarity between these profiles determines the value of s which best describes the interaction potential of the noble gases considered. These measurements are compared to more conventional determinations of the potential in order to conclude the applicability of the inverse repulsive power law to describe the interaction potential of the noble gases.

As secondary goals these experiments have attempted to evaluate a new data reduction technique which is employed

for greater accuracy, to facilitate data manipulation, and to determine the parameters affecting the shock profile of the monatomic gases. This is done by conducting experiments at various Mach numbers, initial pressures, and test gases. In this connection experiments previously conducted at GALCIT* by Schmidt (Ref. 22) in argon and xenon were reprocessed by the new method and used in the interaction potential calculations. Inclusion of this information completes the list of nonradioactive noble gases except for helium, which presented difficulties in the production of accurate shock profiles at high Mach numbers in the GALCIT facility.

Further significance is attached to the problem because the virial coefficients of the equation of state and the transport properties such as viscosity, thermal conductivity, etc. of a gas at high temperatures depend on the repulsive portion of this intermolecular potential (Ref. 29). These properties are fundamentally important to many areas of science and engineering, yet accurate determination of their values is exceedingly difficult and often impossible to measure directly. Conventional measurements of the interaction potential involve the relationship between Φ and the physical properties of a gas, (Refs. 23 - 28), e.g., by measuring the viscosity of

*Graduate Aeronautical Laboratories California Institute of Technology

a gas the interaction potential can be inferred. Another method determines the potential by measuring the total collision cross-section of a gas from the scattering of high energy molecular beams (Refs. 29 - 35). Therefore, determination of the interaction potential by shock wave structure measurements assumes a more noteworthy role.

The investigation was a joint effort by Eric Steinhilper and the author. It is difficult to completely separate the contributions of each individual, but in this report details of the area in which the author expended most of his effort are presented, leaving all but a brief description (for completeness) of the remainder to the future dissertation of Mr. Steinhilper.

1.2 Experimental and Numerical Techniques

The method employed in this investigation matches the results from an experimental measurement of the shock wave structure to the numerical calculations of the Monte Carlo simulation of the shock wave. This section provides a brief resumé of the fundamentals of these two processes.

By structure of a shock wave one refers to the density variation from the upstream equilibrium state of the undisturbed gas (region 1) to the downstream equilibrium state of the shocked gas (region 2). The measurement of this profile is achieved through the use of an electron beam (Ref. 21). The flow of electrons is directed across the shock tube enabling the beam to encounter the atoms of the test gas. Electron-atom collisions attenuate the source beam proportionately to the density of the gas. The increase in density resulting from the shock wave further decreases the electron beam intensity. Therefore an accurate time history of the attenuated electron current affords the profile desired.

The Monte Carlo direct simulation technique (Ref. 7) models (by a computer) a gas so that it consists of a few thousand discrete particles which obey the laws of kinetic theory. These particles represent the billions of molecules in a real gas. The simulated flow field is divided into numerous cells which are sufficiently small to permit the assumption of constant flow properties within a cell.

In each cell collisions are computed from randomly selected particles (in pairs) with a probability proportional to their relative velocities. After a collision new velocity vectors are assigned in accordance with the kinetics of collisions and a time counter is advanced. Repetition of this procedure continues until the time counter has reached a fraction, Δt_m, of the mean time between collisions. The particles are then moved to new positions calculated from the latest velocity components and the time interval Δt_m.

In the shock structure problem the particles are initially uniformly distributed in space with a Maxwellian velocity distribution. The gas is set in motion at time $t = 0$ by a specularly reflecting plane piston to which is imparted an instantaneous velocity equal to the fluid velocity downstream of a normal shock wave (u_2) having the desired Mach number. The transient effects due to the instantaneous motion of the piston decay, and a steady shock wave appears in the flow.

Clearly the heart of the Monte Carlo calculation is the collision process which is governed by the interaction potential. Hence, different potentials lead to different shock wave profiles. In the present work the exponent s of the inverse power law of repulsion is the parameter which governs the shock structure. The constant c can be calculated from room temperature viscosity data (see section

1.5d) leaving s as the only free parameter. Therefore, a number of shock wave density profiles have been calculated each with a different value of s, and the results compared with the experimental profiles.

1.3 Apparatus

1.3a Shock Tube

The experiments are performed in the GALCIT 17-inch diameter shock tube (see reference 39 for details) which has a conventional high pressure driver section 12½ feet long and a 70-foot test section of stainless steel (Figs. 1,2). Shock waves are produced in research grade neon, argon and krypton (purchased from Matheson Co.) by the bursting of an aluminum diaphragm caused by pressurization of the driver section with helium, nitrogen or a combination of both. The velocity of the wave is determined with an electronic microsecond counter (Hewlett Packard 5233L) which times the passage of the shock front across two thin film heat transfer gauges (described in reference 40), located 50 cm apart near the end of the tube. The Mach number is calculated from the ratio of the shock velocity to the speed of sound of the test gas in the undisturbed region ahead of the shock wave. The initial pressure is measured in a small cylinder (1/1000 the volume of the shock tube) with a 0 to 50 mm Wallace and Tiernan absolute pressure gauge. This cylinder (control volume) provides an easier measurement of the test pressure by increasing the pressure from microns (10^{-3} mm) to mm of Hg (c.f. Boyle's Law, $p_1 = p_2 \, v_2/v_1$).

1.3b Electron Beam

The electron beam densitometer (described in reference 21) is located 48.5 diameters from the diaphragm and 20 cm from the end wall. The beam, produced by a commercial television gun (Superior Electronics S-110E) with a variable acceleration voltage of approximately 5000 to 20,000 volts, enters the shock tube through an injector needle with a diameter of 0.5 mm and is collected on the opposite side by a Faraday cage 2.8 mm in diameter (Fig. 3). The gap between the needle and cage is maintained at 4-5/8 inches and the electron energy is fixed at 15,000 volts for all experiments. Figure 4 shows the circuit diagram of the beam power supply and the cage and needle amplifiers.

1.3c Electronics

The electronics in the experiments, apart from those of the shock wave timing and electron beam devices, involve triggering, monitoring and pulsing of the cage and needle signals. These currents are monitored on three Tektronix oscilloscopes (a dual beam type 555, type 532, and type 647A) which are triggered by an end-wall thin film heat transfer gauge located approximately 6 cm upstream of the electron beam (Fig. 1). After the shock wave passes the measuring station a -40 volt pulse, generated by a Tektronix Pulse Generator (type 161), is applied to the deflector plates of the electron gun thereby causing the entire beam to fall upon the needle. The result is a zero current

reference for the cage signal (see figure 6). In addition, a Tektronix Time Mark Generator (type 180A) concurrently supplies time dots to the latter two oscilloscopes for use as timing references. Figure 5 shows a schematic of the electronics and figure 6 presents typical oscillogram traces (see section 1.5).

1.4 Procedure

1.4a Mach Number and Initial Pressure

Although the major emphasis is an investigation of the intermolecular potential of the noble gases, secondary goals, including the evaluation of a new data reduction procedure, warrant the study of the test gases at various initial pressures and Mach numbers. For neon this includes 0.010, 0.025, and 0.050 torr initial pressures at Mach numbers of approximately 3, 4, 6, and 7; for krypton 0.015, 0.025, and 0.050 torr are used but at Mach numbers of 4, 6, and 8; finally, for argon, primarily for comparison with Schmidt's data (Ref. 22), pressures of 0.025 and 0.050 torr are combined with Mach numbers of 4 and 6. The Mach numbers are nominal values with root-mean-square deviations of ± 0.2 from the values quoted; whereas the initial pressures are exact numerical values. The established method for determining these quantities has been described in section 1.3a.

1.4b Shock Tube Operation

For the various combinations of the above initial conditions, the operational procedure remains unchanged. The shock tube is evacuated to less than 0.05 microns Hg (1 micron = 10^{-3} torr) as measured by a discharge vacuum gauge (Consolidated Electronics Type GPH 100) before releasing the test gas from the control volume, where the initial pressure is determined, into the driven section (see figure 1). A three minute delay time is employed to

insure pressure equilibrium before the manifold valve is closed and the firing sequence initiated. Meanwhile the oscilloscope sensitivity and sweep rates are set and the electron beam filament activated. After the requisite interval, the beam is aligned for maximum cage current output at an acceleration voltage of 15,000 volts and a cathode current of approximately 100 μa . The diaphragm is ruptured by the high pressure driver gas (usually helium or nitrogen) and the resulting shock wave triggers the oscilloscope sweeps upon contact with an end-wall thin film heat transfer gauge mounted just upstream of the measuring station. Simultaneously, two 20-volt gate pulses from the 555 oscilloscope disengage the electron beam (after a predetermined delay) and close a ball valve, thereby preventing the high pressures of the shock wave from harming the sensitive elements of the electron gun. Meanwhile, the three oscillograms are photographically recorded on polaroid film and other pertinent beam and shock wave information noted. The venting of the tube and a diaphragm change completes the cycle.

1.5 Data Reduction

Each of the oscillograms displayed in figure 6 contains information necessary for conversion of the current history of the Faraday cage into a shock wave density profile. Figure 6a is a typical recording from the dual beam oscilloscope. The upper trace exhibits the current output from the Faraday cage from 15 to 40 microseconds before the arrival of the shock wave until approximately 20 microseconds after its passage. The lower trace contains the needle current output over that same time interval (the two traces are shifted one cm to avoid confusion). If a spurious signal has developed long before the shock arrival and caused erroneous data to be collected, a glance at these signals will indicate the trouble. In addition, the source current I_0 can be computed from the needle signal since the deflection seen corresponds to the total current emitted through the needle injector.

The 532 oscillogram (Fig. 6b) is a more detailed picture of the cage output and its sole function is the establishment of the zero reference from which all currents (in particular, those of oscillogram c) are measured. Shortly after the passage of the shock wave, the entire electron beam is deflected onto the needle thereby "chopping" the cage signal and recording the zero current level.

Finally, the third picture (Fig. 6c) is a close-up of the shock structure because it depicts the fine detail which

is converted into the shock wave density profile.

1.5a Digitization

Processing begins with the digitization of the current data (Fig. 6c). A new technique has been devised for this purpose which replaces an older method of reading the magnitude of the current at various intervals along the horizontal or time axis with a millimeter scale and magnifying glass. Obviously, this technique has inherent errors, not the least of which is due to eye fatigue, whereas the new scheme is quite accurate yet compatible with existing equipment.

The ideal process would be fully automatic with both the x and y coordinates of various points along the oscillogram trace being electronically recorded. Such a system is quite possible but expensive. Therefore a simpler but somewhat less satisfactory device has been employed which uses an x-y plotter (Hewlett Packard Mosely Recorder, model 7004B) "in reverse". Two potentiometers provide a continuous input voltage of 0 to 9 volts (an arbitrary range selected for convenience) to the x and y terminals of the device. By the proper selection of these voltages, the recorder pen can be positioned at any desired location. Accuracy in placement is achieved by removal of the standard pen and insertion of a cross hair arrangement constructed exclusively for this purpose. Thus, the oscillogram trace can be followed easily with the cross hairs and recordings

made of the x and y voltages, i.e., the x and y coordinates of various points across the picture. The actual recording unit is a multiplexer-voltmeter-printer combination* which alternately switches the voltages on the x and y inputs to a Hewlett Packard Multifunction Meter #3450A, that measures the voltages which are then printed by a Hewlett Packard Digital Recorder #5050B.

Any point on the oscillogram can be read to ± 0.01 volts (corresponding approximately to a time of ± 0.02 microsecond or a distance of ± 0.03mm and an electron beam deflection of $\pm 0.13\%$ of I_1-I_2) as has been verified many times by re-checking the coordinates of each time mark on figure 6c. Therefore the accuracy of digitizing the center of the current traces is better than 0.2% of full scale. This accuracy is achieved only in reading the picture and does not account for oscilloscope nonlinearity or errors in the measuring (electron beam) apparatus.

In addition to the electron beam deflection, the time marks concurrently generated on oscillograms b and c facilitate establishment of the absolute current level for the digital information. After the primary picture (Fig. 6c) has been digitized with approximately 40 points, special attention being given to the time dots, i.e., checking these points twice, a similar procedure is applied to the second oscillogram. In this instance however, only the

*Designed and constructed at GALCIT by Dr. G.L. Brown and Mr. P.E. Dimotakis.

y coordinate relative to the zero current line of each time mark is necessary, since the time dot interval determines the x coordinate. Coupling similar data points from the two oscillograms in such a manner that all possible pairs are compared, special weight being given to those farthest apart, produces the scaling or magnification factor with which the digital information of the third trace can be referred to the zero current. The determination of the scaling along with the remainder of the data reduction process is programmed for an IBM 360/75 computer.

1.5b Selection of I_1 and I_2

After all the data have been referred to the absolute current level, the currents at the two equilibrium states of the shock wave (I_1 and I_2) are determined. The first of these presents no difficulty since the signal is always well stabilized before the shock wave arrives at the beam. Hence I_1 is chosen as the magnitude of the upper plateau on figure 6b as indicated.

The second equilibrium state is not so easily identified (Fig. 6), due to the density rise behind the shock (believed to be caused primarily, by a boundary layer effect described in reference 19). Again a new technique is applied to this critical step in the processing. Experience has shown that scatter is reduced if a straight line is drawn through the rear portion of the shock wave and I_2 is labeled as the point at which this line deviates from

the actual trace (Ref. 21). This is, however, something of a subjective decision. Therefore a technique has been devised to allow an impartial judge, the computer, to select I_2.

The method attempts to determine the first significant deviation of the current trace from the assumed linear behavior at the rear of the shock wave. This is accomplished by least-squared curve fitting a straight line to the last few data points obtained from figure 6c, and arbitrarily selecting a region outside of which is considered to be a significant departure from the line. The intersection of the actual current trace and this bandwidth is taken as I_2.

In the program the last four data points of figure 6c are used in a least-squared curve fit to a straight line. To these original points earlier data are added until the deviation of a new point is larger than the sum of the maximum deviation of the curve (the distance to the farthest point from this line) and one third of a trace width. The program computes other first degree polynomials with each new data point and permits one of the original data points to be discarded from the computation for each two new points added. This provision allows greater flexibility in determining the best straight line by preventing any one of the original four points which may have a large deviation from impairing the calculations. From various combinations of the old and new data points numerous straight lines are

calculated and one is selected on the basis of smallest standard error (rms deviation) and maximum number of points. Around this curve a bandwidth equal to the rms deviation or one third of a trace width, whichever is largest, is projected. I_2 is then chosen as the point where the actual trace crosses the bandwidth of the fitted curve. Through many trials this method has been found to best represent the correct value of I_2 based on comparison with previous data.

1.5c Determination of Density Profiles

Once I_1 and I_2 have been determined, the digital current data are converted to density ρ using the attenuation law

$$I = I_o \exp(-K\rho) \qquad (1.5\text{-}1)$$

where K, a coefficient which depends on test gas, electron energy, etc. can be considered a constant for the present application.

Combining the above equation with the knowledge of I_1 and I_2 and the result (ρ_2/ρ_1) from the Rankine-Hugoniot relations for the density jump across a shock wave yields after some rearranging

$$\bar{\rho} \equiv \frac{\rho - \rho_1}{\rho_2 - \rho_1} = \frac{\ln(I/I_1)}{\ln(I_2/I_1)} \quad . \qquad (1.5\text{-}2)$$

Finally, the x voltages in the digital array are converted to physical times by interpolating between the time marks (Fig. 6c) which are a known time interval apart (generally 5 microseconds), and extrapolating to points outside the first and last time dots. A Galilean transformation using the shock wave velocity is applied to establish the distance axis ($x = Ut$), which is then normalized with the mean free path* λ of the test gas in the undisturbed region ahead of the shock wave, i.e., region 1. For convenience this scale is arbitrarily shifted so $x/\lambda_1 = 0$ corresponds to $(\rho - \rho_1)/(\rho_2 - \rho_1) = .5$.

1.5d Determination of the Constant and Exponent in the Inverse Power Law

In the Monte Carlo direct simulation of the shock wave structure the only free parameter is the interaction potential, $\Phi = c/r^s$. The explicit parameter s is a measure of the hardness or softness of the atoms and is adjustable, whereas c, an implicit parameter, does not appear in the calculations because of an energy normalization. The net result is a numerical solution which is independent of all gas properties except s (and the ratio of specific heats γ which has the monatomic gas value of 5/3).

* $\lambda = 16/5\sqrt{\gamma/2\pi}\ \mu/\rho a$
where μ, a, and γ are the viscosity, speed of sound, and specific heat ratio of the test gas respectively.

In the experimental shock wave structure data reduction procedure, distances are normalized with the upstream mean free path of the gas under investigation. This transport distance is a function of c and s. Therefore once s is determined, c is fixed.

The comparison of the experimental and numerical results determines the value of s. Then c can be evaluated using the equation (Ref. 24) for the viscosity of a pure gas, in which the atoms are considered point centers of repulsion, i.e.,

$$\mu = \frac{5}{8}\sqrt{\frac{km}{\pi}}\left(\frac{k}{sc}\right)^{\frac{2}{s}} T^{\left(\frac{1}{2}+\frac{2}{s}\right)} / \Gamma\left(4 - \frac{2}{s}\right) A^2(s) \quad (1.5\text{-}3)$$

where μ = viscosity (gm/cm/sec)

m = mass of the atom (gm)

k = Boltzmann constant (ergs/^{o}K)

T = temperature (^{o}K)

Γ = the Gamma function

$A(s)$ = a dimensionless quantity

The above equation can be rewritten in terms of the constant c and evaluated using room temperature viscosity data (Ref. 41).

1.5e Calculation of Closest Approach

The evaluation of the constant c in the point centers of repulsion model for the atomic interaction potential determines one point, the intercept, on a log log plot of

Φ versus r. A determination of the exponent s (from matching the numerical and experimental results) yields the slope of such a curve but does not give an indication of the range of validity, i.e., the values of Φ which correspond to the energy range found in the shock wave. The most obvious choice is obtained from the temperature jump across the shock wave, i.e., $3/2\ kT_1 \leq \Phi \leq 3/2\ kT_2$. Since $\Phi = \Phi(r)$, an alternate estimate can be made on the basis of the range of values of r which occur in a shock wave. The distance of closest approach of two atoms in a collision is taken as a characteristic value of r since the true values for each collision extend from $-\infty$ to $+\infty$. Thus a distribution of values of closest approach is, in essence, an energy distribution for the shock wave.

The elimination of time from the equations of motion is the first step in obtaining the point of closest approach r_m since the resultant equation is an analytical expression for the rate of change of r with respect to θ, the angle between the two approaching atoms. The conservation laws of a two body collision for a center of mass coordinate system (see schematic below) can be written as

$$\frac{1}{2}m^*\dot{r}^2 + \frac{1}{2}m^*\dot{r}^2\dot{\theta}^2 + \Phi(r) = \text{constant} = \frac{1}{2}m^*v_r^2 \quad \text{(Energy)} \tag{1.5-4}$$

$$m^*r^2\dot{\theta} = \text{constant} = m^*bv_r \quad \text{(Angular Momentum)}$$

where m^* = reduced mass

v_r = relative velocity

b = impact parameter

$\dot{}$ = d/dt.

Combining these equations yields (taking the negative square root)

$$\frac{dr}{d\theta} = \frac{\dot{r}}{\dot{\theta}} = -\frac{r^2}{b}\sqrt{1 - \frac{\Phi(r)}{\frac{1}{2}m^* v_r^2} - \left(\frac{b}{r}\right)^2} \qquad (1.5\text{-}5)$$

and thus the solution of $dr/d\theta = 0$ gives the desired result, r_m.

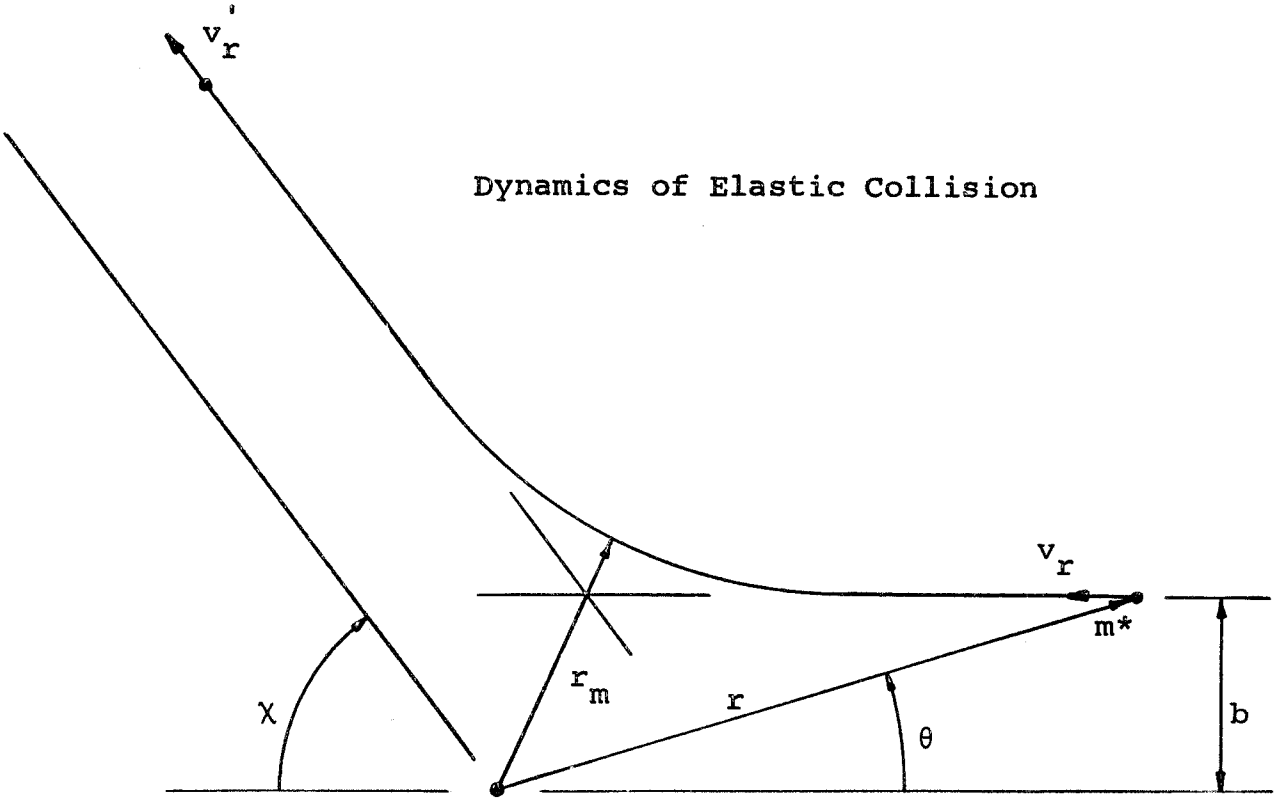

Dynamics of Elastic Collision

In the Monte Carlo calculations the values of v_r, b, m*, and Φ are known for a given collision, hence a record of the point of closest approach can be obtained for all collisions. Due to the large difference in mean collision energy of the gas atoms before and after the passage of the shock wave, two segments of the shock profile are arbitrarily selected, one near the front and one near the rear, to give a statistical distribution of the number of collisions which resulted in a given r_m. The resultant distributions (Fig. 7) contained maxima, presenting two possibilities for the range of validity of the inverse repulsive power law. One is the values of r between the two maxima (solid line in figures 22 - 25); whereas the other is the values between the half-width of each distribution curve (dashed line in figures 22 - 25).

1.6 Results

Before discussing the final results, it is worth establishing the trends and accuracy of the experimental shock structures for the four noble gases considered. In all cases the curves shown are averages of a number of runs conducted under identical conditions, and the indicated bandwidth, which represents scatter, is the rms (root-mean-square) deviation.

1.6a Pressure Effects

The influence of initial pressure is illustrated in figures 8, 9, and 10. On the low density side of the shock wave there are no discernible trends and all curves fall within experimental accuracy. However, a relationship between pressure and the density profile on the downstream side of the shock is evident. As the initial pressure increases, the density approaches a uniform asymptotic state in agreement with the assumption of an ideal normal shock. Since the selection of condition 2 (section 1.5b) is more accurate when the density profile approaches a constant value, a high initial pressure yields results with less scatter.

It is believed that this density rise is due to a boundary layer affect which results in a curved shock front (Ref. 19). Unfortunately, calculations based on this principle do not account for the total observed effect but do predict the above-mentioned dependence on pressure (Ref.42).

1.6b Experimental Scatter

Typical examples of the scatter of experimental results in neon, argon, and krypton are shown in figures 11, 12 and 13 respectively. The significant feature of these curves is the relationship between scatter and the length of the downstream tail of the shock wave (figure 11). The density profile of the Mach 3 shock wave extends five mean free paths downstream of $x/\lambda_1 = 0$ and has a larger scatter band than the Mach 6 shock wave structure, which extends well beyond $x/\lambda_1 = 8$. In order to select an accurate value for the downstream equilibrium state, the computer must fit a first degree polynomial to this rear portion of the shock wave (section 1.5b). If the length of this region is too short, i.e. the electron beam is deflected too soon after shock passage, the value selected is generally lower than would otherwise be the case. Thus, erroneous determination of ρ_2 for such runs results in somewhat increased scatter.

This result is further illustrated in figures 12 and 13. The scatter shown is the rms deviation for 9 and 6 experiments, respectively, conducted at a fixed Mach number but various initial pressures.

1.6c Mach Number Effect

Previous theoretical models have investigated the effect of Mach number on the structure of a shock wave by studying the normalized inverse shock thickness (λ_1/δ_s) .

The Navier-Stokes, BGK, and Mott-Smith models all indicate a maximum in λ_1/δ_s between $M_s = 3$ and $M_s = 5$ (Ref. 21).

In the present experiments the Mach number trends for neon, argon and krypton are shown in figures 14, 15 and 16 respectively. The effects are small and in some cases less than the experimental scatter (especially near the downstream tail of the shock wave). Unlike the figures showing the effect of initial pressure, these results show a definite trend on the low density side of the shock wave; in all cases the shock seems to exhibit minimum thickness at approximately $M_s = 4$. However λ_1/δ_s values scatter wildly between 0.25 and 0.35, the same range as other experiments (Refs. 9 - 21), for Mach numbers between 3 and 8, demonstrating the inability to arrive at definite conclusions on the evidence of shock thickness measurements alone.

1.6d Comparison of Numerical and Experimental Shock Profiles

The experimental shock wave structure curves for neon, argon, krypton, and xenon (both argon and xenon data were obtained from reference 22) are compared with the Monte Carlo numerical simulation of a Mach number 8 shock wave with values of 8 and 11 for the inverse repulsive potential exponent s (Figs. 17 - 20). The experimental shock profiles are the averages of numerous results from Mach 8 shock waves of varying initial pressures for all cases except neon. For neon the data shown (Fig 17) display the

average results for both Mach 6 and Mach 7 shock waves. Since the Mach number effect is only slight, the $M_s = 7$ curve is considered close enough to the desired Mach number to be used. In addition, the $M_s = 6$ profile provides a reference for extrapolating to the Mach 8 shock wave structure and affords an intuitive feeling for the accuracy of the conclusions drawn from the $M_s = 7$ curve.

The relative positions for the experimental and theoretical curves are set such that the areas between them, to the right and left of their intersection (usually occurring near $x/\lambda_1 = 0$) are approximately equal. There is no strict procedure for assigning the position; rather, the method is somewhat intuitive. From these superimposed curves the experimental value of s is determined with the accuracy indicated in the table; the accuracy is estimated from the similarity between the experimental and numerical curves and the resulting ease in positioning the curves.

Gas	(Mol. Wt.)	s	Accuracy	Viscosity*
neon	(20.14)	12	±1	$\mu \sim T^{0.67}$
argon	(39.95)	11	±½	$\mu \sim T^{0.68}$
krypton	(83.80)	10	±½	$\mu \sim T^{0.70}$
xenon	(131.30)	9	±1	$\mu \sim T^{0.72}$

*The temperature dependence of viscosity is calculated from equation 1.5-3 and the value of s.

Comparison of the shock structure curves for the four noble gases is shown in figure 21. All but neon are for Mach = 8 shock waves and the $M_s = 7$ shock for neon is again close enough for illustrative purposes. Variance of the thickness with atomic number results from the relative hardness or softness (i.e., s) of their interaction potentials, since the mean free path dependence has been removed through normalization. The trend of this thickness is in accord with the principle that hard sphere molecules ($s = \infty$; $\mu \sim T^{\frac{1}{2}}$) have the thinnest structure, whereas Maxwellian molecules ($s = 4$; $\mu \sim T$) are the opposite limit. Hence the noble gas results fall between these two limits according to their potential exponent s .

1.6e Interaction Potential

Finally, figures 22, 23, 24, and 25 present plots of the interaction potential Φ versus the interatomic separation r for the four noble gases. In addition, these figures include the previous work of other investigators (Refs. 23 - 38); the high potential results are generally from high energy molecular beams, whereas the lower curves result from viscosity and other low temperature data. The present results fall in an energy range between those of the previous investigations and thus serve as a basis for interpolation between the high and low potential data.

1.7 Discussion

1.7a Experimental

In Section 1.5a it is stated that the digitization process, i.e., the "reading" of the oscillograms, is accurate to 0.2% of full scale, a claim based on the ability to repeatably measure a given deflection of the current trace. This accuracy eliminates "picture reading" as a major source of error, but obviously does nothing to alleviate other experimental errors.

Schmidt claims (Ref. 21) that assignment of ρ_2 to the point at which the curved trace merges into a linear increase at the rear of the shock wave reduces scatter. The present method of data reduction employs the same idea, but uses an IBM 360 computer to select the point of merging. The small experimental scatter observed in figures 12 and 13 serves as substantial evidence for this claim, despite the noticeable variation of scatter with the length of the measured downstream tail of the shock profile, initial pressure, and test gas. The effects of variations in initial pressure and the length of this tail are discussed in sections 1.6a and b respectively; any further comments will be limited to the effect of varying the test gas and its relation to initial pressure.

The choice of test gas has some effect on error because of differing electron-atom scattering cross-sections. The signal to noise ratio is low in the case of small electron

scattering by light gases such as neon. Experimental scatter in argon and krypton are comparable. Fortunately, an increase in initial pressure or Mach number can be used to compensate for decreased scattering in neon by producing a denser sample and, consequently, more beam attenuation. On the other hand, if the collision cross-section is too large, multiple scattering complicates the calibration procedure. However, the lack of dependence on initial pressure is reason to believe that this does not occur to any significant degree and, in fact, conditions are maintained such that total attenuation of the beam is generally a small percentage of the current emitted from the needle.

Ionization due to the high temperatures present in some strong shock waves must also be avoided since it would lead to a spurious collector (Faraday Cage) current, and thereby invalidate the assumed attenuation law. This effect is relatively small in most gases if the Mach numbers are less than 8. In krypton, however, it is noticeable even when $M_s = 8$ and the initial pressure is 0.050 torr or greater. Therefore, this condition has been excluded from the final results.

Attention should also be directed to the value of K in the attenuation law $I = I_0 \exp(-K\rho)$. It has been assumed that this parameter is independent of all shock wave variables except test gas. (A full discussion of K is found in references 21 and 43). To test this hypothesis

the calibration constant is evaluated in two ways, statically and dynamically. The static calibration is performed in the test section of the shock tube by measuring the beam attenuation at various densities. Such tests have been conducted in helium, neon, argon, and krypton (Fig. 26). The helium and neon calibrations demonstrate K to be a constant; whereas the argon calibration shows K to be double-valued. The krypton calibration has a similar behavior but the change of slope occurs at a higher pressure, above approximately 190 μ Hg (not shown in figure 26). More static calibrations are necessary to establish the exact pressure at which the slope changes for krypton. Admittedly the "knee" in the curves is puzzling and believed attributable to a high pressure effect (Ref. 21) but the lack of dependence of shock wave structure on initial pressure is reason to believe the discrepancy is unimportant.

The second method of obtaining the constant comes from using the values of I_1 and I_2 at the two equilibrium states ρ_1 and ρ_2 with the attenuation law equation, i.e.,

$$K_{Dyn.} = \frac{1}{\rho_2 - \rho_1} \ln \left(\frac{I_1}{I_2}\right) \qquad (1.7\text{-}1)$$

Although the density normalization (Eqn. 1.5-2) eliminates the calibration constant from the calculations, it assumes that the value of K is a constant. A comparison of the static and dynamic calibration constants provides another

check on this hypothesis.

All experiments included in the final results are those in which the downstream tail of the shock wave is of sufficient length to produce a reasonable value of ρ_2. The initial pressure, Mach number, and test gas combinations are chosen to eliminate erroneous electron beam signals caused by ionization and multiple scattering; and all runs have been discarded which possess a large difference (approximately 25%) in the static and dynamic calibration constant.

1.7b Numerical Simulation

A few comments will be made concerning the Monte Carlo calculations, but a general discussion may be found in reference 7. When the steady shock wave has formed (see section 1.2), the density profile is obtained by sampling the number density in the various cells, i.e., at different locations. The error in this profile is the statistical uncertainty ($dn/n = d\rho/\rho$) which is proportional to $\pm 1/\sqrt{N}$ where N is the number of sampled particles. Increased accuracy is achieved by averaging such profiles at subsequent time intervals. Since each calculation requires a large amount of computer time, the operational cost becomes one limit on the accuracy of the structure.

Error bars included on figures 17 through 20 represent the error in density near the front and rear of the shock wave. The significant feature is the increase in error

near the high density region of the shock wave. This occurs because the normalization multiplies the error in density $(d\rho/\rho)$ by $\rho/(\rho_2 - \rho_1)$. Hence for ρ near ρ_1 the error is approximately 1/3 the statistical uncertainty, whereas near ρ_2 the error is 4/3 this uncertainty.

1.7c Interaction Potential

The ultimate goal of this work is a first attempt to measure the characteristics of the interaction potential of the noble gases using the shock wave structure. The inverse repulsive power law as a model for the interaction potential has limited applicability, but it is a successful first approximation for the noble gases within a molecular separation distance of approximately 2.0 Å - 3.9 Å as illustrated in figures 22, 23, 24, and 25. None of the potentials for these gases is valid for the full range; rather neon is valid from 2.0 Å to 2.6 Å, argon from 2.6 Å to 3.2 Å, krypton from 2.5 Å to 3.2 Å, and xenon from 2.8 Å to 3.9 Å. This is not the range of validity discussed in section 1.5e but is instead that which agrees with previous investigations. However, the range of validity based on the maxima of the closest approach distributions (see section 1.5e and figure 7) is generally included in these ranges. Krypton is an exception as seen in figure 24.

The present results for neon agree best with previous results; agreement becomes somewhat worse with increasing atomic number. The reason for this is simple. The inverse

repulsive power law neglects all attractive forces. It is known that the potential well exhibited by all atoms increases with atomic number; hence the shallow well of neon indicates dominance of the repulsive forces and the best experimental result. It is also clear from comparison with other investigations that the linear (on a log log scale) inverse power law cannot explain the potential exactly.

In the final analysis it is interesting to note that the shock structure measurements fall into the range of energy difficult to obtain from more conventional measurements. This allows greater accuracy in interpolating between the previous low energy data and the high energy molecular beam data.

1.8 Conclusion

This investigation has been undertaken with two primary aims; to establish the validity of a new data reduction technique for measuring the shock structure of the noble gases and to determine the inverse power law best describing the interaction potentials of these gases. While attaining the former goal, experiments were conducted at various Mach numbers and initial pressures. The results show the shock structure to be independent of p_1 in the pressure range between 0.010 torr and 0.050 torr. There is a slight Mach number effect with the thinnest shock wave occurring at approximately $M_s = 4$. In general the root-mean-square deviation of a number of profiles conducted at a fixed Mach number in the same test gas is ± 0.07 mean free path or equivalently $\pm 2\%$ of the shock thickness.

The inverse repulsive power law has been shown adequate as a first approximation to the true interaction potential of the noble gases in the approximate energy range of 0.04 ev to 1.0 ev. The exponents of this power law which best describe the interaction potential of xenon, krypton, argon, and neon as determined from the shock structure measurements are 9, 10, 11, and 12, respectively. The neon results agree best with previous results; agreement becomes somewhat worse with increasing atomic number.

II. Feasibility of a Modified Electron Beam Densitometer Technique to Measure Diffusive Separation in Shock Waves in Helium-Argon Mixtures

2.1 Introduction

The basic aspects of the structure of a shock wave of moderate strength in the noble gases are for all practical purposes fully understood. These are, as can be expected, the least complicated shock waves imaginable because of the relative inertness, reluctance toward ionization, and monatomic nature of the fluid. In an attempt to expand upon this knowledge, researchers are seeking a similar understanding of the problem of a shock wave propagating into a binary mixture of gases.

The fascinating possibility that a shock could occur for each mixture component was probably a driving force in the early investigations. Although this was not to be, the theoretical work of Cowling (Ref. 44) in 1941 predicted that diffusion would be as important as the other dissipative forces in a shock wave provided the two gases had a large difference in molecular weight. Diffusion occurs in a shock wave because of the large pressure gradients present. The lighter molecules diffuse down this pressure gradient, and therefore concentrate near the front (upstream region) of the wave, creating a difference in composition throughout the shock. Although the large temperature gradients are attempting to negate this effect, thermal

diffusion is known to be much smaller than baro-diffusion. In 1959 Sherman (Ref. 45) demonstrated the slight diffusive separation of the two components in a helium-argon shock wave by numerically solving the equations of motion assuming a Navier-Stokes approximation. The solution substantiates the argument that the baro-diffusion forces create the separation; hence, in a helium-argon mixture the helium density profile is ahead of the argon one. In addition, the numerical solution indicates a velocity overshoot of the heavy molecules at low heavy gas initial concentrations. This anomaly, which Sherman himself doubted on the basis of plausibility, became the center of attention for the next few years.

After more detailed analyses using a kinetic theory approach, namely, the Mott-Smith (Ref. 46), Chapman-Enskog (Ref. 47), BGK (Ref. 48), two-fluid (Ref. 49), and velocity moment (Ref. 50) techniques, in addition to the Monte Carlo (Ref. 51) method, produced no velocity overshoot, the experimentalists attacked the problem. The early experiments of Rothe (Ref. 52) in 1966 using an underexpanded free jet were inconclusive due to lack of one-dimensionality, but those of Center (Ref. 53) in 1967 employing the flow near the exit of a Mach 2 nozzle seemed to favor the kinetic theory viewpoint (i.e., no overshoot was observed). In both cases the electron beam fluorescence method was used as the

diagnostic tool in a helium-argon mixture. Harnett (Ref. 54) in 1969 introduced an electron beam spectroscopic technique for measuring simple moments of the velocity distribution functions of an excited helium-argon mixture in flows at the exit of a Mach 1.5 nozzle. In all cases the diffusive separation was observed with the helium molecules leading the argon, but there was no evidence of a velocity overshoot. Finally, Beylich (Ref. 49) in 1968 attempted to use the fluorescence technique in a shock tube with a hydrogen-nitrogen mixture. Because of the long sampling time inherent in the method, Beylich was forced to run twenty duplicate experiments to obtain his data. In addition, the weak signals required the use of an easily excited gas such as nitrogen and hence only the structure of the heavier component in the H_2-N_2 mixture could be observed.

The present investigation has been undertaken to determine the feasibility of a new technique in measuring the separation phenomena. Its main advantage over the other methods is its simplicity and adaptability to high Mach number experiments (however, for the sake of comparison only low Mach number experiments are conducted) which can be performed in shock tubes. As mentioned above the only previous shock tube experiments have had only limited success so a new method is definitely warranted. A modified

version of the electron beam densitometer is the basis for the method because of the proven accuracy of this technique.

2.2 Modified Electron Beam Densitometer Technique

The principle of the electron beam densitometer is the scattering of a beam of electrons by collision with gas molecules. Clearly, as the density of the gas increases, more electrons are scattered from the original beam; hence, by monitoring the electron current through a gas sample the density of this sample can be determined as a function of time. In addition, the scattering process is a function of the electron energy since the collision cross-section of the gas molecules depends upon that energy. This becomes the basis for the modification necessary to obtain the structure of a shock wave in a binary mixture.

Consider the effects on an electron beam in a mixture composed of helium and argon molecules. Both types of particles scatter electrons in a proportion determined by the concentration and collision cross-section of each species. However, the concentration of a given gas is influenced only by the shock wave, whereas the cross-section is governed by the electron beam energy. If two beams of different energies are passed through the same shock wave, a difference in attenuation will result from the change in the cross-sections. It should therefore be possible to recombine these two signals in such a manner that the density profiles of the individual species can be separated.

The interesting cases, according to gas dynamic theory, occur when a mixture is composed of two gases which vary greatly in molecular weight. The above technique requires gases that have large cross-sectional variations with electron energy. These requirements plus the previous work done on the helium-argon system lead to its selection in the experiments which follow.

2.3 Theoretical Considerations

The basis of the modified electron beam densitometer technique is the variation of atomic cross-section with electron energy; therefore an understanding of cross-sections is essential to the utilization of the technique. In addition, the investigation of other parameters which might be important in converting the experimental data, the two attenuated electron beam signals (collector currents), to helium and argon density profiles is desirable.

The steps in the theoretical investigation are the derivation of the equations necessary to separate the density profiles of the individual species from the collector currents, calculation of the cross-sections for the energy range available with the experimental apparatus, and correlation of the cross-section data with the structure of a shock wave in a given helium-argon mixture (obtained from other investigations) to predict theoretically the differences in the collector currents. This procedure serves the two-fold purpose of determining "a priori" the feasibility of the electron beam densitometer technique in separating the helium and argon density profiles as well as presenting guides for analyzing the final experimental results.

2.3a Equations for the Helium and Argon Density Profiles

Following a derivation similar to that for a single gas (section 1.5c), the attenuation of an electron beam by

a mixture of helium and argon atoms is written

$$I = I_o \exp\left(-K_{He}\,\rho_{He} - K_{Ar}\,\rho_{Ar}\right) \qquad (2.3\text{-}1)$$

where I = collector current

I_o = source current

K = calibration constant

ρ = density.

The calibration constants, K_{He} and K_{Ar}, are related to the collision cross-sections of the atoms (see section 2.3c). Writing equation 2.3-1 for the two electron beam energies (denoted by ' and ") and coupling these equations with conditions in the upstream equilibrium region of the shock wave yields, after some rearranging,

$$\begin{aligned} \ln\,(I/I_1)' &= -K'_{He}\,(\rho-\rho_1)_{He} - K'_{Ar}(\rho-\rho_1)_{Ar} \\ \ln\,(I/I_1)'' &= -K''_{He}\,(\rho-\rho_1)_{He} - K''_{Ar}(\rho-\rho_1)_{Ar} \end{aligned} \qquad (2.3\text{-}2)$$

This set of equations can be solved for the unknowns $(\rho-\rho_1)_{He}$ and $(\rho-\rho_1)_{Ar}$ provided the determinant of the coefficients is non-zero. A second system of equations using the downstream equilibrium values ρ_2 and I_2 in place of ρ and I can also be solved for the normalization parameters $(\rho_2-\rho_1)_{He}$ and $(\rho_2-\rho_1)_{Ar}$. The combined expression for the normalized density of argon in terms of

the electron beam currents becomes

$$\left[\frac{\rho-\rho_1}{\rho_2-\rho_1}\right]_{Ar} = \frac{K''_{He}\ln(I/I_1)' - K'_{He}\ln(I/I_1)''}{K''_{He}\ln(I_2/I_1)' - K'_{He}\ln(I_2/I_1)''} \quad . \tag{2.3-3}$$

Defining

$$\bar{\rho} = \frac{\ln(I/I_1)}{\ln(I_2/I_1)} \tag{2.3-4}$$

and

$$K_1 = -\frac{1}{\rho_2-\rho_1}\ln(I_2/I_1) \quad , \tag{2.3-5}$$

relations used in the shock structure of a single gas (section 1.5c), the normalized argon density is expressed as

$$\left[\frac{\rho-\rho_1}{\rho_2-\rho_1}\right]_{Ar} = \bar{\rho}' + \frac{\bar{\rho}'' - \bar{\rho}'}{1 - \frac{K''_{He}}{K'_{He}}\frac{K'_1}{K''_1}} \tag{2.3-6a}$$

and similarly for helium

$$\left[\frac{\rho-\rho_1}{\rho_2-\rho_1}\right]_{He} = \bar{\rho}' + \frac{\bar{\rho}'' - \bar{\rho}'}{1 - \frac{K''_{Ar}}{K'_{Ar}}\frac{K'_1}{K''_1}} \quad . \tag{2.3-6b}$$

The quantities $\bar{\rho}'$ and $\bar{\rho}''$ are the normalized densities which would be obtained if the mixture were considered to be a single gas with mean properties; hence these quantities are the analytical expressions for the composite density

profiles. Similarly K_1' and K_1'' are the composite dynamic calibration constants (see section 1.7a). Since the calibration constant of a single gas is a function of the test gas, the subscript 1 is used to refer to the mixture in the upstream equilibrium region of the shock wave where the concentrations of the individual species are known, thus continuing the single gas analogy.

It is convenient to combine the calibration constants or, equivalently, the cross-sections, into a single parameter χ termed the magnification or scaling factor. Hence,

$$\chi_{He,Ar} = \frac{1}{1 - \left(\frac{K'}{K''}\right)_1 \cdot \left(\frac{K''}{K'}\right)_{Ar,He}} \tag{2.3-7}$$

Then the argon and helium density profiles are expressed as

$$\left[\frac{\rho - \rho_1}{\rho_2 - \rho_1}\right]_{Ar} = \bar{\rho}' + \chi_{Ar}\, \Delta\bar{\rho}$$

and (2.3-8)

$$\left[\frac{\rho - \rho_1}{\rho_2 - \rho_1}\right]_{He} = \bar{\rho}' + \chi_{He}\, \Delta\bar{\rho}$$

where $\Delta\bar{\rho} = \bar{\rho}'' - \bar{\rho}'$.

This derivation is subject to the restriction that the determinant of the coefficients in the set of equations 2.3-2 is non-zero, i.e.,

$$\frac{K'_{He}}{K''_{He}} \neq \frac{K'_{Ar}}{K''_{Ar}} \,. \tag{2.3-9}$$

The functional dependence of the cross-sections with electron energy cannot be the same for the two gases. The magnification factor χ is a manifestation of this restriction (equation 2.3-7) and can be thought of as the "degree" to which equation 2.3-9 is violated.

2.3b Scattering Cross-section

An electron which is incident on a target atom interacts both elastically with the nuclear field screened by the orbital electron cloud and inelastically with the orbital electrons (Ref. 55). The relative importance of these two effects depends on the momentum transferred in a collision. This momentum is related to the electron energy and scattering angle and is expressed as (Ref. 56)

$$q = 2\beta E \sin \tfrac{1}{2}\theta \qquad (2.3\text{-}10)$$

where q = the momentum transferred in units of $m_o c$

m_o = electron rest mass

c = velocity of light

β = v/c

v = velocity of incoming electron

E = the energy of the incoming electron in units of $m_o c^2$

θ = the scattering angle.

For small scattering angles within the orbital electron cloud the inelastic scattering cross-section dominates;

whereas at large scattering angles the inelastic cross-section approaches $1/Z$ of the elastic cross-section (Ref. 55) where Z is the atomic number of the target atom. Thus the differential cross-section may be conveniently expressed in the form (see Appendix A for complete details)

$$\frac{d\sigma}{d\Omega}(\theta) = (d\sigma/d\Omega)_R \left[(1-F(\theta))^2 S_E(\theta) + \frac{G(\theta)}{Z}\right] \tag{2.3-11}$$

where $(d\sigma/d\Omega)_R = 4Z^2 r_o^2 E^2/q^4$, the Rutherford point nucleus differential cross-section

$r_o = \epsilon^2/m_o c^2 = 2.82 \times 10^{-13}$ cm, the classical electron radius

ϵ = electron charge

$F(\theta)$ = atomic form factor

$G(\theta)$ = contribution due to inelastic scattering

$S_E(\theta) = 1-(q/2E)^2$, electron spin effect*.

*$S_E(\theta)$ is obtained from a comparison between the Rutherford differential cross-section for non-relativistic electrons and the Mott-Born cross-section (Ref. 56) for relativistic electrons. Although $q/2E$ makes a negligible contribution to the total cross-section for the experimental energy range of this investigation, the term has been included for completeness.

In principle, if the atomic structure (electron distribution) of the atom is known, the various form factors can be calculated. Because of the complex nature of most atoms, however, the electron distribution is difficult if not impossible to obtain. Therefore various models have been employed in an attempt to account for the screening which the atomic electrons produce as they shield the nucleus from the incoming electron. As the energy of the incoming electron increases, a point will be reached where the electron is able to penetrate the atomic electron cloud and render the screening ineffective. In this energy region $F(\theta)$ must go to zero and at still higher energies the electron will be close enough to the nucleus for the nuclear structure and magnetic moment to become significant. Hence $F(\theta)$ is only important in the energy range where the momentum transfer is small, e.g., $q < 1$.

There are three models commonly used to account for the screening phenomena. The simplest and least accurate is that of exponential screening (Ref. 56). In this model the scattering potential of the atom is assumed to be exponential in nature with the power of the exponential dependent on the atomic number. The second method incorporates the Thomas-Fermi statistical model (Refs. 57, 58) of the atom in which the electrons are assumed to have a smooth charge distribution. Molière (Ref. 59) approximated the screening function of the Thomas-Fermi model with a

series and obtained an analytical expression for $F(\theta)$ which is relatively easy to evaluate but is accurate only for intermediate values of q. It is particularly poor at large distances, where the scattering angle and q are small, and at very small distances, where the scattering angle and q are large (Ref. 56). Finally, there is the Hartree-Fock independent particle model (Ref. 60). As the name implies, this method attempts to account for the effects of the individual atomic electrons by supposing that each electron is in the field of the nucleus plus an average field of the other electrons. The atomic wave functions and potentials obtained for this system must be calculated from Hartree's self-consistent field equations; hence, this method is the most complex to evaluate, often requiring numerical integrations. However, it is the most accurate, and, fortunately, Ibers (Ref. 61) has tabulated the atomic form factors for various values of momentum transfer up to $q = 0.058$.

Since the Hartree-Fock model is the most accurate it is employed wherever feasible. In the case of helium, the wave function obtained from the Hartree field equations is simple enough so that the atomic form factor can be obtained in closed form. However, the same treatment is not possible for argon; thus, the tabulated values of Ibers are used up to $q = 0.058$ and thereafter the Thomas-Fermi model with the Molière modification is used. Since the highest value

of momentum transfer is less than one, the Thomas-Fermi method is used in the region $0.058<q<1$ which, fortuitously, is in the domain in which this method is most accurate.

The inelastic contribution to the scattering is somewhat more difficult to calculate. Assuming the differential inelastic cross-section is the sum of the individual excitation cross-sections, considering excitations from the ground state only, Morse (Ref. 62) has shown that $G(\theta)$ is related to the transition probabilities associated with transitions by atomic electrons to higher energy levels (see Appendix A). Since the wave function for helium is simple enough to allow the required integrations, an analytical expression for the inelastic scattering factor can be obtained. The argon wave function does not lend itself readily to the above integration. However, Lenz (Ref. 63) treated small angle inelastic scattering of argon using exponential screening and obtained an expression which compared favorably with scattering experiments (Ref. 64); therefore this expression is used for argon.

A complete discussion of the calculations for the elastic and inelastic cross-sections is given in Appendix A. The results for helium and argon are presented as a function of the scattering angle in figures 27 and 28 for 7 kv, 10 kv, and 15 kv electrons.

Inelastic scattering involves a gain of energy by the target atom and is governed by the energy levels of this

atom; thus, inelastic scattering is expected to have a more complex dependence on electron energy than elastic scattering. The importance of inelastic scattering demonstrated in figures 27 and 28 gives some confidence to the belief that the energy dependence of the helium and argon cross-sections are not identical.

2.3c Theoretical Collector Current

Consider a beam of electrons whose flux is N (particles/cm^2/sec) incident on a scattering volume with ndz particles/cm^2 in a length dz. The attenuation of the beam by single scattering is represented by

$$dN(z) = - N(z)\ \sigma\ (z)\ ndz$$

or

$$\frac{dN}{dz} + n\sigma\ N = 0 \qquad (2.3\text{-}12)$$

where $\sigma = \iint \frac{d\sigma}{d\Omega} \sin\theta\ d\theta\ d\Phi$, total cross-section.

Solving the differential equation yields

$$N(\ell) = N(0)\ \exp\ (-\int_0^{\ell} n\ \sigma(z)\ dz) \qquad (2.3\text{-}13)$$

for the beam flux at a distance ℓ from its source. The relationship between particle flux and current gives

$$I = I_0 \exp(-nQ) \qquad (2.3\text{-}14)$$

where I = current

I_o = source current

n = number density

$Q = \int_o^{\ell} \sigma(z)\, dz$, the cross-section moment.

The total cross-section is obtained by integrating the differential cross-section over the solid angle exclusive of the collector. The integration is complicated by the increase in the excluded solid angle as the collisions occur closer to the collector. Referring to the schematic below,

$$\sigma(z) = \int_{\theta_m(z)}^{\pi} \int_0^{2\pi} \left(\frac{d\sigma}{d\Omega}\right) \sin\theta \, d\theta \, d\Phi \qquad (2.3\text{-}15)$$

where $\theta_m(z) = \tan^{-1}\left(\frac{R}{\ell - z}\right)$

R = radius of the collector.

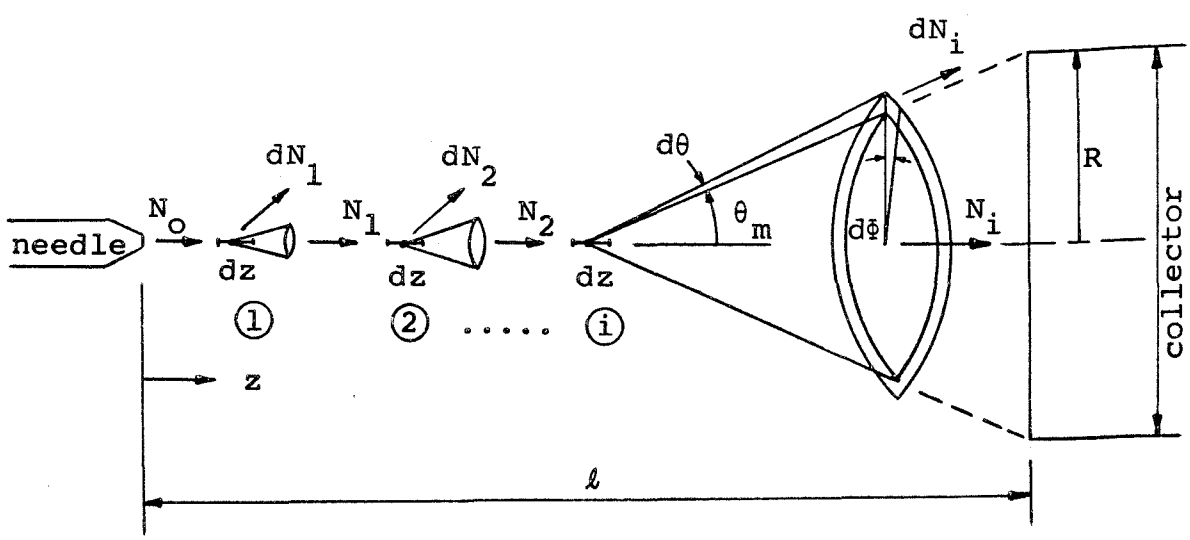

The results for the helium and argon total cross-sections (see Appendix A for details) are shown as a function of distance from the source (needle) in figure 29. The calculations assume that all collisions occur along the center line, the electron beam is homogeneous, and the scattering centers are fixed in space. These latter two assumptions are reasonable when considering the relative speeds of the incoming electrons and the atoms. However, the first assumption becomes less valid as the collisions occur closer to the collector. Fortunately, the assumption is poor only in a region of low scattering, i.e., the region in which few collisions direct an electron away from the collector.

The cross-section moment, defined as $Q = \int_0^{\ell} \sigma(z)\, dz$, is computed for helium and argon using the total cross-section expressions for these gases. Using Simpson's rule, the integrations are performed on a computer. These values are plotted versus α in figure 30 along with the effective Q defined by

$$Q = \alpha\, Q_{Ar} + (1 - \alpha)\, Q_{He} \qquad (2.3\text{-}16)$$

where $\alpha = n_{Ar}/n$, the argon concentration. The significant feature in this figure is the large helium concentration necessary to cause the effective Q to deviate from the cross-section moment of argon, a condition caused by the small helium cross-section.

With the value of Q determined in the above manner, the theoretical collector current I can be calculated for any given shock structure n(x) from equation 2.3-14. To obtain the best density profile of a shock wave in a helium-argon mixture, data from Center's experiments (Ref. 53) are used. Variations through the shock wave of concentration α and ratio of cross-section moment Q'/Q" are computed as well as the collector current I for 7 kv and 15 kv electrons. These results are presented in figures 31 and 32 for 2.2% argon (initial concentration) and in figures 33 and 34 for 48% argon. The results exhibited by these figures demonstrate the extremely small differences in collector currents which would be found experimentally under the given conditions (Mach number, initial concentration, and electron beam energy).

2.3d Results of Theory

The theoretical calculations cast doubt on the ability to achieve quantitative data from the experiments with a helium-argon mixture and the electron beam energy range available with the experimental apparatus. However, the only restriction imposed by the theory, the variation of cross-section with electron energy can not be the same for both gases, is not violated with a helium-argon mixture. Hence, qualitative data should be attainable. The small helium cross-section causes additional concern since the conversion of the experimental data to individual density

profiles is complicated by a large magnification factor χ (see equation 2.3-8) when the effective cross-section of the mixture very nearly equals the cross-section of one of the component gases. Figure 30 presents results showing deviations of effective cross-section from the argon cross-section for argon concentrations of less than 70%, but a 10% or greater deviation occurs only for argon concentrations less than 20%.

2.4 Apparatus

The GALCIT 17-inch shock tube and support equipment described in the measurement of the shock structure of a single gas (see section 1.3 and figure 1) is also utilized in the mixture experiments with the addition of an extra oscilloscope necessary for a timing reference. At first one might argue that two electron beams are required since this is the basis of the new technique to separate the density profiles of the individual species. This is obviously a desirable situation but not mandatory. One electron beam is sufficient if use is made of the repeatability of the shock tube. That is, two identical runs can be executed at different electron beam energies, thereby simulating the conditions of one run with two beams. Since these experiments are an attempt to examine the feasibility of a new technique in measuring the structure of the individual species in a mixture shock wave, it is only natural that the second method has been chosen for its simplicity and immediate availability. One obvious improvement can be made by averaging many duplicate experiments, thereby obtaining the density profiles of the species from these averaged shock profiles rather than from individual runs.

The disadvantage of the present method is the necessity for an absolute distance scale and the reliance on the

reproducibility of the shock tube. The latter problem is minor since previous work (section 1.6b) has shown experimental scatter to be much less than the expected diffusive separation. However, the attainment of an absolute distance scale or its equivalent, an absolute time scale, is a difficult problem which can produce errors of the same order as the separation. Surmounting this obstacle is one of the important aspects of these experiments and is described in section 2.6a.

2.5 Procedure

2.5a Selection of Mach Number and Initial Pressure

In all the mixture experiments the Mach number is held approximately constant at 4 (3.84 to 4.08) primarily due to the difficulty in obtaining a higher Mach number in mixtures of high helium concentrations. A second parameter p_1 is also held constant at 0.050 torr. The reasoning is based on the experience that shock waves with this relatively high initial pressure (for the GALCIT 17-inch shock tube) are less sensitive to the effects which cause the density to rise in the region behind the shock rather than reach the constant equilibrium value ρ_2. In addition, past experiments show no change in the shock structure of the noble gases when the initial pressure is varied from 0.010 torr to 0.050 torr (section 1.6a) and only slight changes are observed when the Mach number range is 3 to 8 (section 1.6c).

2.5b Determination of Mixture Concentrations

The first major problem encountered is the attainment of the correct mixture concentrations for consecutive runs. In most instances these mixtures are produced in the control volume of figure 1 just prior to a run by filling the volume until the desired partial pressures have been obtained. For example, a 20% argon mixture is produced by filling the control volume to 10 torr with argon and then adding helium until the final pressure is 50 torr.

This pressure is measured by a 0 to 50mm Wallace and Tiernan absolute pressure gauge (FA-160) with a reported accuracy of $\pm$0.33% of full scale and a sensitivity of 0.2% of full scale.

It is believed that most of the mixing takes place when the turbulent jet of helium is released into the control volume containing the argon. The low pressure in this volume aids the diffusion process, but extra precaution has been taken by allowing the gases to stand in this container for five minutes. A rough calculation shows that molecular diffusion should produce homogeneity in approximately this time. Further proof of complete mixing is not available until the shock structures of a mixture of 10.8% argon in helium obtained from the above method of mixing and from a certified bottled mixture (purchased from the Matheson Company) are compared; experiments conducted with the purchased bottle are identical in structure and Mach number.

To investigate the influence of initial concentration on the diffusive separation, experiments are conducted with test mixtures of 10%, 20%, 50%, and 80% argon concentration. Difficulties in producing small partial pressures in the control volume limit the test mixture to concentrations greater than 10% of one component.

2.5c Creation of the Shock Wave

After a mixture concentration is selected, the driven section is evacuated to 0.01 μ Hg (1 μ Hg = 10^{-3} torr) as measured by a liquid nitrogen trapped McLeod manometer. The tube is then flushed with the test mixture to 0.050 torr and again pumped down to below 0.01 μ Hg. During the five minute period in which the mixture is allowed to homogenize, the vacuum pump values are closed and the diaphragm checked for leaks by filling the driver to 6 psia with the high pressure gas (typically helium or nitrogen) and watching the test section pressure for sudden changes. This done, the mixture is released into the shock tube along a path of many turns, expansions, and contractions which again aids the mixing process.

The mixture is allowed to stand for another three minutes to permit the pressure to reach equilibrium throughout the tube. Meanwhile the oscilloscopes are pre-set with the desired sensitivity and sweep rates and the electron beam heater filament is turned on in a warm-up procedure for 1½ minutes. With all valves to the shock tube closed and the electron beam activated and aligned for maximum collector current, the shot is fired and recorded on polaroid film. A notation is made of the temperature, time required for the shock to travel 50 cm (as determined by two thin film heat gauges mounted in the

side of the shock tube), and various electron beam data such as energy, cathode current, etc. A diaphragm change completes the cycle. A typical time from closure of the vacuum valves to bursting of the diaphragm is fifteen minutes.

2.6 Data Reduction

In mixture experiments four oscillograms are needed (Fig. 35). The first three are identical to those in the noble gas experiments, and a description of their processing is given in sections 1.5a and 1.5b. The fourth trace provides a history of the triggering signal and is used to establish the absolute distance scale required in the mixture runs.

2.6a Absolute Distance Scale

In the shock structure measurements of a single monatomic gas it is unnecessary to obtain an absolute distance scale since all profiles can be plotted relative to a given point, like the 0.5 point, on a normalized density profile and distances measured from this point in units of mean free paths. However, in seeking shifts between two such profiles obtained at different electron beam energies, it is necessary to refer all distances to an absolute scale. This is not a trivial matter because the differences caused by the electron energy changes are less than a mean free path.

The absolute distance scale is obtained by using the end-wall triggering signal to define a "zero" time since this signal is independent of electron energy and dependent only on the shock wave. Ideally, the reference time might be any easily identifiable point on the signal; however, slight variations in amplitude between runs would cause

unacceptable error. Fortunately, there is one point that does not change with amplification, and that is the position of maximum slope. Due to difficulty in defining this point, the triggering signal is differentiated (electrically) and displayed on the lower beam of the dual-beam oscilloscope (Fig.35d). The peak of this signal represents the maximum slope and is used as the standard point from which all times are calculated.

The digitized shock structure data obtained from oscillogram c (Fig. 35) are converted to relative time by interpolation between time marks (see section 1.5a) and then readjusted so that the maximum slope of the triggering signal is zero time. This is done by measuring the time, T_0, from the maximum slope to the dot on the triggering signal which corresponds to the first time mark on oscillogram c (see figure 35). These times are then converted to distances by a Galilean transformation employing the shock wave velocity ($x = Ut$). For convenience the distance scale is shifted to make zero occur near the center of the shock wave and normalized with a length roughly equivalent to the mean free path of the mixture in the undisturbed region ahead of the shock wave.

The length used to normalize the distance scale can be thought of as a mean free path since it is obtained by considering the mixture molecules as hard spheres and

calculating the mean free path of this model using the actual mixture viscosity, molecular weight, etc. Hence,

$$\lambda_1 = \frac{16}{5}\sqrt{\frac{\gamma}{2\pi}}\frac{\mu}{\rho_1 a_1} \qquad (2.6\text{-}1)$$

where λ_1 = normalization length

γ = specific heat ratio

ρ_1 = density of the mixture ahead of the shock

μ = viscosity of the mixture

a_1 = sonic speed of the mixture.

The sources of error in the above procedure can only come from inaccuracies in the Tektronix Time Mark Generator (#180A) used to generate the time dots on the oscillograms and in measuring the maximum slope point. This latter restriction is by far the most severe since the peak voltage can only be measured to within $\pm$0.1 microsecond due to the poor resolution of the differentiated signal (lower trace on oscillogram d); whereas the time mark generator has a quoted accuracy of $\pm$0.0001%.

2.6b Determination of Calibration Constants

In the mixture experiments there are six calibration constants (see section 2.3a), K_1', K_1'', K_{Ar}', K_{Ar}'', K_{He}', and K_{He}'' of which only four are independent. This allows a certain degree of flexibility in their evaluation. K_1 is determined in each run from the Rankine-Hugoniot relations for the

density jump across a shock wave and the known values of the current in these regions (see equation 2.3-5). In addition, an average value is obtained from all experiments conducted at fixed conditions. The argon and helium constants, K_{Ar} and K_{He}, can be calculated either from static calibrations in which the electron beam attenuation is measured at various densities of the test gas for a particular beam energy (Fig. 36), or from shock wave experiments conducted with the pure gas (see section 1.7a). These two methods are referred to as static and dynamic calibrations, respectively. The two methods produce similar results for the argon calibration constant, hence either method is acceptable. However for helium, which has such a small calibration constant, it is better to use the relation

$$K_{He} = K_{Ar} + (K_1 - K_{Ar}) \; / \; (1 - \beta_1) \qquad (2.6\text{-}2)$$

$$\text{where} \quad \beta_1 = (\rho_{Ar} \; / \; \rho)_1$$

since K_1 and K_{Ar} are more accurately known. This equation is derived from the attenuation law considering the mixture as both a composite gas and as two individual gases, i.e.,

$$I_1 = I_0 \exp \left(- K_{He} \, \rho_{He_1} - K_{Ar} \, \rho_{Ar_1}\right) \qquad (2.6\text{-}3)$$

$$\text{and} \qquad I_1 = I_0 \exp\,(-K_1\,\rho_1)\ . \qquad (2.6\text{-}4)$$

The subscript 1 refers to the upstream equilibrium region of the shock wave.

2.6c Experimental Density Profiles

The digitized data are converted to composite density profiles using equation 2.3-4. The absolute time scale provides a means of comparing two such profiles. The individual helium and argon shock structures are then obtained from the differences in the composite profiles and the values of the calibration constants discussed in section 2.6b (see equation 2.3-8). All of these computations are programmed for an IBM 360/75 computer.

2.7 Results

The goal of these experiments has been to discover the feasibility of a modified electron beam densitometer technique to measure the diffusive separation in shock waves in a helium-argon mixture. In theory the method is practical provided the ratio of the cross-sections (equivalently, ratio of the calibration constants) at two electron energies is not the same for the gases involved. In addition, it has been shown that the separation of the structure of the species is related to the difference in the normalized density profiles of the mixture at the two beam energies when the mixture is considered to be a composite gas with mean properties.

The accuracy to which the two composite density profiles can be separated is dependent on the experimental scatter. A typical example of this scatter (rms deviation) is shown in figure 37 for the case of 80% argon. The Mach number is fixed at approximately 4 and the total initial pressure is .050 torr. For reference, the width of this scatter band is approximately ½ microsecond.

The composite profiles for 10%, 20%, 50% and 80% argon are given in figures 38, 39, 40, and 41 respectively. Each of these structures is an average of a number of experiments ranging from a minimum of 2 to a maximum of 5. The error bars indicated on these figures represent the rms deviation.

Under certain conditions the rms deviation is less than the line width; hence the bars have been omitted. In most cases the averaged profile at one energy is outside the scatter band of the second profile. The 10% argon case is a noticeable exception. However, there are many instances in which the two scatter bands overlap. The average separation of these profiles, in terms of the normalized length λ_1, is approximately 0.1, 0.25, 0.15, and 0.2 for the four mixture concentrations, respectively.

The difference in the composite shock structure allows profiles of the individual species to be separated. These results are illustrated in figures 42, 43, 44, and 45. Two effects are immediately obvious. First, there is large scatter in all helium profiles and in the argon structure at the lowest argon concentration. Second, most of the helium profiles do not normalize to 1. This latter effect is due to the increase in density beyond the equilibrium value ρ_2. Since the composite shock structures exhibit a difference in density past this point the structures of the individual species reflect this difference. In addition, uncertainties in the static calibrations, K_{Ar} and K_{He} may cause the profiles to be normalized inaccurately.

Qualitatively, the density profiles of the individual species are correct. The helium atoms concentrate in the front of the shock wave ahead of the argon atoms. In addition, the separation (approximately 20% of the shock

thickness) is of the same order as that found by Center (see reference 53 and figure 31). Quantitatively, little can be inferred from the results and the large scatter prohibits comment on the velocity anomaly.

2.8 Discussion

The theory of the modified electron beam densitometer technique has indicated a number of areas of concern. These areas are manifested in the scaling factors χ associated with separating the composite profiles into profiles of the individual species. The results demonstrate the full significance of the difficulties, and this section attempts to discuss the important aspects of the problem.

2.8a Experimental Scatter

The use of a single electron beam in the present investigation has required an absolute time scale to which all experiments can be related. This is done by establishing a reference time on the triggering signal (section 2.6a). The accuracy with which this has been accomplished is demonstrated in the results (Fig. 37). The scatter is approximately ½ a normalized length (λ_1) which is equivalent to measuring the reference time to 0.5 microsecond. Although this is a reasonable rms deviation under the circumstances, it is still a factor of three worse than the scatter obtained from the shock structure measurements of the noble gases (section 1.6b). Unfortunately, the magnification of the scatter when converting to the structure of the individual species makes even this error intolerable.

The problem of determining the value of the downstream equilibrium density is again evident from the results.

Uncertainty in the value of this density causes improper normalization of the final structure of the individual species and is more appropriately discussed in section 2.8b.

2.8b Composite Shock Structure

The composite profiles (Figs. 38 - 41) show a very small separation at the two electron beam energies used and, although the 10% argon mixture has the smallest separation, there seems to be no logical progression with increasing concentration. The difference in the composite structures at a fixed gas concentration reflects the variation of the cross-section of the gas atoms with electron beam energy. Therefore the larger the energy range the greater the difference will be. In these experiments the electron energies are 7 kv and 15 kv. The electron-atom collision cross-section exhibits a rapid change with energy in this range; therefore each additional kv increment in electron energy aids the ability to separate the profiles. Calculations give a maximum limit of 30 kv to 50 kv after which further increases in energy add little to the total cross-sections.

A more severe problem stems from the density rise beyond the equilibrium state. The data reduction scheme is based on the downstream density reaching a constant value (ρ_2) . Under these conditions the profiles of the individual species will normalize properly to 1 since

$\bar{\rho}'' - \bar{\rho}'$ will remain zero after both composite profiles have attained the downstream equilibrium state of the shock wave ($\bar{\rho}' = \bar{\rho}'' = 1$) . However, the now infamous density increase causes $\bar{\rho}'' - \bar{\rho}'$ to be non-zero everywhere (except for minor coincidences). The problem is further complicated by uncertainty in the selection of state 2. The result is improper normalization of the density profiles of the individual species (Figs. 42 - 45). Perhaps the composite profiles should be forced to remain constant once the density has reached the equilibrium value ρ_2 , i.e., neglect the density variation of the downstream tail of the shock; then the upper limit of the structure of the individual species would be 1. This idea has prompted the representation of the profiles as terminating at $(\rho - \rho_1)/(\rho_2 - \rho_1) = 1$ regardless of the direction indicated by the data. It remains for the reader to smooth the curve into the dashed line if desired (Figs. 42 - 45).

2.8c Density Profiles of the Individual Species

The theoretical results of section 2.3 warn of the difficulties in separating the density profiles of the individual species in a helium-argon mixture with the limited electron beam energy range available (7 kv - 15 kv). However, the experiments have been conducted to confirm these suspicions and to salvage at least qualitative data from the new technique. This has been accomplished with

an extra bonus of now understanding the full significance of the theoretical predictions.

The results of figures 42 - 45 exhibit many interesting features. First, the scatter in the argon structure increases with decreasing argon concentration and a large degradation is noticeable between the 20% and 10% argon mixture. Second, there is large scatter in all helium profiles. Third, most of the helium structures do not normalize to 1 (see section 2.8b). Fourth, the 20% argon mixture gives the best overall results based on separation and smoothness of the profiles. The central point to the understanding of these features is the small collision cross-section of the helium atoms.

In theory the individual density profiles are calculated from the difference in the two composite shock structures multiplied by a constant χ (appropriately termed a magnification factor) which represents the degree of similarity between the ratios of the cross-sections of the gases at the two beam energies. If these ratios are identical, then χ is infinite; whereas if there is a large dissimilarity in the ratios, then χ approaches 1. Clearly, $\chi = \infty$ implies that the structure of the individual species can not be separated and $\chi = 1$ means that the errors incurred in establishing the composite profiles are not magnified when constructing the individual profiles. Equivalently, these ratios can be compared to the ratio of

the effective cross-section at the two beam energies, i.e., treating the mixture as a composite gas. This results in two constants, χ_{He} and χ_{Ar}, which are so arranged that χ_{He} is the degree of similarity between the ratios of the effective cross-sections and the argon cross-sections and vice versa.

In most circumstances the effective cross-section is approximately equal to the argon cross-section. This is because helium has a very small cross section which is almost completely negligible in determining the effective cross-section. As the argon concentration increases, the importance of the helium atoms becomes even smaller. Since the profiles of the individual species can be thought of as reflecting the amount of scattering or beam attenuation of the atoms, increasing the argon concentration produces a poorer helium structure. Analytically this fact is represented by an increase in the helium magnification factor χ_{He} and a decrease in χ_{Ar}. For argon concentrations above 50%, the ratio of the effective cross-sections at the two beam energies is very nearly equal to the ratio of the argon cross-sections (see figure 30). This means that helium is ineffective in the scattering process; consequently the helium structure will exhibit large errors (χ_{He} is very large, 10 to 20). This fact is especially noticeable near the downstream tail of the shock wave ($\rho \simeq \rho_2$) where the density uncertainty is the largest,

as explained in section 2.8b. The argon profiles in the progression of increasing argon concentrations improve rapidly, obviously due to the dominance of the argon atoms in determining the effective cross-section (χ_{Ar} is only 2 or 3).

The above reasoning is not true for high helium concentrations, e.g., 10% argon. Under this condition both the helium and argon atoms contribute a finite amount to the effective cross-section. However, this means that the effective value is small, otherwise the helium portion would be negligible. The net result is large errors in the composite shock structures due to the very poor signal to noise ratio caused by small beam attenuation. Such a situation causes difficulty in separating the composite profiles as is obvious in figure 38. Therefore, both structures in figure 42 have large scatter.

The 20% argon case (Fig. 43) appears to be the perfect balance between the two above-mentioned effects which actually occur because of the same problem, the small helium cross-section. For small argon percentages the effective cross section is so small that it is difficult to obtain the correct composite shock profiles. On the other hand, for large argon concentrations the two electron beam signals are completely dominated by the argon atoms; therefore very little information about the helium structure is obtained. However, in the 20% argon case there is enough

argon present to produce correct composite profiles and, at the same time, there is enough helium present to obtain information about the helium structure. This appears to be a coincidence in the present investigation but it does demonstrate the soundness of the technique and shows what can be expected under favorable conditions.

2.9 Conclusion

The purpose of this work is to test the feasibility of the modified electron beam densitometer for measuring the diffusive separation in a helium-argon shock wave. Qualitatively the technique has been verified. For all mixture concentrations tested, the helium atoms diffuse upstream and the resulting separation is of the order of 20% of the total shock thickness.

Quantitatively the method is disappointing. Large scatter prevents comments on the velocity anomaly and the other interesting phenomena, e.g., the relationship between initial concentration and the diffusive separation.

It is believed that the qualitative results may be substantiated by quantitative data if a few adjustments are made. The most important is a more favorable mixture, i.e., one in which both atoms contribute to the effective cross-section at all concentrations (except for the case of minute percentages of one component). Such a combination might be xenon-argon or even xenon-neon. Another beneficial change would be an increase in the electron beam energy range. This would result in larger differences in the composite density profiles. An upper limit to this increase is approximately 50 kv based on calculations of the collision cross-sections for helium and argon. Finally, the use of two electron beams would be very effective in

reducing scatter. Such a scheme would eliminate the need for an absolute time scale and make every run self-contained.

APPENDIX A

SCATTERING CROSS-SECTIONS

The general problem involves the scattering of an electron incident on a target atom which has both an atomic and a nuclear structure. This electron interacts elastically with the screened nuclear field as well as inelastically with the orbital electrons. Under the assumption of central potentials with spherically symmetric charge and magnetic moment distributions, calculations based on the Born approximation for point charges and point magnetic moments can be corrected for an atom of finite structure. This is done by multiplying the point potential formulas by appropriate scaling or form factors (Ref. 56). Hence,

$$\frac{d\sigma}{d\Omega}(\theta) = \left(\frac{d\sigma}{d\Omega}\right)_R \left\{[G_E(\theta)-F(\theta)]^2 \, S_E(\theta) + \frac{G(\theta)}{Z}\right\} + \left(\frac{d\sigma}{d\Omega}\right)_M \left[\frac{G_M}{\mu}\right]^2 \tag{A-1}$$

where $\left(\frac{d\sigma}{d\Omega}\right)_R$ = Rutherford point nucleus cross-section

G_E, F = the nuclear and atomic form factors, respectively

S_E = electron spin effects

G = the contribution to inelastic scattering

$\left(\frac{d\sigma}{d\Omega}\right)_M$ = scattering cross-section due to a point magnetic moment

G_M = magnetic moment form factor

μ = magnetic moment of the nucleus

Z = atomic number.

The contribution from inelastic scattering is written as G/Z because for large scattering angles the inelastic cross-section rapidly approaches $1/Z$ of the elastic cross-section (Ref. 55). However, the nuclear form factors are only important for extremely high electron energies in which large amounts of momentum are transferred in the collision. For small momentum transfer the scattering due to the magnetic moment is negligible and the nucleus can be considered a point charge with $G_E = 1$ (Ref. 56). Thus

$$\frac{d\sigma}{d\Omega}(\theta) = \left(\frac{d\sigma}{d\theta}\right)_R \left\{[1 - F(\theta)]^2 \, S_E(\theta) + \frac{G(\theta)}{Z}\right\} . \quad \text{(A-2)}$$

In principle, if the atomic and nuclear structure of the atom is known, then the various form factors can be calculated as will be seen in the next two sections.

A.1 Elastic Scattering

To calculate the elastic scattering of a beam of non-relativistic electrons by a spherically symmetric potential $V(r)$, one must solve the Schrödinger wave equation,

$$\nabla^2\psi + [k^2 - U(r)]\psi = 0 \qquad \text{(A-3)}$$

where $k = \frac{2\pi mv}{h}$, the wave number

m = mass of the electron

v = velocity of the electron

h = Planck's constant

$U(r) = 8\pi^2 mV(r)/h^2$

and ψ, the wave function, has the asymptotic form

$$\psi \sim e^{ikz} + \frac{e^{ikr}}{r} f(\theta) \ . \qquad \text{(A-4)}$$

In this form $\exp(ikz)$ is the incoming plane wave (traveling in the z direction) representing the incoming electrons and $f(\theta)$ is the scattering amplitude of the outgoing spherical wave, $f(\theta)\exp(ikr)/r$, representing the scattered electrons. From a consideration of the incoming and scattered particle fluxes, the differential cross-section is given by $|f(\theta)|^2$.

The general solution to equation A-3 (Ref. 65) with the required asymptotic form (A-4) is

$$\psi \sim e^{ikz} - \frac{e^{ikr}}{r} \cdot \frac{1}{4\pi} \int e^{-ik\vec{n}\cdot\vec{r}'} U(\vec{r}') \psi(\vec{r}') d\tau' \qquad (A-5)$$

where $d\tau'$ = volume element of the coordinate space of the atomic electrons

$\vec{n}$ = unit vector in the direction of $\vec{r}$.

Assuming the Born approximation, i.e., the wave function is undisturbed by the scattering center, $\psi(\vec{r}')$ in equation A-5 can be replaced by $\exp(ikz')$ and the integral evaluated for $f(\theta)$ using spherical polar coordinates. The result is

$$f(\theta) = -\frac{8\pi^2 m}{h^2} \int_0^\infty \frac{\sin Kr}{Kr} V(r) r^2 dr \qquad (A-6)$$

where $K = 4\pi mv\sin\frac{1}{2}\theta/h$

θ = scattering angle.

It is sometimes convenient to express the atomic field $V(r)$ as the potential due to the nuclear charge $-Z\epsilon$ plus the potential due to the charge density $Z\epsilon\rho(r)$ of the atomic electrons. Thus,

$$V(r) = -\frac{Z\epsilon^2}{r} + \epsilon^2 \int \frac{Z\rho(r')\, d\tau'}{|\vec{r} - \vec{r}'|} \qquad (A-7)$$

where Z = atomic number

ϵ = charge on the electron

$|\vec{r} - \vec{r}'|$ = the distance to the atomic electrons from the incoming electron.

Substituting $V(r)$ into equation A-6 yields

$$f(\theta) = \frac{8\pi^2 mZ\epsilon^2}{h^2 K^2} [1 - F(\theta)] \qquad \text{(A-8)}$$

$$\text{where} \quad F(\theta) = 4\pi \int_0^\infty \rho(r) \frac{\sin Kr}{Kr} r^2 \, dr \, .$$

Therefore, if the charge distribution of the atom is known, the atomic form factor can be calculated.

As the energy of the incoming electron increases, the electron will penetrate the atomic electron cloud and render the screening ineffective. In this region $F(\theta)$ goes to zero and $(d\sigma/d\Omega)$ reduces to the Rutherford differential cross-section $(d\sigma/d\Omega)_R$.

$$\frac{d\sigma}{d\Omega} = |f(\theta)|^2 = \left(\frac{8\pi^2 mZ\epsilon^2}{h^2 K^2}\right)^2 = \left(\frac{2Zr_o E}{q^2}\right)^2 = \left(\frac{d\sigma}{d\Omega}\right)_R \qquad \text{(A-9)}$$

where E = electron energy in units of $m_o c^2$

m_o = electron rest mass

c = velocity of light

r_o = $\epsilon^2/m_o c^2$, the classical electron radius

q = $2mv/m_o c \sin \frac{1}{2}\theta$, the momentum transferred in a collision in units of $m_o c$.

The electron-spin effect (see equation A-2) is obtained by comparing the Rutherford cross-section for nonrelativistic electrons and the Mott-Born cross-section for relativistic electrons (Ref. 56). The difference in these two cross-

sections is

$$S_E = 1 - (q/2E)^2 \ . \qquad \text{(A-10)}$$

Although $q/2E$ is generally negligible for the present energy range, this term has been included for completeness. Therefore, the differential elastic scattering cross-section (Eqn. A-2) can be expressed as

$$\left(\frac{d\sigma}{d\Omega}\right)_E = \left(\frac{2Zr_o E}{q^2}\right)^2 \cdot \left(1 - F(q)\right)^2 \cdot \left[1 - \left(\frac{q}{2E}\right)^2\right] \ . \qquad \text{(A-11)}$$

Equation A-11 is subject to the following approximations (Ref. 56):

1) First Born approximation	$\frac{Z}{137\beta} \ll 1$	0.06 - 0.8*
2) Point-charge nucleus	$\frac{R_A \beta E}{2\pi r_o} \ll 1$	0.02 - 0.06
3) Infinitely heavy nucleus	$2E\left(\frac{m_o}{M_o}\right) \ll 1$	$< 10^{-4}$
4) Nucleus with negligible spin effects	$\left(\frac{q}{Z}\right)^2 \left(\frac{m_o}{M_o}\right)^2 \ll 1$	$< 10^{-13}$

where R_A = radius of nucleus (Ref. 56)

M_o = rest mass of atomic nucleus (Ref. 56).

*The maximum and minimum values of the parameters listed in column 2 for the present investigation.

Because of the complex nature of the electron distributions of most atoms, $\rho(r)$ is not known exactly. Therefore, various models have been developed to facilitate the calculation of the form factor $F(q)$. The simplest and least accurate is the exponential model of the atom (Ref. 56) in which

$$V(r) = -\frac{Z\epsilon^2}{r} \exp(-\Lambda r) \qquad \text{(A-12)}$$

where Λ, the screening parameter, is a function of the atomic number. As the electron energy increases, penetration becomes greater (r decreases) and the screened potential exponentially increases to a point nuclear field. Therefore, the model affords only qualitative results unless Λ is empirically chosen from experiments for a particular gas and electron energy.

The Thomas-Fermi statistical model gives a smooth charge distribution of the atom (Refs. 57, 58). The model is described by the potential

$$V(r) = \frac{Z\epsilon^2}{r} \Phi \qquad \text{(A-13)}$$

where Φ, the screening function, is given as the dependent variable of a second order differential equation with x the independent variable. In addition, x is a known function of Z and r. Since exact values of Φ are

known only from numerical tabulations, Moliere (Ref. 59) has given an analytical approximation for the Thomas-Fermi potential.

$$V(r) = -\frac{Z\epsilon^2}{r} \sum_{i=1}^{3} a_i \exp\left(-b_i \frac{r}{R_{TF}}\right) \qquad \text{(A-14)}$$

where $a_1 = 0.10$, $a_2 = 0.55$, $a_3 = 0.35$

$b_1 = 6.00$, $b_2 = 1.20$, $b_3 = 0.30$

$R_{TF} = 0.885\, a_o\, Z^{-1/3}$, radius of the Thomas-Fermi atom

$a_o = h^2/4\pi^2 m_o \epsilon^2$, Bohr radius of the hydrogen

The sum in equation A-14 represents the screening effect of the atomic electrons. The screening increases rapidly away from the origin (the nucleus); for $r = R_{TF}$, the potential due to the nuclear charge is reduced by 60%. The inherent limitation of the Thomas-Fermi statistical model is the averaging of the effects of the atomic shell structure.

Substituting the Moliere potential (A-14) into equation A-6 yields

$$1 - F(q) = q^2 \sum_{i=1}^{3} \frac{a_i}{\Lambda_i^2 + q^2} \qquad \text{(A-15)}$$

where $\Lambda_i = \frac{\lambda_o}{2\pi R_{TF}} b_i$

$\lambda_o = \frac{h}{m_o c}$, the Compton wavelength.

The parameter Λ is a measure of the screening. For large Λ (equivalently, large Z), a high incoming electron energy is necessary to penetrate the electron cloud and to render the screening ineffective. When Λ^2 is much less than q^2, the right hand side of equation A-15 approaches one and $F(q)$ approaches zero. This Moliere approximation has a sharper drop in the electron distribution at the edge of the atom and is expected to give a more accurate result than the Thomas-Fermi model (Ref. 56). Since the model does not account for the atomic shell structure, it is only valid for intermediate values of q (equivalently, intermediate values of the impact parameter).

The Hartree-Fock independent-particle model of the atom (Ref. 60) is the most accurate description of the charge distribution since the atomic potential for this model assumes that each atomic electron is in a nuclear field plus an average field due to the other electrons. The potential $V(r)$ for this model is given by

$$V(r) = -\epsilon^2 \int \left(\frac{Z}{r} - \sum_{n=1}^{Z} \frac{1}{|\vec{r} - \vec{r}_n|} \right) |\psi_o(\vec{r}_1, \ldots \vec{r}_Z)|^2 d\tau_1 \ldots d\tau_Z \qquad \text{(A-16)}$$

where ψ_o , the wave function of the atom, is obtained from Hartree's self-consistent field equations. The first term in this expression is the potential at a distance r , due to the nuclear charge. This field is diminished by the potential due to the charge distribution of the atomic electrons, a distribution which is based on the probability, $|\psi_o|^2 d\tau$, of finding an electron in a differential volume $d\tau$. Each electron is accounted for by integrating over the individual atomic electron coordinate space. In general, the method requires numerical calculations which, fortunately, have been performed by Ibers (Ref. 61) for a limited range of q ($0 \leq q \leq 0.058$).

A.1a Argon

Since the Hartree-Fock method is the most accurate, it is used wherever feasible. Hence, for argon, the values tabulated by Ibers are used for $q \leq 0.058$ and thereafter, the form factor obtained from the Thomas-Fermi model with the Moliere modification is used. Thus (see equations A-11 and A-15),

$$\text{(a)} \quad \left(\frac{d\sigma}{d\Omega}\right)_E = E^2 \, \bar{f}^2(q) \qquad \text{for } 0 \leq q \leq 0.058 \qquad \text{(A-17a)}$$

where $\bar{f}(q)$ is tabulated by Ibers
and $(q/2E)^2 \ll 1$ in this range.

$$(b)\quad \left(\frac{d\sigma}{d\Omega}\right)_E = \left(\frac{2Zr_oE}{q^2}\right)^2 \cdot \left[q^2 \sum_{i=1}^{3} \frac{a_i}{\Lambda_i^2 + q^2}\right]^2 \cdot \left[1 - \left(\frac{q}{2E}\right)^2\right] \qquad \text{(A-17b)}$$

for $q > 0.058$.

A.1b Helium

The solution of the Hartree-Fock field equations for the helium wave function can be represented as (Ref. 65)

$$\psi_o(r_1, r_2) = \Phi(r_1)\,\Phi(r_2) \qquad \text{(A-18)}$$

where $\Phi(r) = N(\pi a_o^3)^{-1/3}\left[\exp\left(-\frac{z_1 r}{a_o}\right) + c\exp\left(-\frac{2z_1 r}{a_o}\right)\right]$

$z_1 = 1.4558, \quad c = 0.6,$

$N = 1.48423, \quad a_o = 0.53\times10^{-8}$cm (Bohr radius).

Substitution ψ_o (A-18) into equation A-16 and performing the integration yields

$$V(r) = -H\epsilon^2 \sum_{i=1}^{3}\left\{\alpha_i\left[\left(\frac{i+1}{2}\right)\frac{z_1}{a_o} + \frac{1}{r}\right]\exp\left[-\frac{(i+1)z_1 r}{a_o}\right]\right\} \qquad \text{(A-19)}$$

where $\alpha_1 = 1/8,\ \alpha_2 = 2c/27,\ \alpha_2 = c^2/64$

$$H = \frac{128\,N^4}{z_1^6}\sum_{i=1}^{3}\alpha_i \quad .$$

Substituting this potential into equation A-6 gives $f(\theta)$,

and, finally

$$\left(\frac{d\sigma}{d\Omega}\right)_E = (2r_o\ E\ H)^2 \left[\sum_{i=1}^{3} \alpha_i \frac{2\gamma_i^2 + q^2}{(\gamma_i^2 + q^2)^2}\right]^2 \left[1 - \left(\frac{q}{2E}\right)^2\right] \qquad \text{(A-20)}$$

where $\gamma_i = (i + 1)\ z_1/137$.

The similarity between equation A-20 and A-17b is noticeable. If H is normalized such that $\sum \alpha_i = 1$, then H becomes 2, the atomic number for helium, as expected. The sum in equation A-20 is therefore the effect of the screening and for $q >> \gamma_i$ the differential cross-section reduces to the Rutherford cross-section.

In addition, the similarity between equation A-14 and A-19 is obvious. Factoring a $1/r$ from the summation terms leaves the coefficient of the exponentials as a function of r . This, in essence, reflects the shell structure of the atom.

A.2 Inelastic Scattering

The inelastic contribution to scattering is somewhat more difficult to calculate. However, assuming the differential inelastic cross-section is the sum of the individual excitation cross-sections, considering excitations from the ground state only, Morse (Ref. 62) has shown that if $\theta >> E_k/4E$ where E_k is an average excitation energy*

$$G(q) = 1 - Z\,F^2(q) + \frac{1}{Z}\int |\psi_o(\vec{r}_1,\ldots\vec{r}_Z)|^2 \cdot \sum_{k\neq\ell}^{Z} \exp\left[(i2\pi q/\lambda_o)\cdot(r_\ell\cos\theta_\ell - r_k\cos\theta_k)\right] d\tau_1\ldots d\tau_Z \qquad \text{(A-21)}$$

where $F(q)$ = atomic form factor

ψ_o = atomic wave function.

Taking E_k to be one-half the ionization energy, then the restriction on the scattering angle implies $\theta >> 3 \times 10^{-4}$ radians for helium and $\theta >> 9 \times 10^{-4}$ radians for argon when the electron energy is 7 kv. In the experimental apparatus the minimum scattering angle is 0.01 radians.

The integral in this expression can be thought of as the transition probability associated with an electron transition from the ground state to a higher energy level.

*The restriction is based on the idea that only energetically allowed transitions are possible (Ref. 65). Therefore, the energy of the incoming electron must be greater than the excited state energy level.

The first term (1) is the evaluation of the integral for $k = \ell$. As the scattering angle increases (q increases) G rapidly approaches one and the inelastic cross-section becomes 1/Z of the Rutherford cross-section (Eqn. A-2).

The complexity of the wave function for most atoms prevents the general use of this equation. Instead, an empirical determination of the inelastic scattering factor is obtained from experimental data. Such methods are obviously restricted to specific cases.

A.2a Argon

The argon wave function is too complex to use in equation A-21. However, Lenz (Ref. 63) treats small angle scattering of argon using exponential screening and obtains the expression

$$G(\theta) = 1 - \left[1 + \left(\frac{2\pi\theta b}{\lambda}\right)^2\right]^{-2} \qquad \text{(A-22)}$$

where $b = 2.75 \times 10^{-19}$ cm

$$\lambda = \frac{h}{mv} .$$

The screening parameter b is chosen from an empirical fit to the most available small angle scattering experiments for argon (Ref. 64). Using this expression in equation A-2 yields

$$\left(\frac{d\sigma}{d\Omega}\right)_i = \frac{4Zr_o^2 E^2}{q^4} \left\{ 1 - \left[1 + \left(\frac{2\pi\theta b}{\lambda}\right)^2 \right]^{-2} \right\}. \qquad \text{(A-23)}$$

The significant feature of equation A-23 is the variation of the inelastic cross-section with scattering angle. The inelastic scattering rapidly approaches $1/Z$ of Rutherford scattering with increasing θ .

A.2b Helium

Using the Hartree-Fock wave function for the helium atom (equation A-18) in equation A-21, the expression for the inelastic scattering factor can be obtained in closed form, i.e.,

$$G(q) = 1 - Z\,F^2(q) + \frac{H}{Z}\left[\sum_{i=1}^{3} \alpha_i \frac{\gamma_i^4}{(\gamma_i^2 + q^2)^2} \right]^2 . \qquad \text{(A-24)}$$

The inelastic differential cross-section then becomes

$$\left(\frac{d\sigma}{d\Omega}\right)_i = \frac{4\,Z\,r_o^2\,E^2}{q^4} \left\{ 1 - Z\,F^2(q) + \frac{H}{Z}\left[\sum_{i=1}^{3} \alpha_i \frac{\gamma_i^4}{(\gamma_i^2+q^2)^2} \right]^2 \right\} \qquad \text{(A-25)}$$

$$\text{where} \quad F(q) = 1 - \frac{q^2 H}{Z} \sum_{i=1}^{3} \alpha_i \frac{(2\gamma_i^2 + q^2)}{(\gamma_i^2 + q^2)^2} \quad .$$

A.3 Total Cross-Section

The total cross-sections are obtained by integrating the differential cross-sections over the solid angle exclusive of the collector (see schematic, section 2.3c). The integration is complicated by the increase in solid angle as collisions occur closer to the collector. Defining θ_m as the minimum scattering angle necessary to direct an electron away from the collector, the total cross-section can be expressed as

$$\sigma(z) = \int_{\theta_m(z)}^{\pi} \int_{o}^{2\pi} \left(\frac{d\sigma}{d\Omega}\right) \sin\theta \, d\theta \, d\Phi \qquad \text{(A-26)}$$

where $\theta_m(z) = \tan^{-1}(R/\ell - z)$

R = radius of the collector

$\ell - z$ = distance from the collector.

It is often convenient to transform to the momentum variable q. Since $q = 2\,(mv/m_o c)\sin\frac{1}{2}\theta$, equation A-26 becomes

$$\sigma(z) = \frac{2\pi}{\beta^2 E^2} \int_{q_m(z)}^{2\beta E} \left(\frac{d\sigma}{d\theta}\right) q \, dq \qquad \text{(A-27)}$$

where $q_m = 2\beta E \sin\frac{1}{2}\theta_m$.

A.3a Argon

Because the elastic differential cross-section for argon is given as numerical data in the range $q \leq 0.058$ instead of an analytical expression, it is necessary to fit polynomials to the numerical data before equation A-27 can be integrated. The best empirical expression is obtained by fitting two polynomials to the data. One function is valid in the range $0 \leq q \leq 0.01$ and the other in the range $0.01 \leq q \leq 0.058$. With these modifications equation A-27 is used (together with equation A-17) to give

$$\sigma_E(z) = \frac{2\pi}{\beta^2}\left\{\int_{q_m(z)}^{0.01} f_1^2\, q\, dq + \int_{0.01}^{0.058} f_2^2\, q\, dq + \int_{0.058}^{2\beta E}\left(1 - \frac{q^2}{4E^2}\right)(2Z\, r_o)^2\left[\sum_{i=1}^{3}\frac{a_i}{\Lambda_i^2 + q^2}\right]^2 q\, dq\right\} \tag{A-28}$$

where $f_1 = 4.7 - 97.4\, q - 7774.5\, q^2$

$f_2 = 12.4 - 136.8\, q^{\frac{1}{2}} + 441.8\, q - 1456.8\, q^2$.

The expression for the inelastic scattering factor $G(\theta)$ (Eqn. A-22) is simplified by making the assumption $\sin \theta/2 \approx \theta/2$. This is a valid assumption since $G(\theta)$ rapidly approaches 1 for increasing θ ($G = 0.999$ for $\theta = 0.3$ radian). Thus

$$G(\theta) \approx 1 - \left[1 + \left(\frac{2\pi qb}{\lambda_o}\right)^2 \right]^{-2} = G(q) \cdot \qquad \text{(A-29)}$$

Substituting $(d\sigma/d\Omega)_i$ (Eqn. A-23), with the above expression for $G(q)$, in equation A-27, gives

$$\sigma_i(z) = \frac{8\pi Z r_o^2}{\beta^2} \left\{ 2 \left(\frac{\lambda_o}{2\pi b}\right)^2 \int_{q_m(z)}^{2\beta E} \frac{dq}{q\left[\left(\frac{\lambda_o}{2\pi b}\right)^2 + q^2\right]} \right.$$

$$\left. + \int_{q_m(z)}^{2\beta E} \frac{q\, dq}{\left[\left(\frac{\lambda_o}{2\pi b}\right)^2 + q^2\right]^2} \right\} \cdot \qquad \text{(A-30)}$$

The integrals in equations A-28 and A-30 can be evaluated in closed form to obtain σ_i and σ_E as functions of z, the distance from the origin of the electron beam (see schematic in section 2.3c).

A.3b Helium

Substituting the expression for the differential elastic cross-section for helium (equation A-20) in equation A-27 yields

$$\sigma_E(z) = \frac{2\pi}{\beta^2} (2r_o H)^2 \int_{q_m(z)}^{2\beta E} \left[\sum_{i=1}^{3} \alpha_i \frac{2\gamma_i + q^2}{\left(\gamma_i^2 + q^2\right)^2} \right]^2 \left(1 - \frac{q^2}{4E^2}\right) q\, dq. \qquad \text{(A-31)}$$

Although the evaluation of this integral is a long and tedious process, each of the twelve terms can be integrated in closed form. Therefore, σ_E is obtained as a function of the distance from the needle injector.

Similarly, the integration of the inelastic cross-section presents no difficulty except that it is longer. Using equations A-25 and A-27,

$$\sigma_i(z) = \frac{8\pi z r_o}{\beta^2}\left\{\int_{q_m(z)}^{2\beta E}\left[\frac{dq}{q^3}\right] - Z\int_{q_m(z)}^{2\beta E}\left[1 - \frac{q^2 H}{Z}\right.\right.$$

$$\left.\left.\cdot\sum_{i=1}^{3}\alpha_i\frac{2\gamma_i^2 + q^2}{\left(\gamma_i^2 + q^2\right)^2}\right]^2\frac{dq}{q^3} + \frac{H}{Z}\int_{q_m(z)}^{2\beta E}\left[\sum_{i=1}^{3}\alpha_i\frac{2\gamma_i^2 + q^2}{\left(\gamma_i^2 + q^2\right)^2}\right]^2\frac{dq}{q^3}\right\}. \quad \text{(A-32)}$$

REFERENCES

1. Hayes, W.D., Gasdynamic Discontinuities, Princeton University Press, Princeton, New Jersey (1960).

2. Gilbarg, D. and Paolucci, D., J. Rat. Mech. and Anal. 2, 617 (1953).

3. Chapman, S. and Cowling, T., The Mathematical Theory of Non-uniform Gases, Cambridge University Press, London (1952).

4. Grad, H., Com. Pure and Appl. Math. 5, 257 (1952).

5. Liepmann, H.W., Narasimha, R., and Chahine, M., Phys. Fluids 5, 1313 (1962).

6. Mott-Smith, H.M., Phys. Rev. 82, 885 (1951).

7. Bird, G.A., J. Fluid Mech. 30, 479 (1967).

8. Cowan, G.R. and Hornig, D.F., J. Chem. Phys. 18, 1008 (1950).

9. Greene, E.F., Cowan, G.R., and Hornig, D.F., J. Chem. Phys. 19, 427 (1951).

10. Greene, E.F. and Hornig, D.F., J. Chem. Phys. 21, 617 (1953).

11. Hansen, K. and Hornig, D.F., J. Chem. Phys. 33, 913 (1960).

12. Linzer, M. and Hornig, D.F., Phys. Fluids 6, 1661 (1963).

13. Sherman, F.S., NACA-TN-3298, (1955).

14. Talbot, L. and Sherman, F.S., NASA-MEMO-12-14-58W, (1959).

15. Venable, D. and Kaplan, D.E., J. Appl. Phys. 26, 639 (1955).

16. Ballard, H.N. and Venable, D., Phys. Fluids 1, 225 (1958).

17. Duff, R.E. and Webster, W.M., Bull. Am. Phys. Soc. 4, 283 (1959).

REFERENCES (cont.)

18. Camac, M., Rarefied Gas Dynamics, v. 1, p. 240, Academic Press, New York (1965).

19. Russell, D., Rarefied Gas Dynamics, v.1, p. 265, Academic Press, New York (1965).

20. Schultz-Grunow, F. and Frohn, A., Rarefied Gas Dynamics, v.1, p. 250, Academic Press, New York (1965).

21. Schmidt, B., J. Fluid Mech. 39, 361 (1969).

22. Schmidt, B., Graduate Aeronautical Laboratories, California Institute of Technology 17-inch Shock Tube Experiments, Runs 2089-2491, (unpublished).

23. Mason, E.A. and Rice, W.E., J. Chem. Phys. 22, 843 (1954).

24. Hirschfelder, J.O., Curtiss, C.F., and Bird, R.B., Molecular Theory of Gases and Liquids, Wiley, New York (1954).

25. Whalley, E. and Schneider, W.G., J. Chem. Phys. 23, 1644 (1955).

26. Konowalow, D.D. and Hirschfelder, J.O., Phys. Fluids 4, 629 (1961).

27. Saxena, S.C., Kelly, J.G., and Watson, W.W., Phys. Fluids 4, 1216 (1961).

28. Chakraborti, P.K., Indian J. Phys. 35, 354 (1961).

29. Amdur, I. and Mason, E.A., Phys. Fluids 5, 370 (1958).

30. Amdur, I. and Mason, E.A., J. Chem. Phys. 22, 670 (1954).

31. Amdur, I. and Mason, E.A., J. Chem. Phys. 23, 415 (1955).

32. Amdur, I. and Mason, E.A., J. Chem. Phys. 23, 2268 (1955).

33. Amdur, I. and Mason, E.A., J. Chem. Phys. 25, 624 (1956).

REFERENCES (cont.)

34. Kamnev, A.B. and Leonas, V.B., Doklady Akademii Nauk 165, 1273 (1965), [translation: Soviet Physics - Doklady 10, 1202 (1966)].

35. Amdur, I. and Jordan, J.E., Adv. Chem. Phys. 10, 29 (1966).

36. Bleick, W.E. and Mayer, J.E., J. Chem. Phys. 2, 252 (1934).

37. Abrahamson, A.A., Phys. Rev. 130, 693 (1968).

38. Keeler, R.N., Van Thiel, M., and Alder, B.S., Physica 31, 1437 (1965).

39. Liepmann, H.W., Roshko, A., Coles, D., and Sturtevant, B., Rev. Sci. Instr. 33, 625 (1962).

40. Wang, C.C.P., Ph.D. Thesis, California Institute of Technology (1967).

41. Cook, A., Argon, Helium, and the Rare Gases, v. 1, Interscience Publications, New York (1961).

42. Schmidt, B., Lab Notebook (unpublished).

43. Piva, H., Ph.D. Thesis, California Institute of Technology (1968).

44. Cowling, T.G., Phil. Mag. 33, 61 (1942).

45. Sherman, F.S., J. Fluid Mech. 8, 465 (1960).

46. Oberai, M.M., Phys. Fluids 8, 826 (1965).

47. Goldman, E. and Sirovich, L., J. Fluid Mech. 35, 575 (1969).

48. Abe, K., and Oguchi, H., Rarefied Gas Dynamics, v. 1, p. 425, Academic Press, New York (1965).

49. Beylich, A.E., Ph.D. Thesis, Technische Hochschule Auchen (1968).

50. Harris, W.L. and Bienkowski, G.K., Rarefied Gas Dynamics, v. 1, p. 397, Academic Press, New York (1969).

REFERENCES (cont.)

51. Bird, G.A., J. Fluid Mech. 31, 657 (1968).

52. Rothe, D.E., Phys. Fluids 9, 1643 (1966).

53. Center, R.E., Phys. Fluids 10, 1777 (1967).

54. Harnett, L.N., Ph.D. Thesis, University of California, Berkeley (1969).

55. Center, R.E., Avco-Everett Research Laboratory, Research Report 329 (1969).

56. Motz, J.W., Olsen, H., and Koch, H.W., Rev. Modern Phys. 36, 881 (1964).

57. Thomas, L.H., Proc. Camb. Phil. Soc. 23, 542 (1927).

58. Fermi, E., Zeits. f. Physik 48, 73 (1928).

59. Moliere, G., Z. Naturforsch. 2a, 133 (1947).

60. Hartree, D.R., Proc. Camb. Phil. Soc. 24, 111 (1928).

61. Ibers, J.A., International Tables for X-Ray Crystallography, v. III, The Kynoch Press, Birmingham, England (1962).

62. Morse, P.M., Phys. Z. 33, 443 (1932).

63. Lenz, F., Z. Naturforsch. 9a, 185 (1954).

64. Berkes, I. and Demeter, I., Nucl. Phys. 15, 421 (1960).

65. Mott, N.F. and Massey, H.S.W., Theory of Atomic Collisions, Clarendon Press, Oxford 3rd Edition (1965).

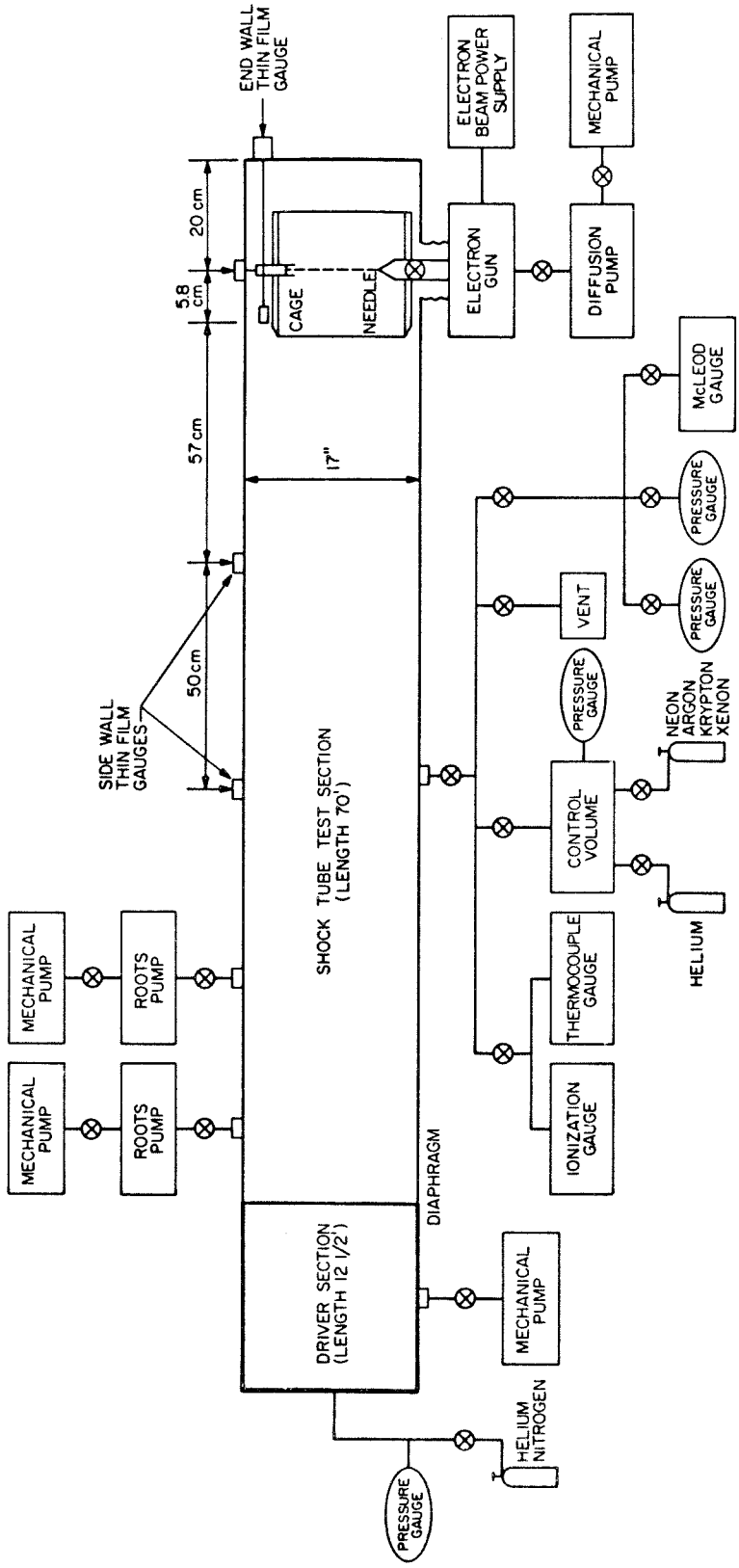

Figure 1. Schematic Diagram of the Apparatus

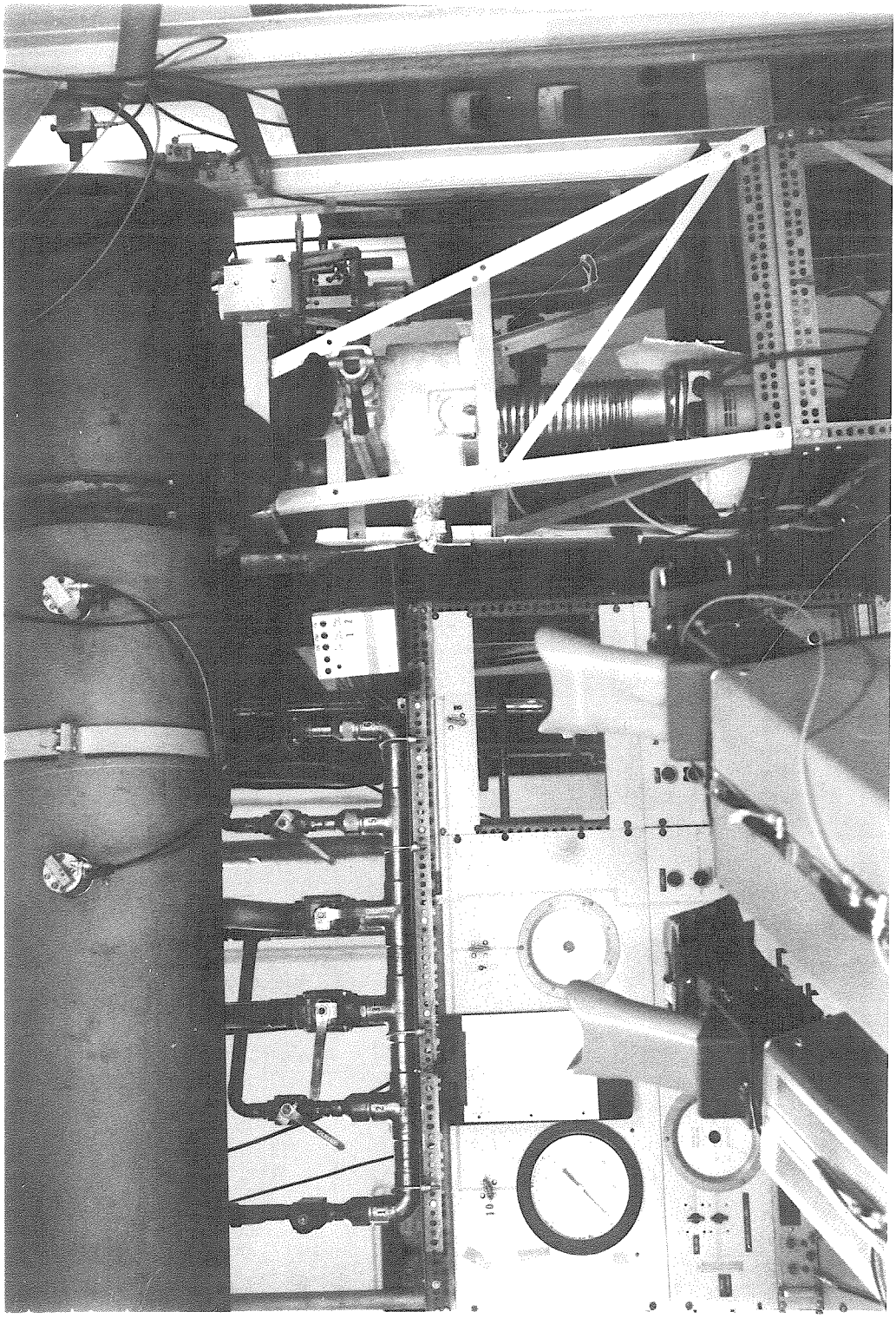

Figure 2. GALCIT 17-inch Shock Tube and Electron Beam

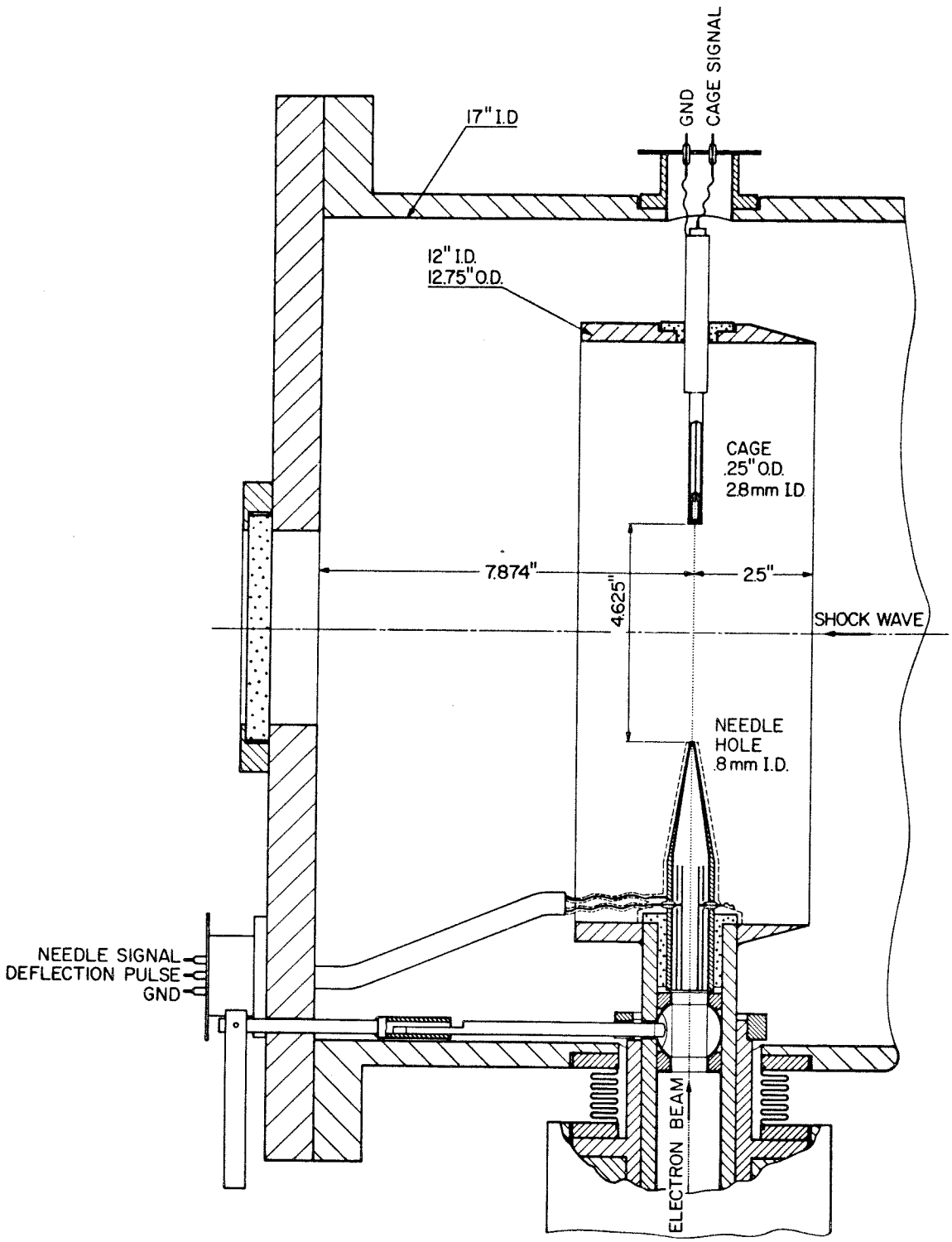

Figure 3. Electron Beam Schematic

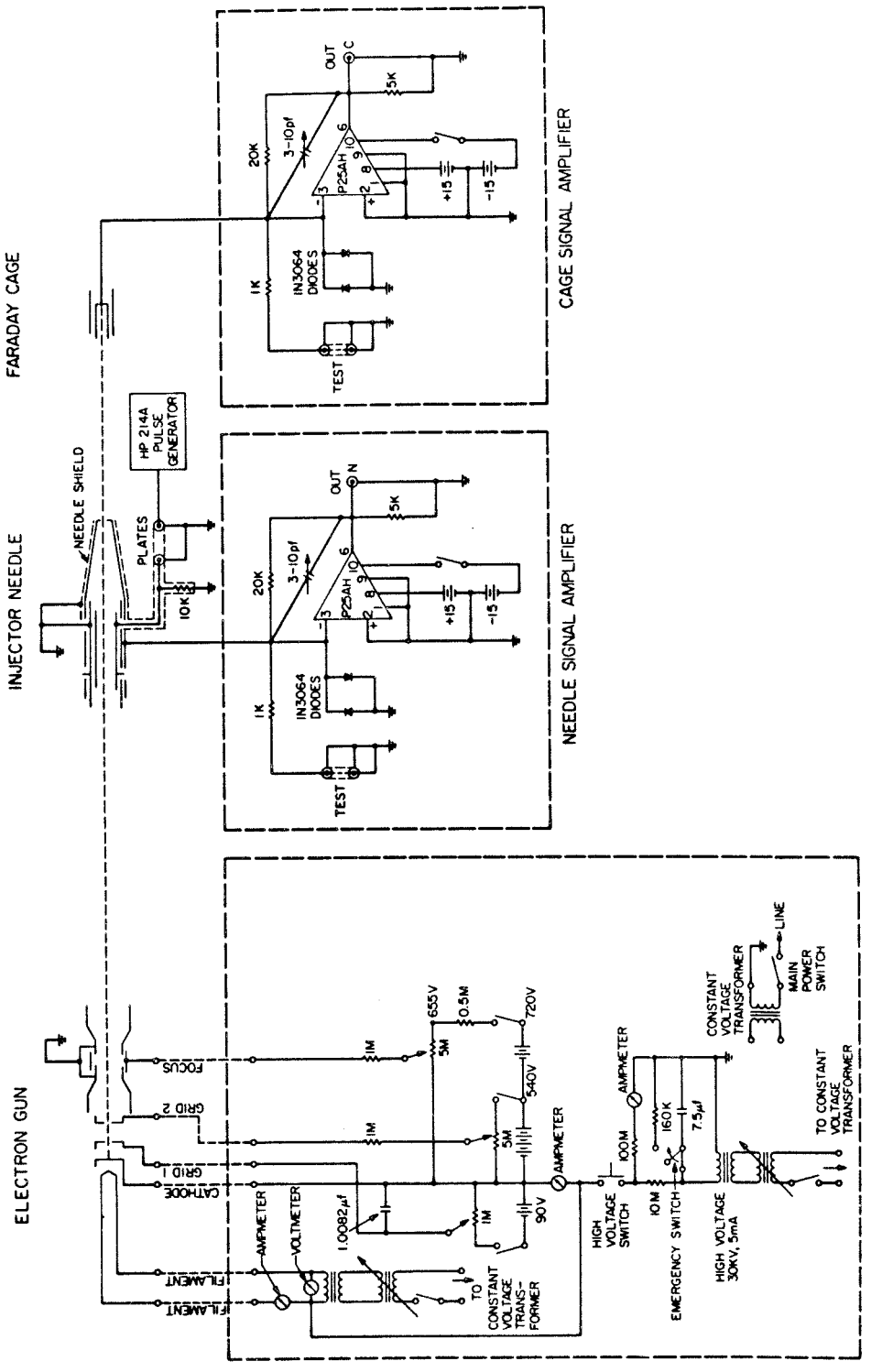

Figure 4. Circuit Diagram of Electron Beam Power Supply and Needle and Cage Signal Amplifiers

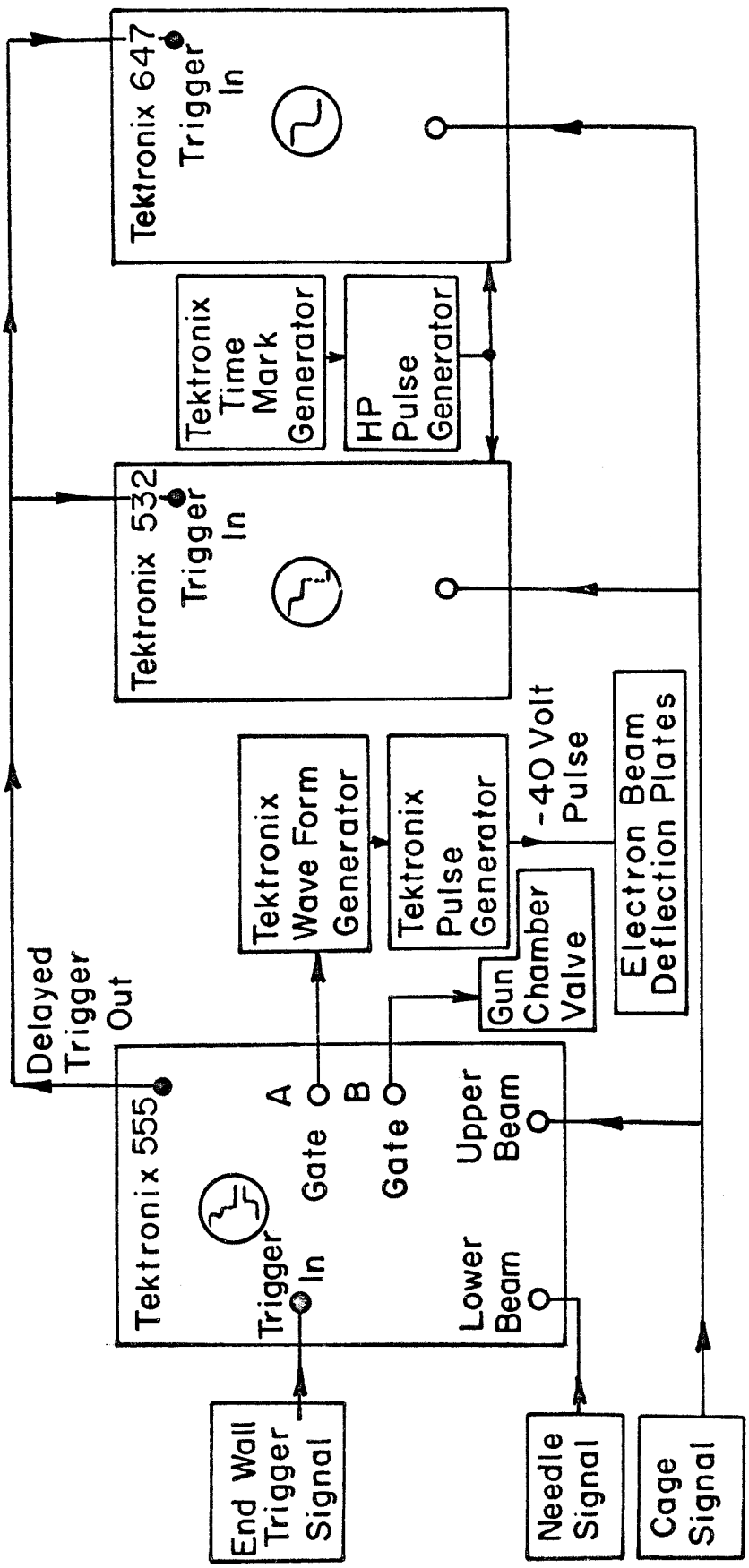

Figure 5. Schematic of the Electronic Equipment

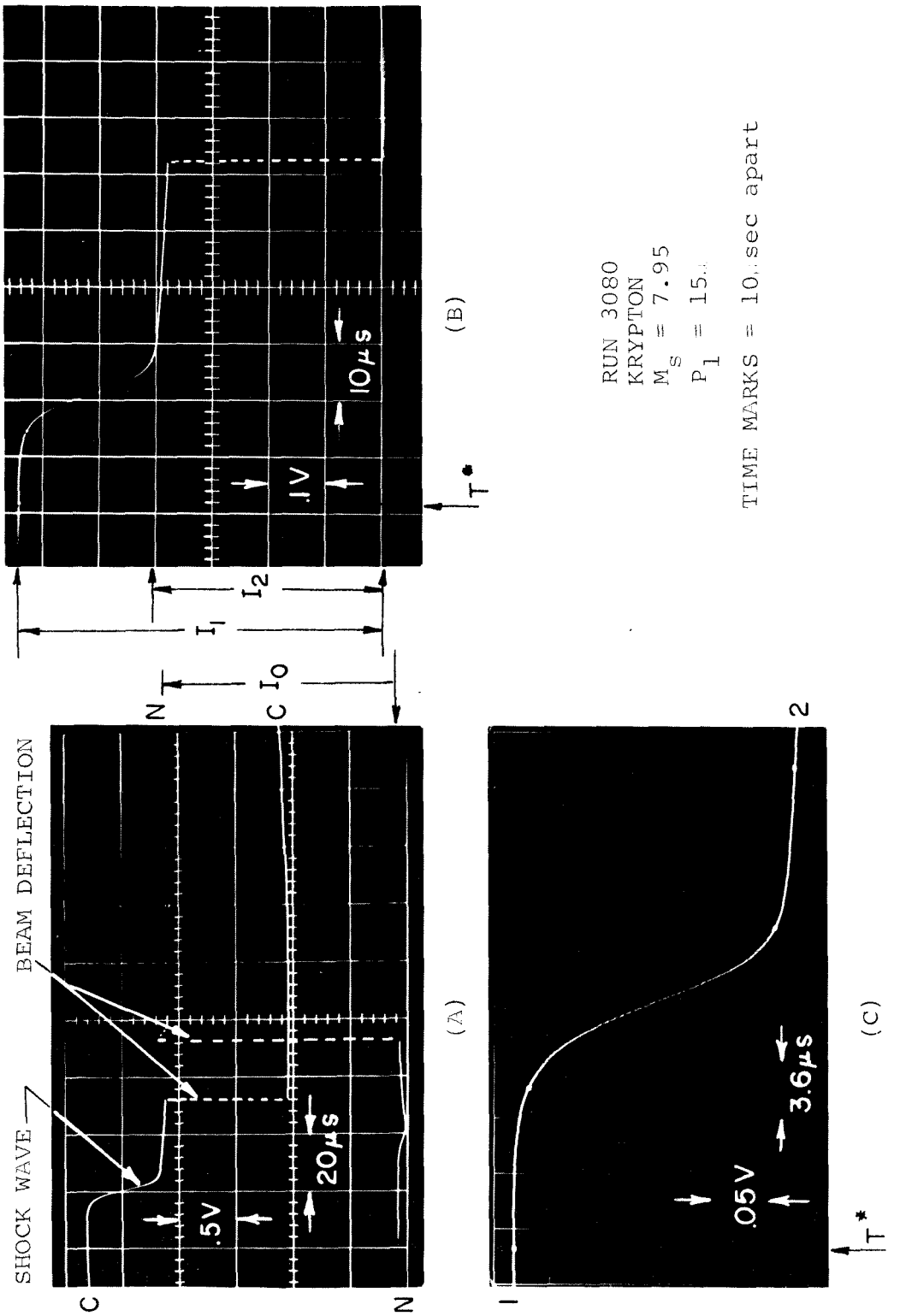

Figure 6. Typical Electron Beam Oscillograms

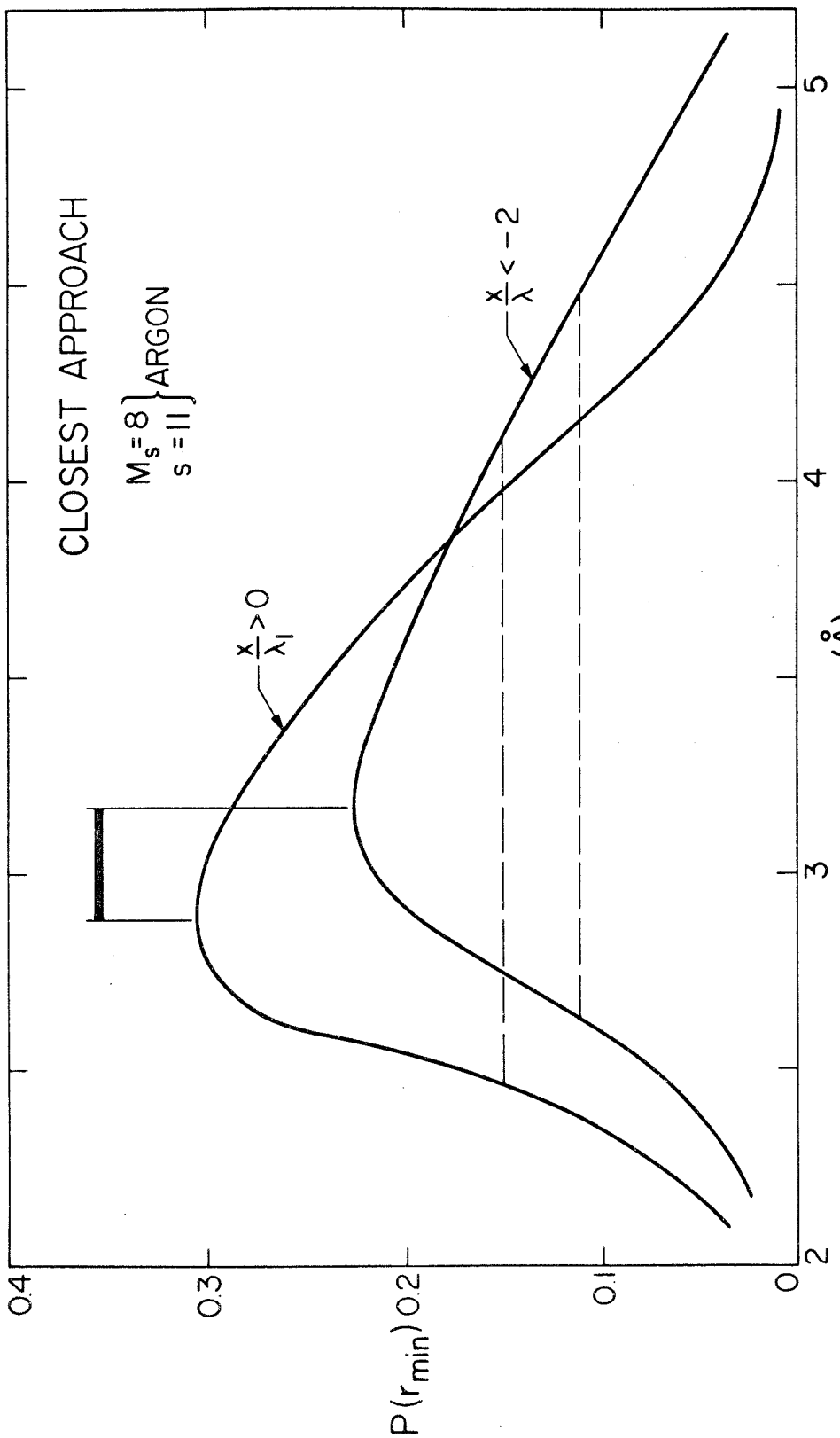

Figure 7. Distribution of Values of Closest Approach

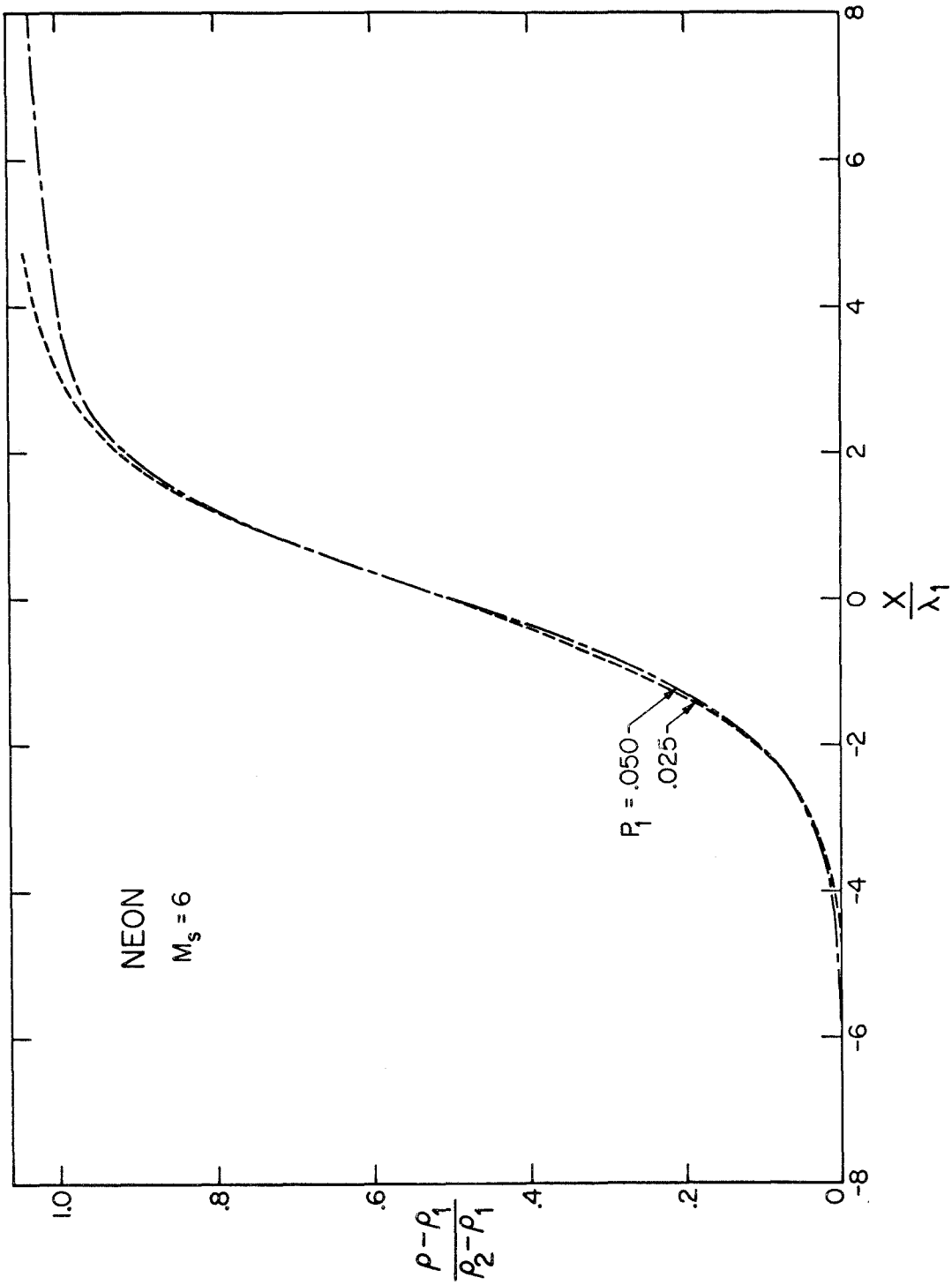

Figure 8. Effects of Initial Pressure on a Neon Shock Wave

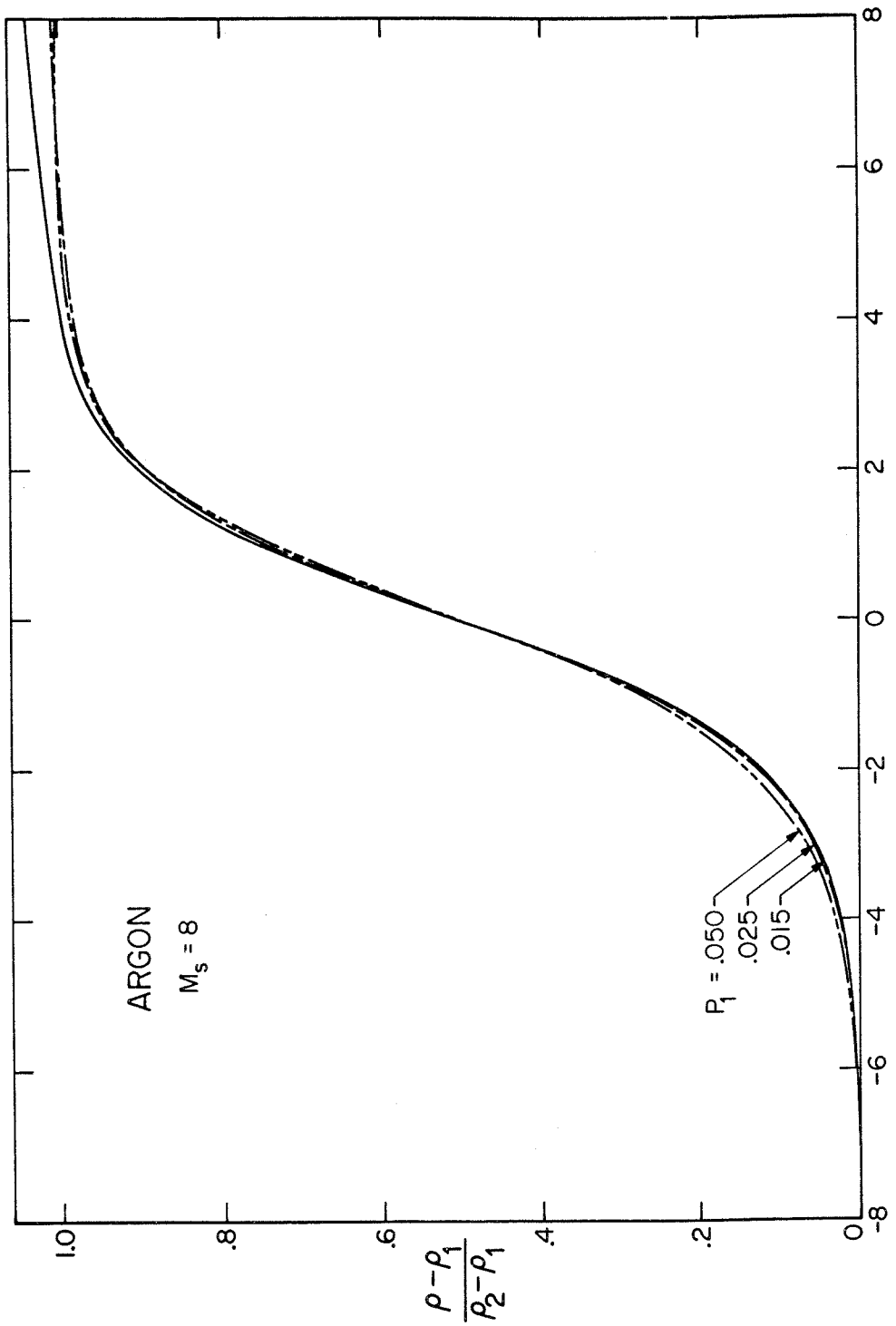

Figure 9. Effects of Initial Pressure on an Argon Shock Wave

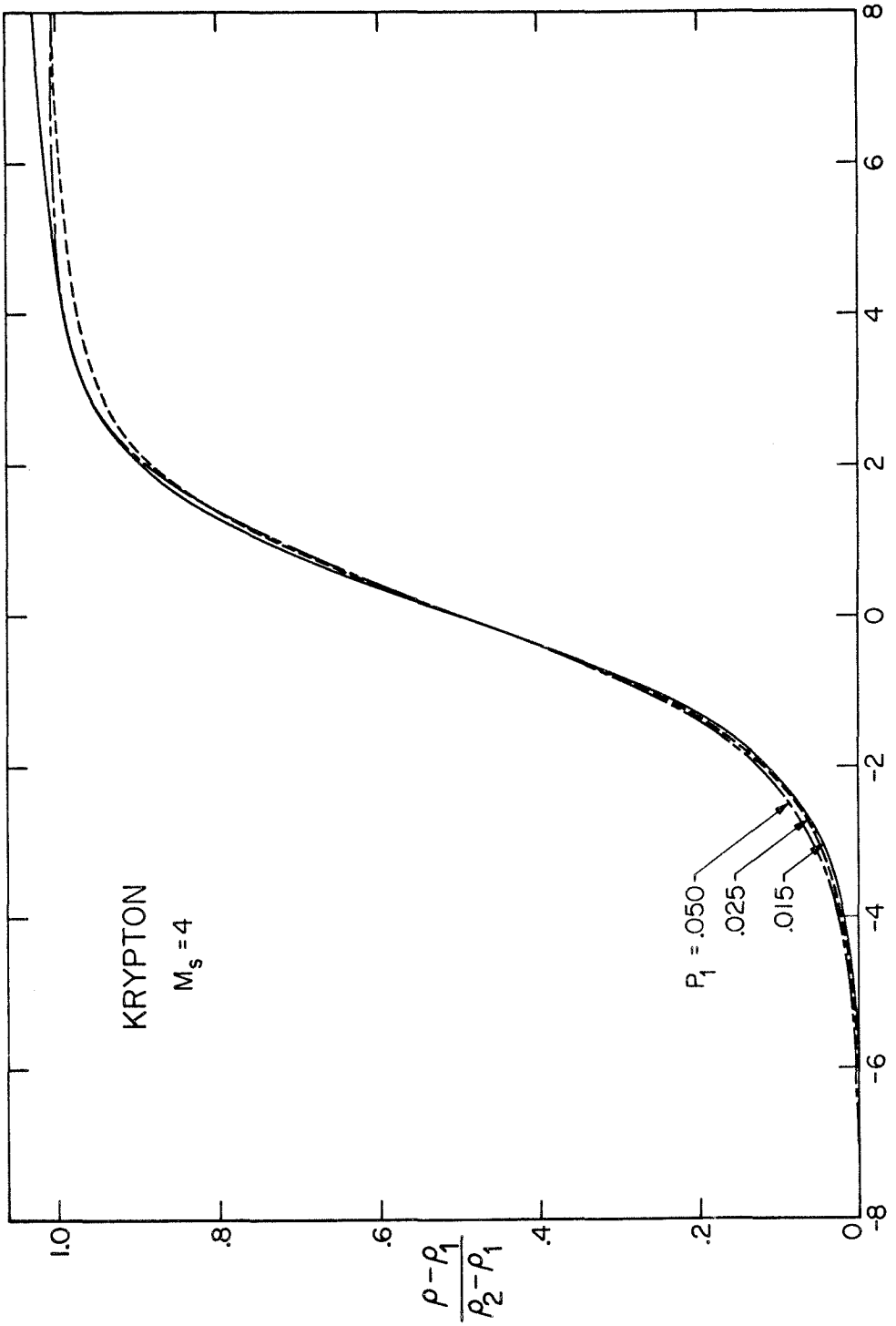

Figure 10. Effects of Initial Pressure on a Krypton Shock Wave

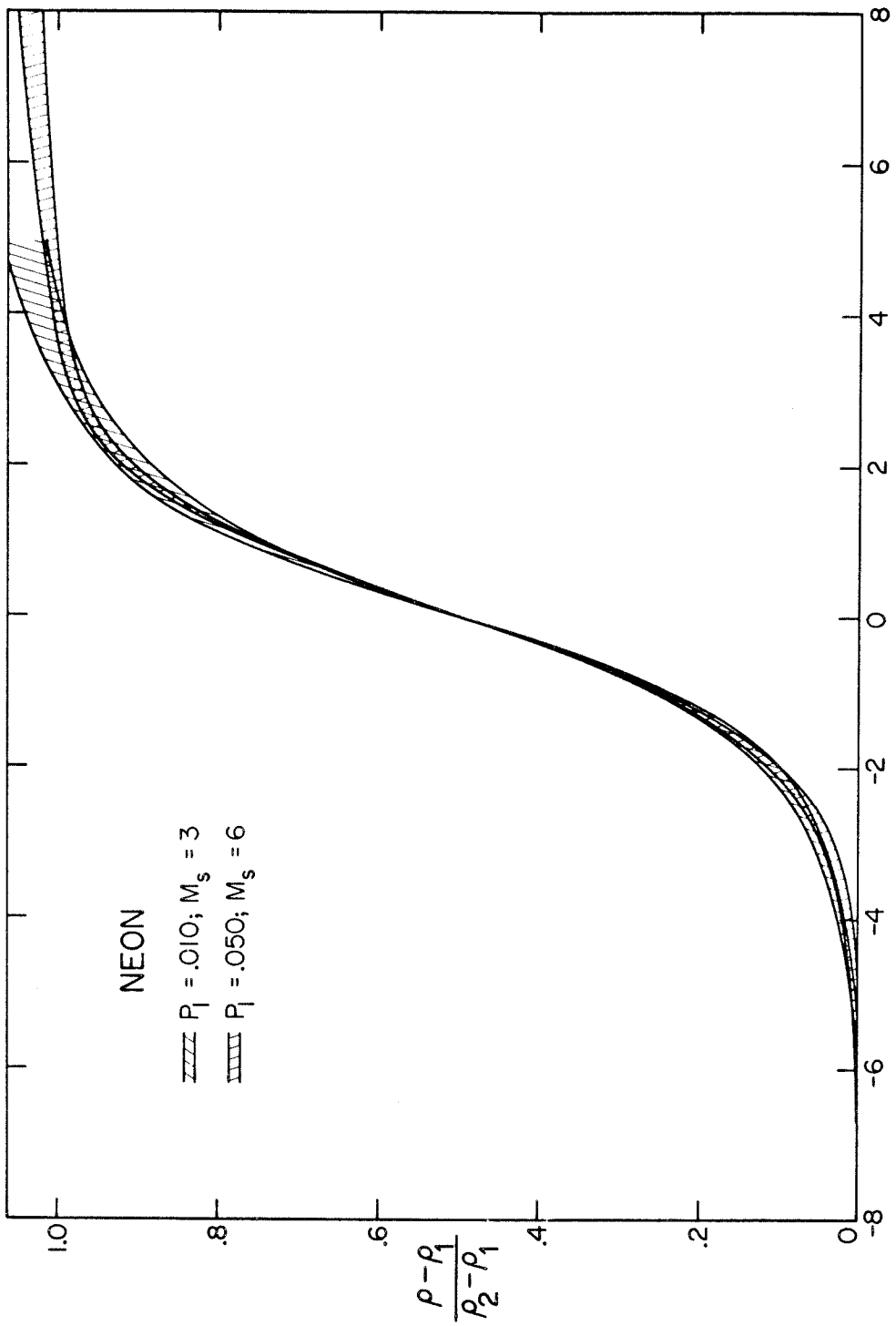

Figure 11. Experimental Scatter for a Neon Shock Wave

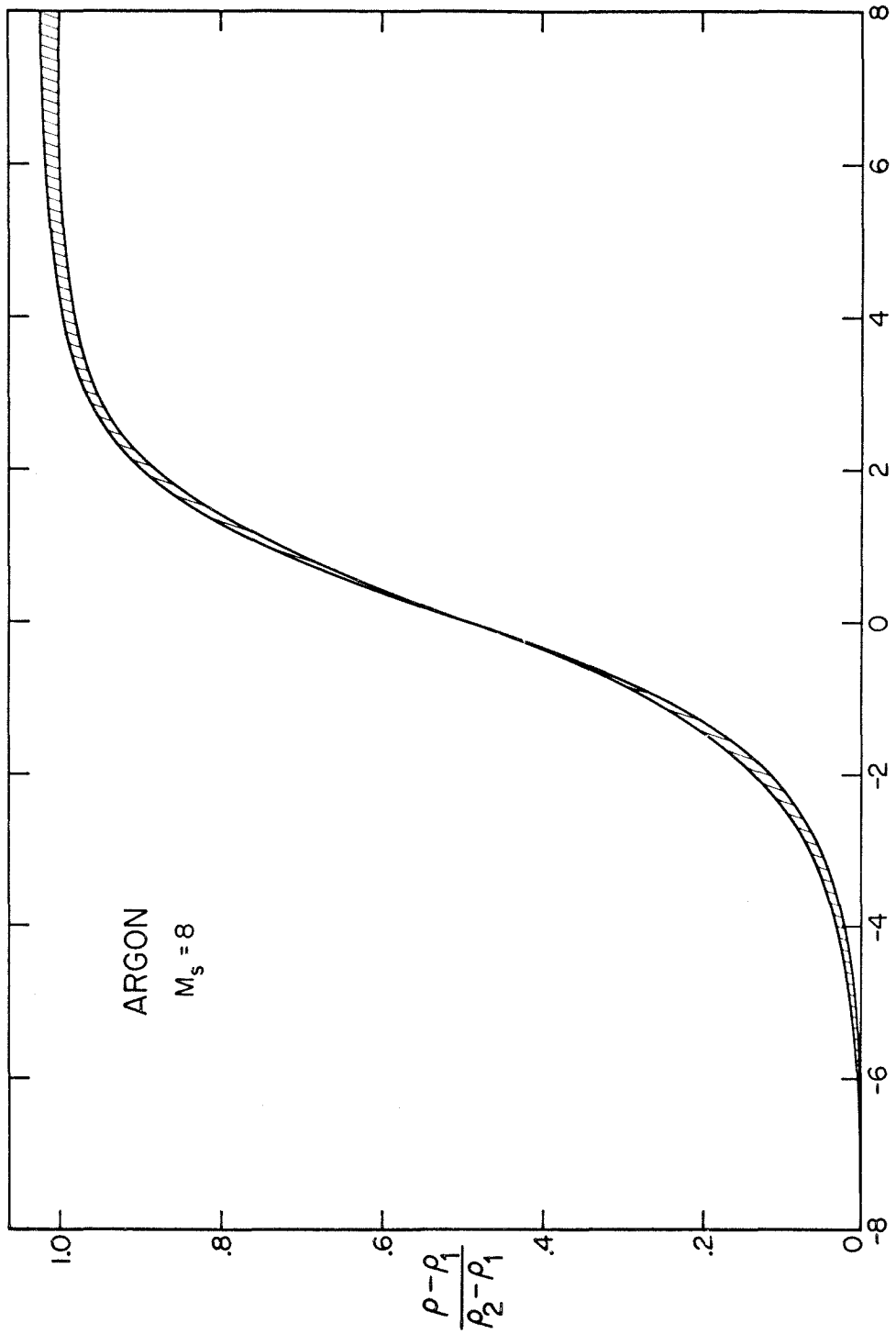

Figure 12. Experimental Scatter for an Argon Shock Wave

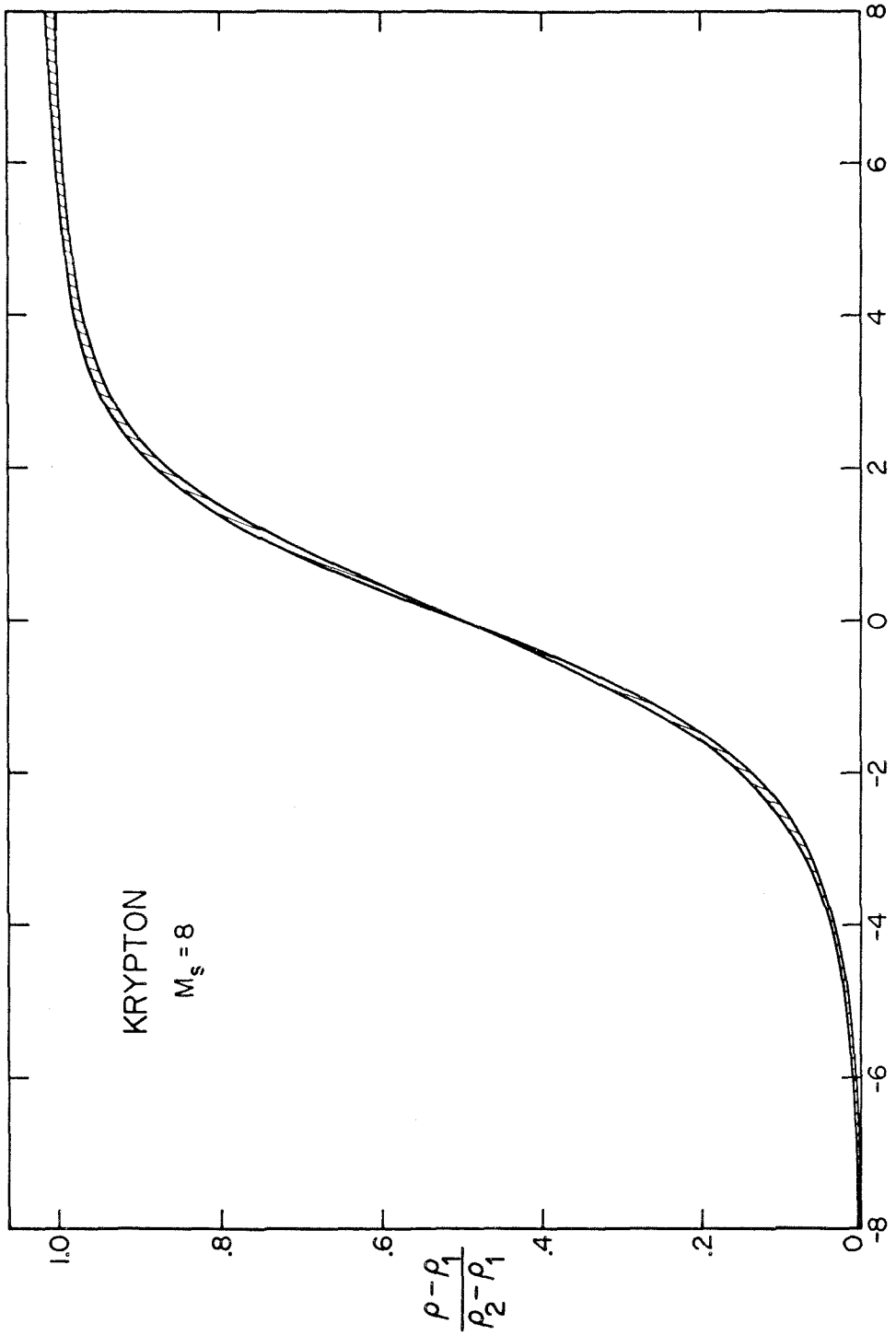

Figure 13. Experimental Scatter for a Krypton Shock Wave

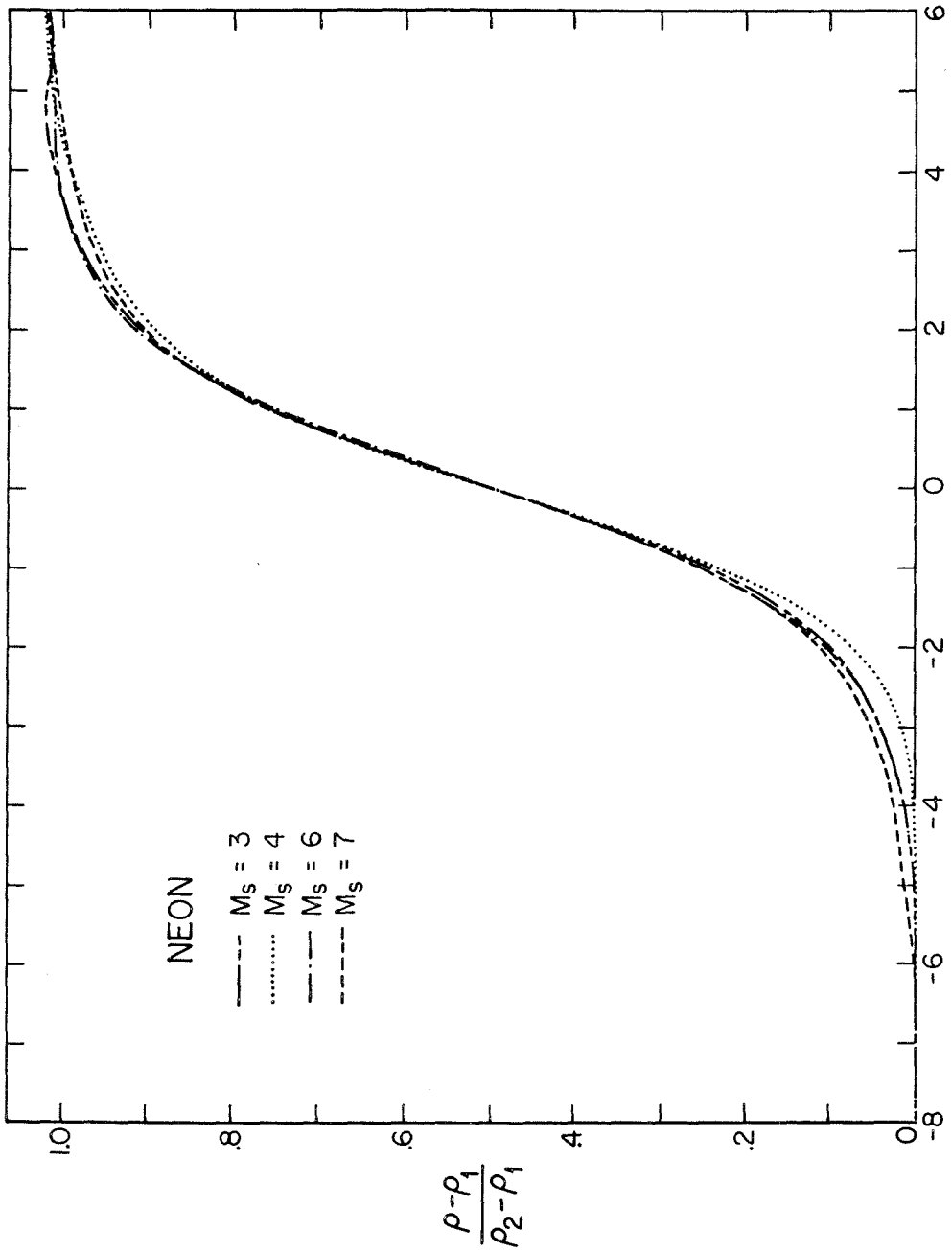

Figure 14. Effect of Mach Number on a Neon Shock Wave

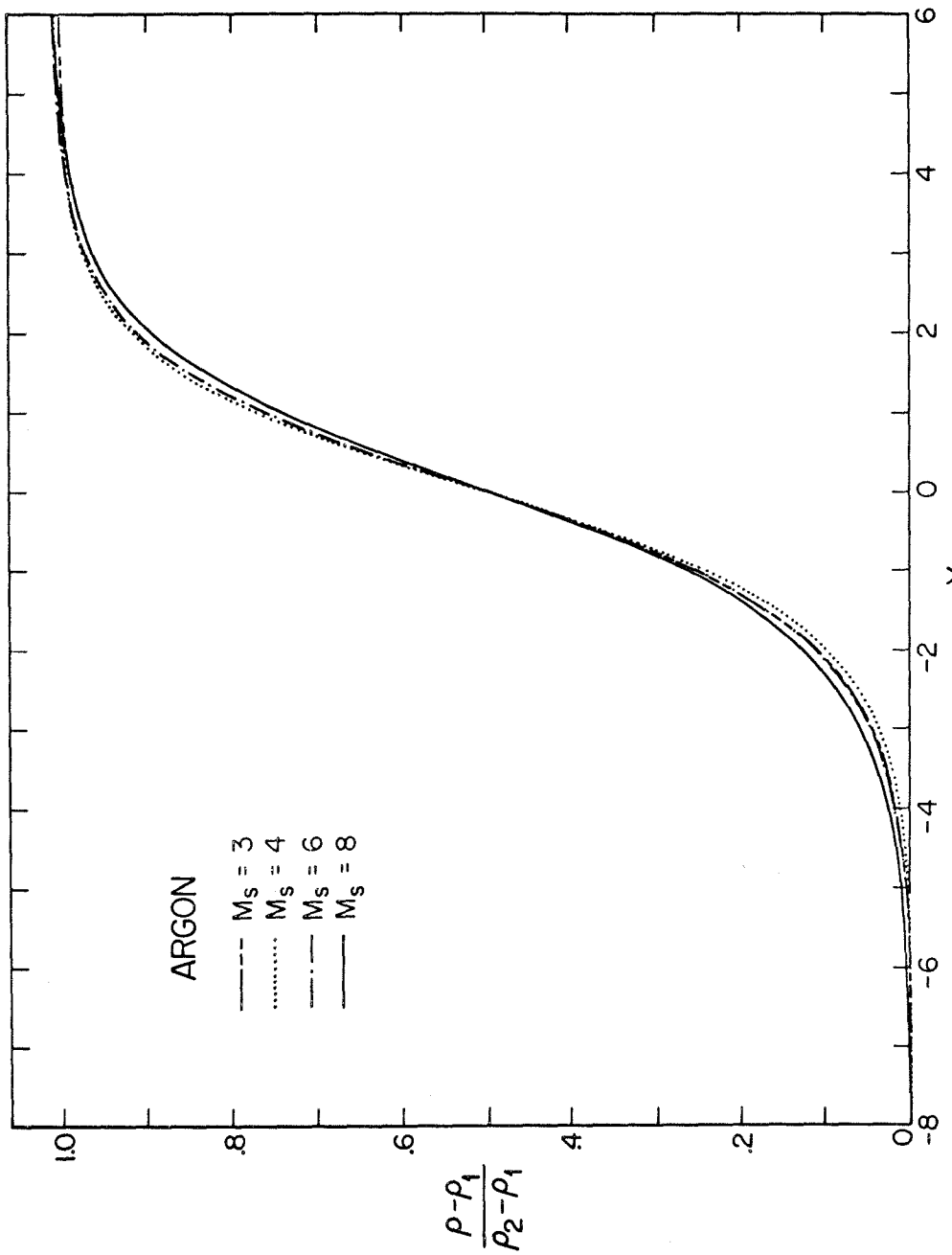

Figure 15. Effect of Mach Number on an Argon Shock Wave

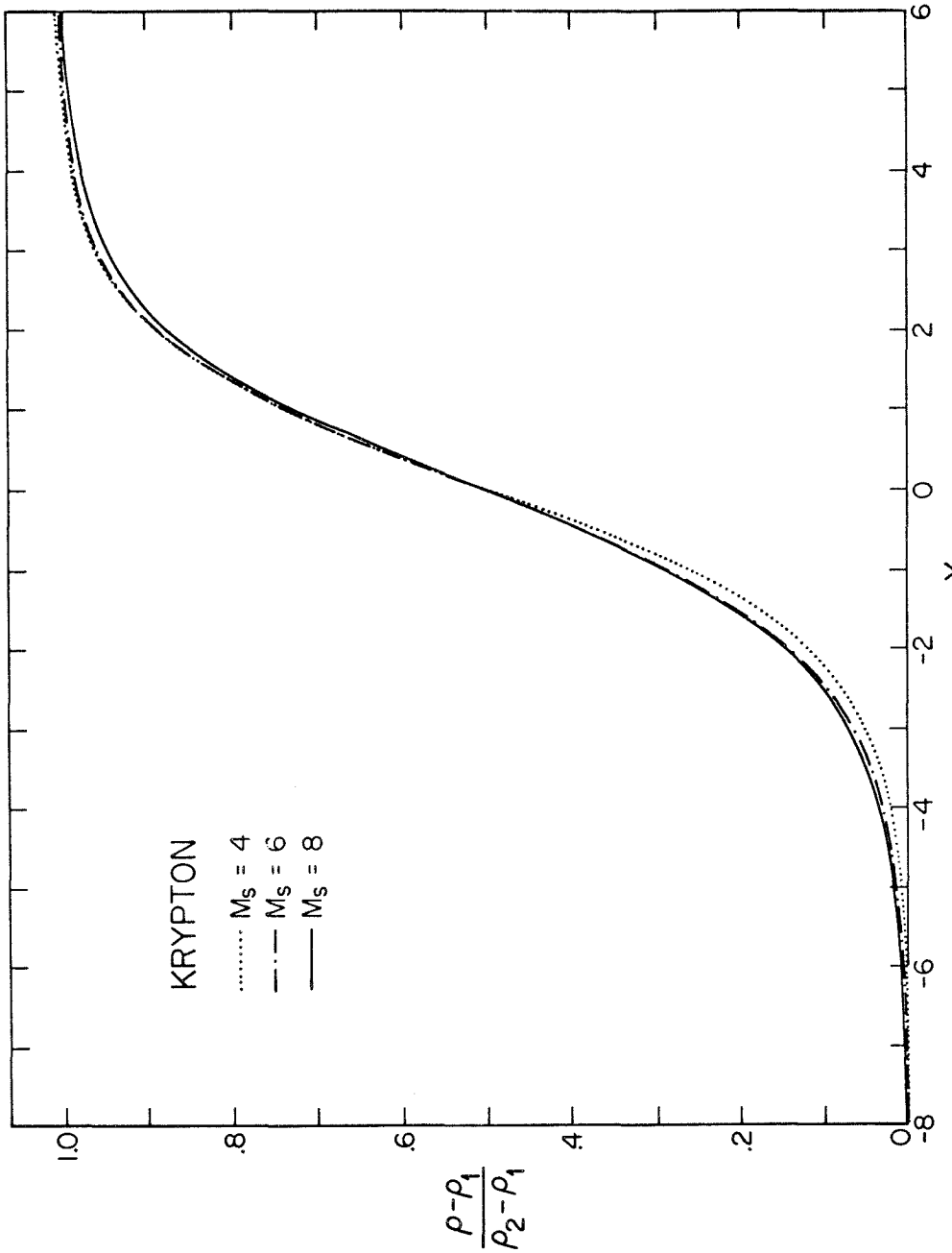

Figure 16. Effect of Mach Number on a Krypton Shock Wave

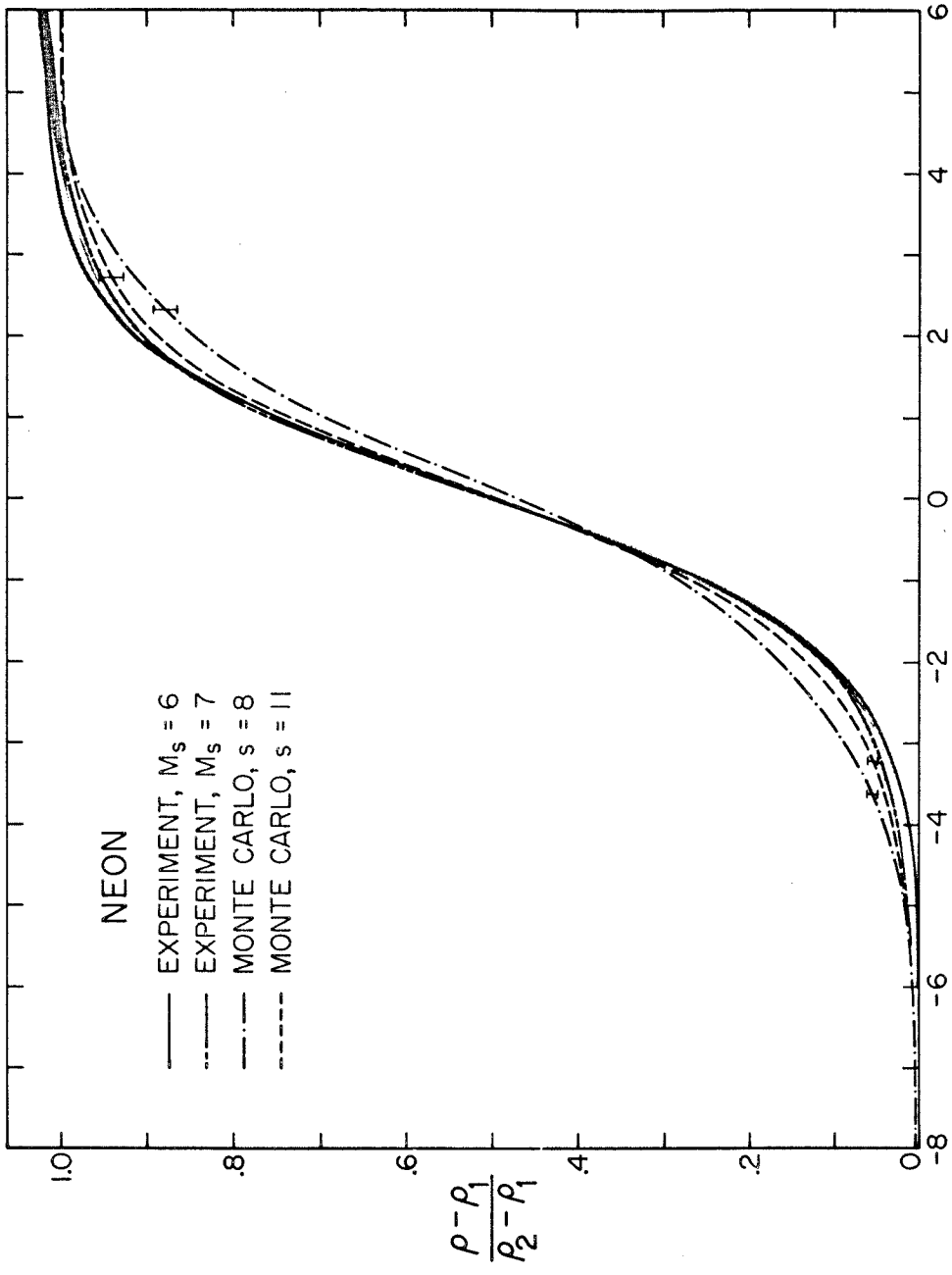

Figure 17. Comparison of Experimental and Numerical Shock Profiles for Neon

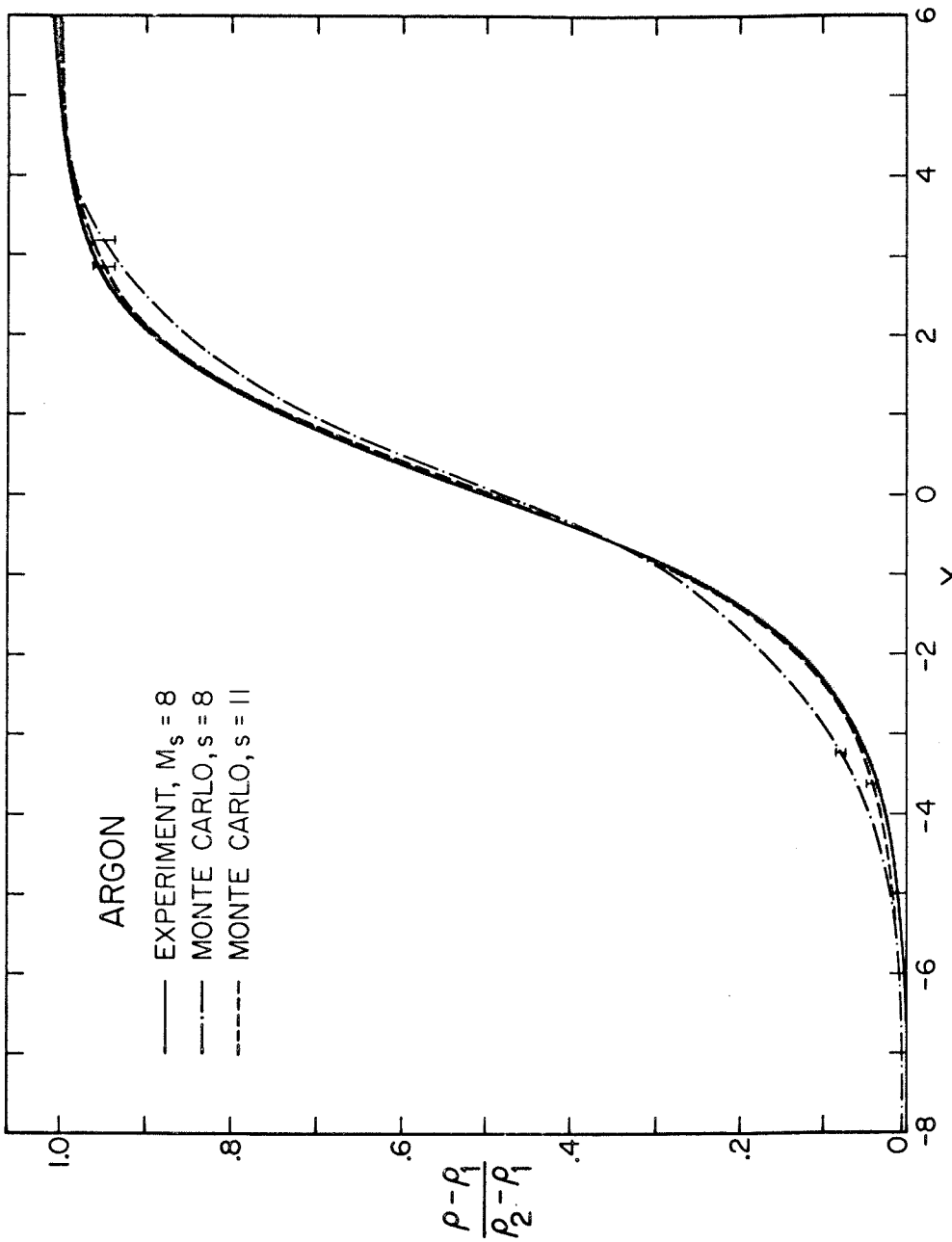

Figure 18. Comparison of Experimental and Numerical Shock Profiles for Argon

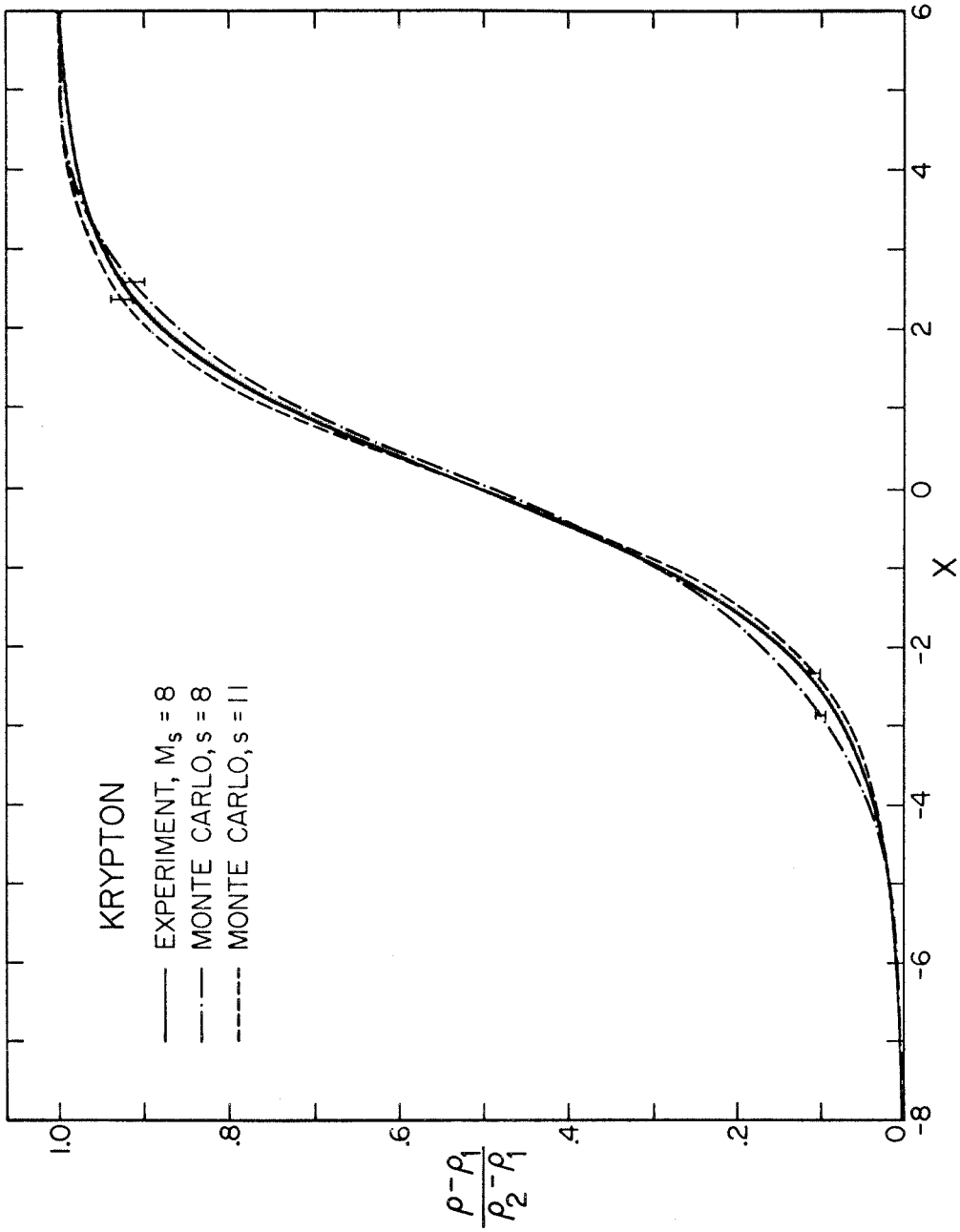

Figure 19. Comparison of Experimental and Numerical Shock Profiles for Krypton

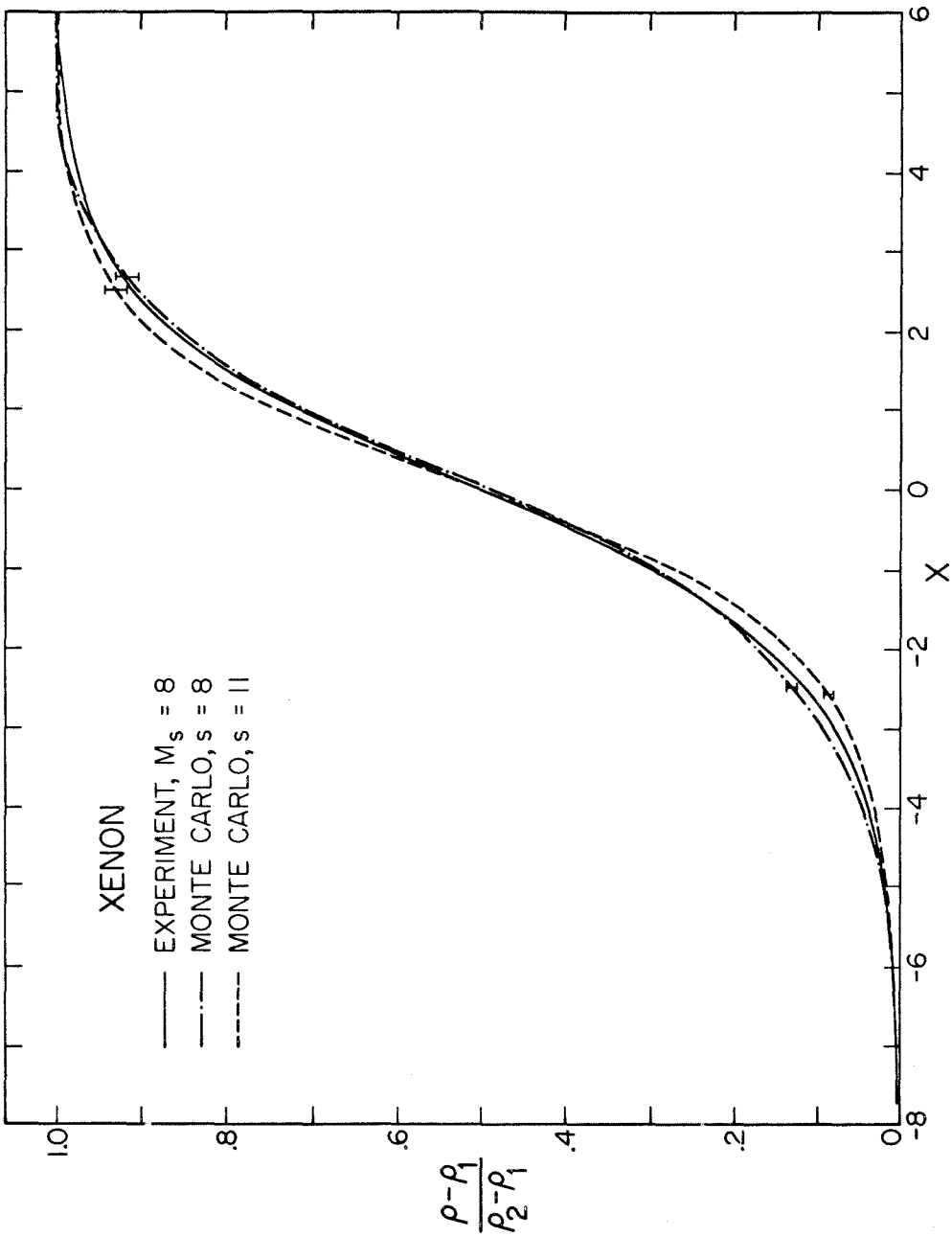

Figure 20. Comparison of Experimental and Numerical Shock Profiles for Xenon

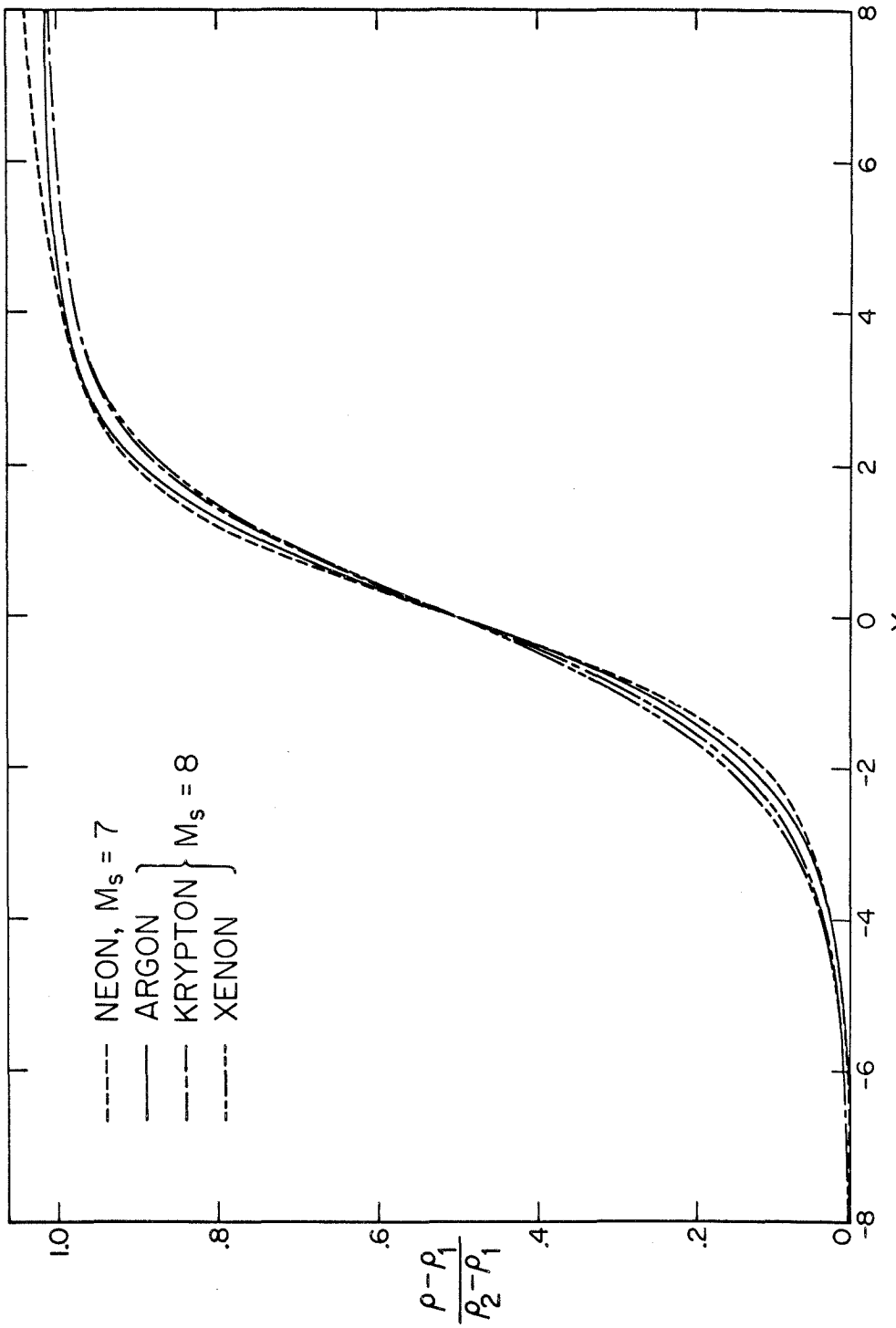

Figure 21. Experimental Shock Profiles of Neon, Argon, Krypton, and Xenon

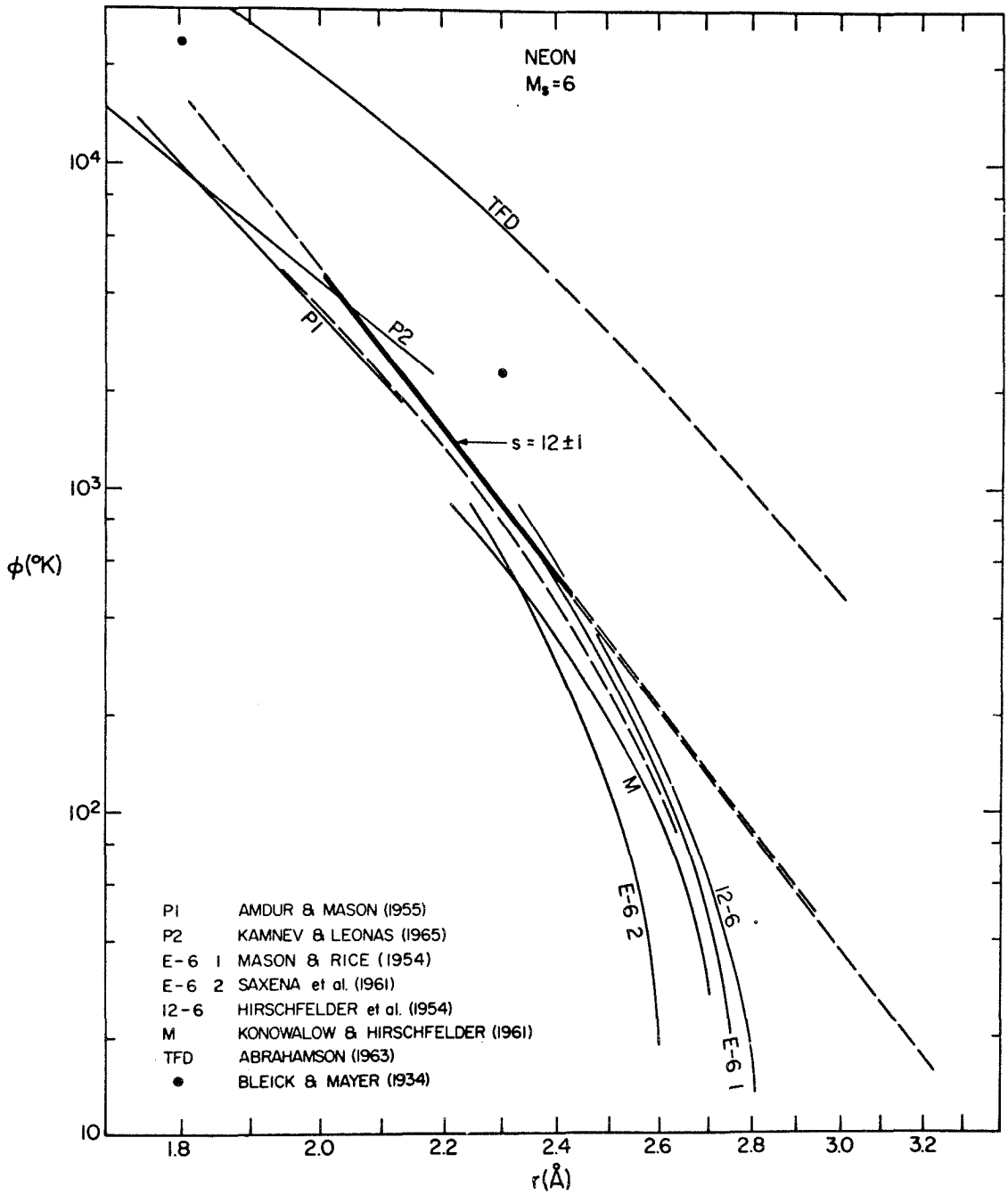

Figure 22. Neon Interaction Potential

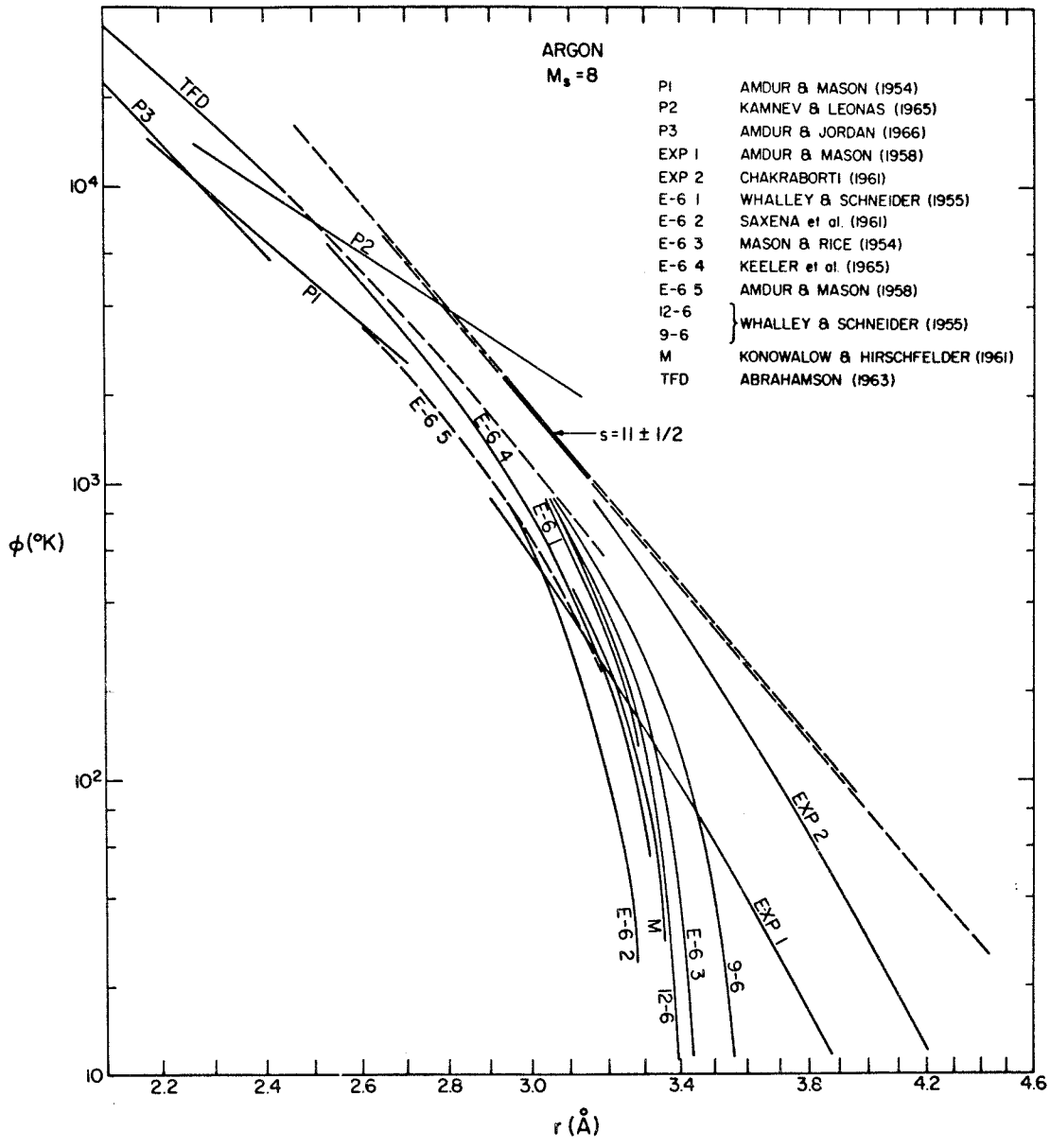

Figure 23. Argon Interaction Potential

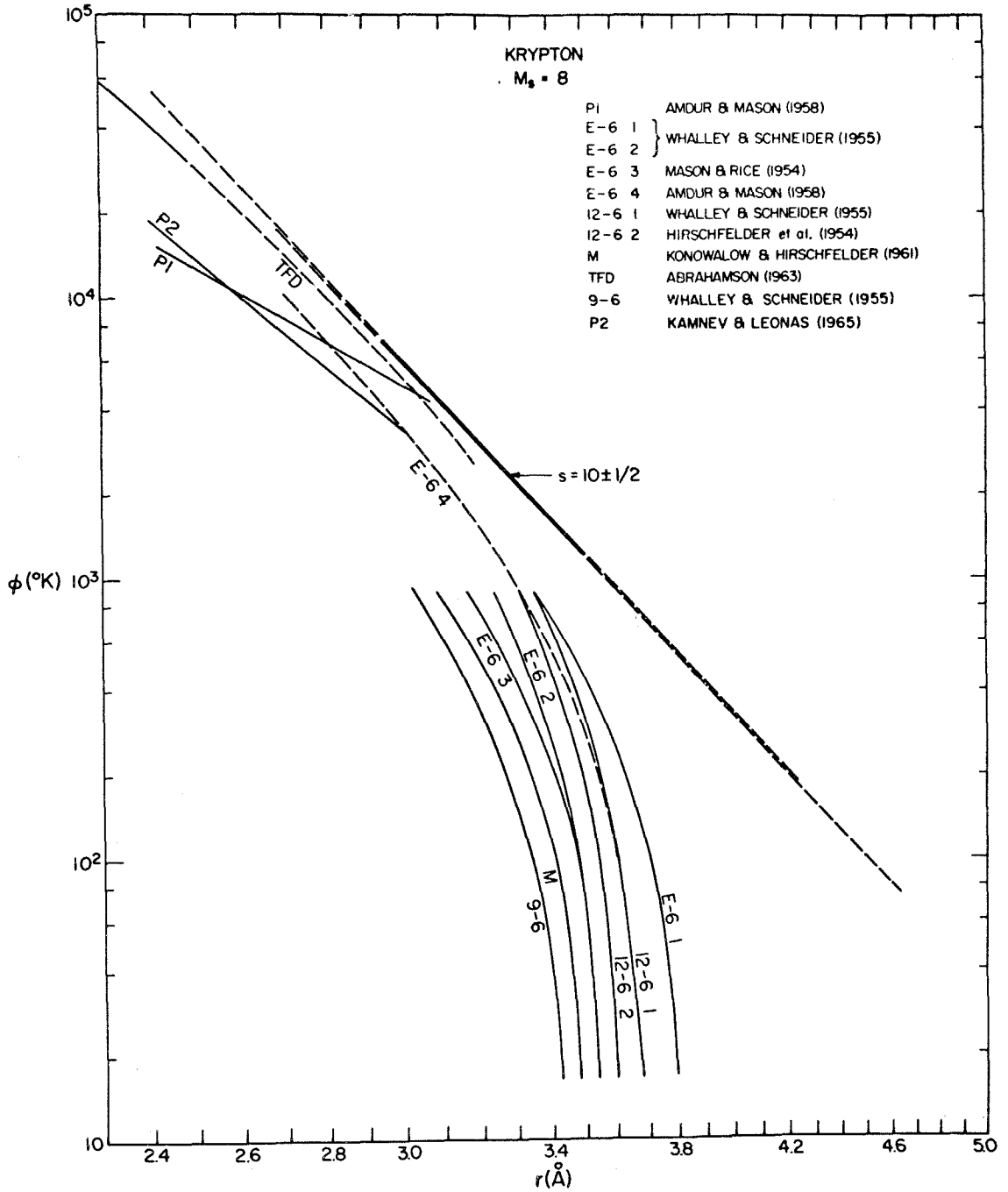

Figure 24. Krypton Interaction Potential

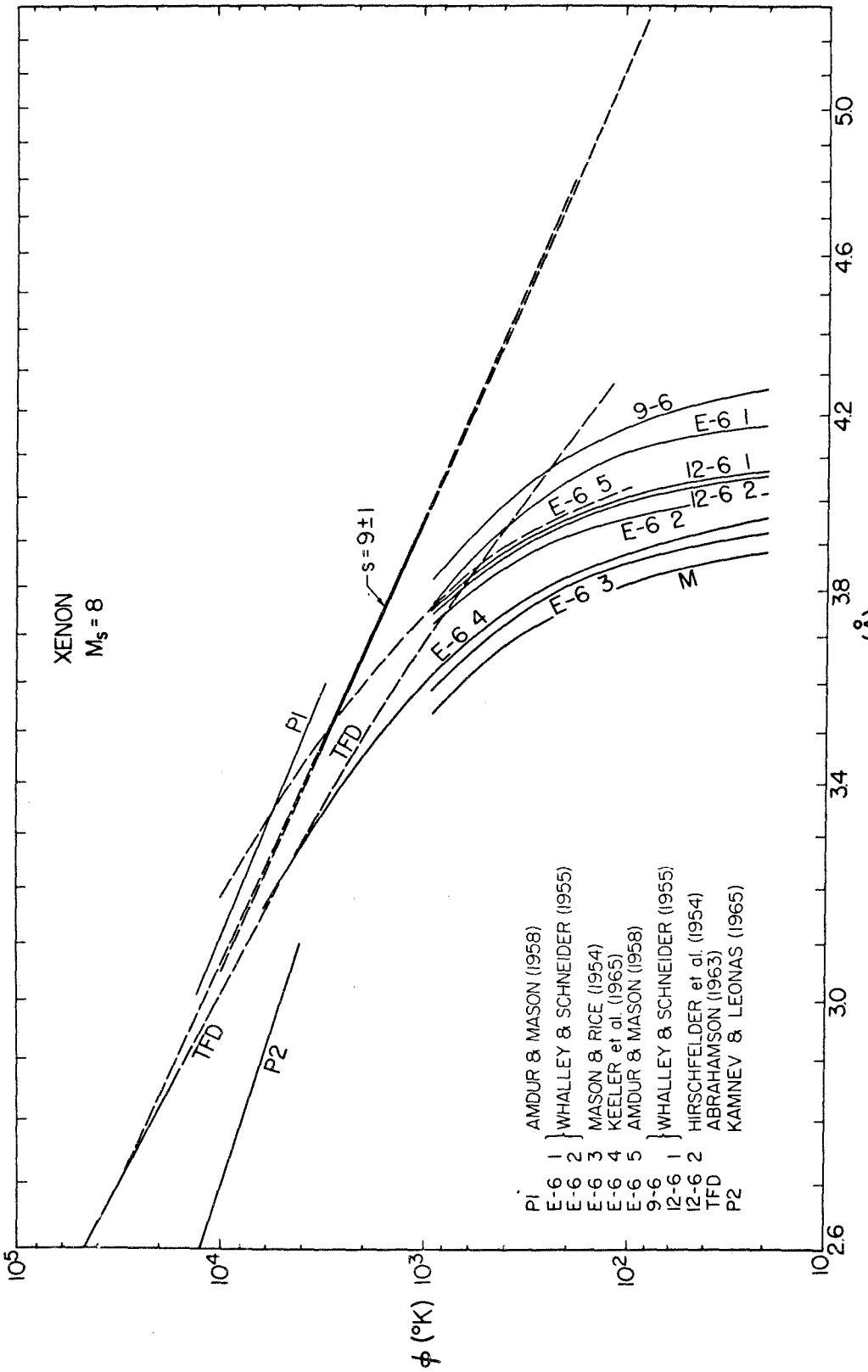

Figure 25. Xenon Interaction Potential

Figure 26

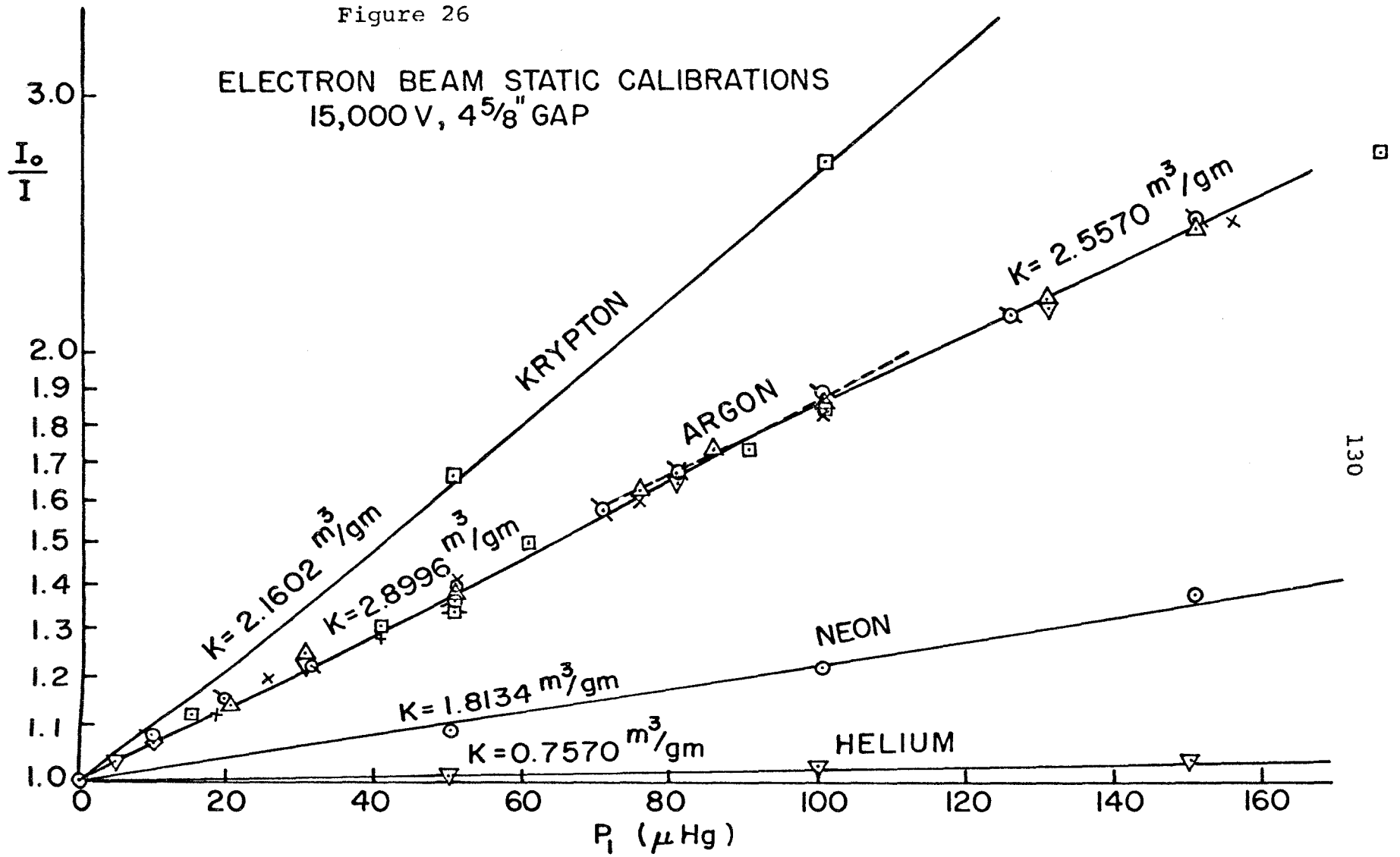
ELECTRON BEAM STATIC CALIBRATIONS
15,000 V, 4 5/8" GAP
$\frac{I_o}{I}$
3.0
2.0
1.9
1.8
1.7
1.6
1.5
1.4
1.3
1.2
1.1
1.0
KRYPTON
K= 2.1602 m³/gm
ARGON
K= 2.8996 m³/gm
K= 2.5570 m³/gm
NEON
K= 1.8134 m³/gm
HELIUM
K= 0.7570 m³/gm
0
20
40
60
80
100
120
140
160
P_1 (μHg)

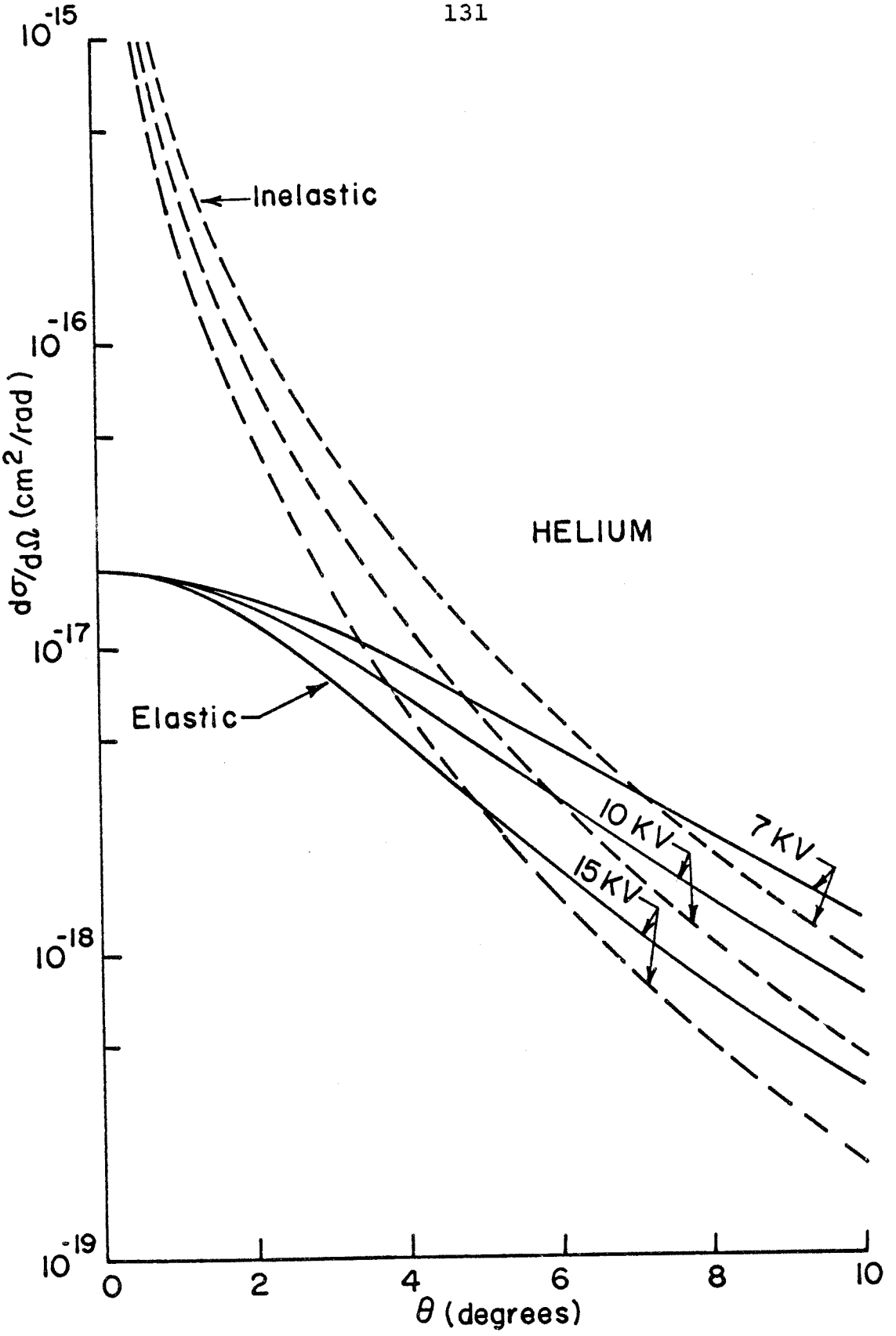

DIFFERENTIAL CROSS-SECTION

Figure 27

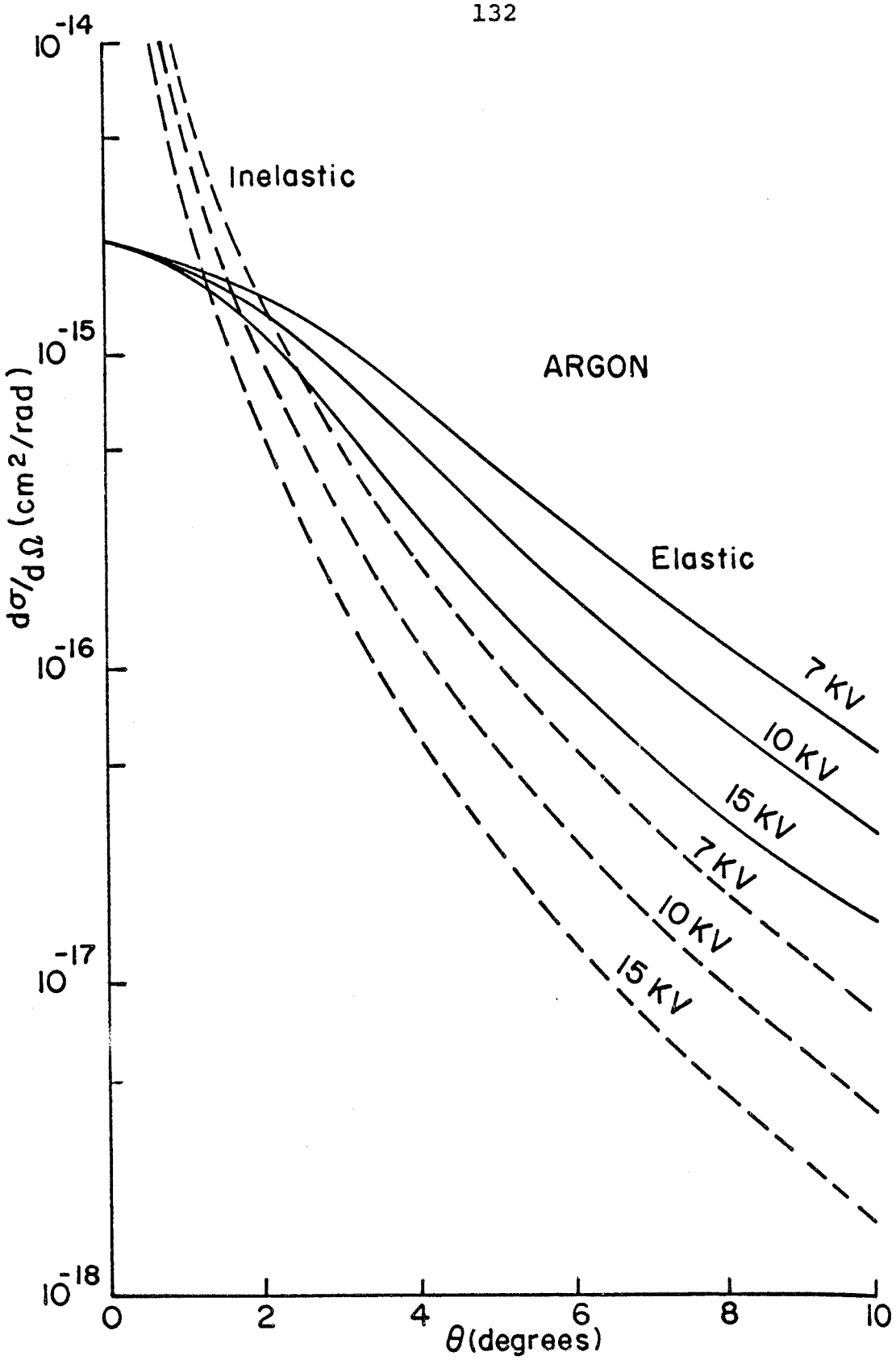

DIFFERENTIAL CROSS-SECTION

Figure 28

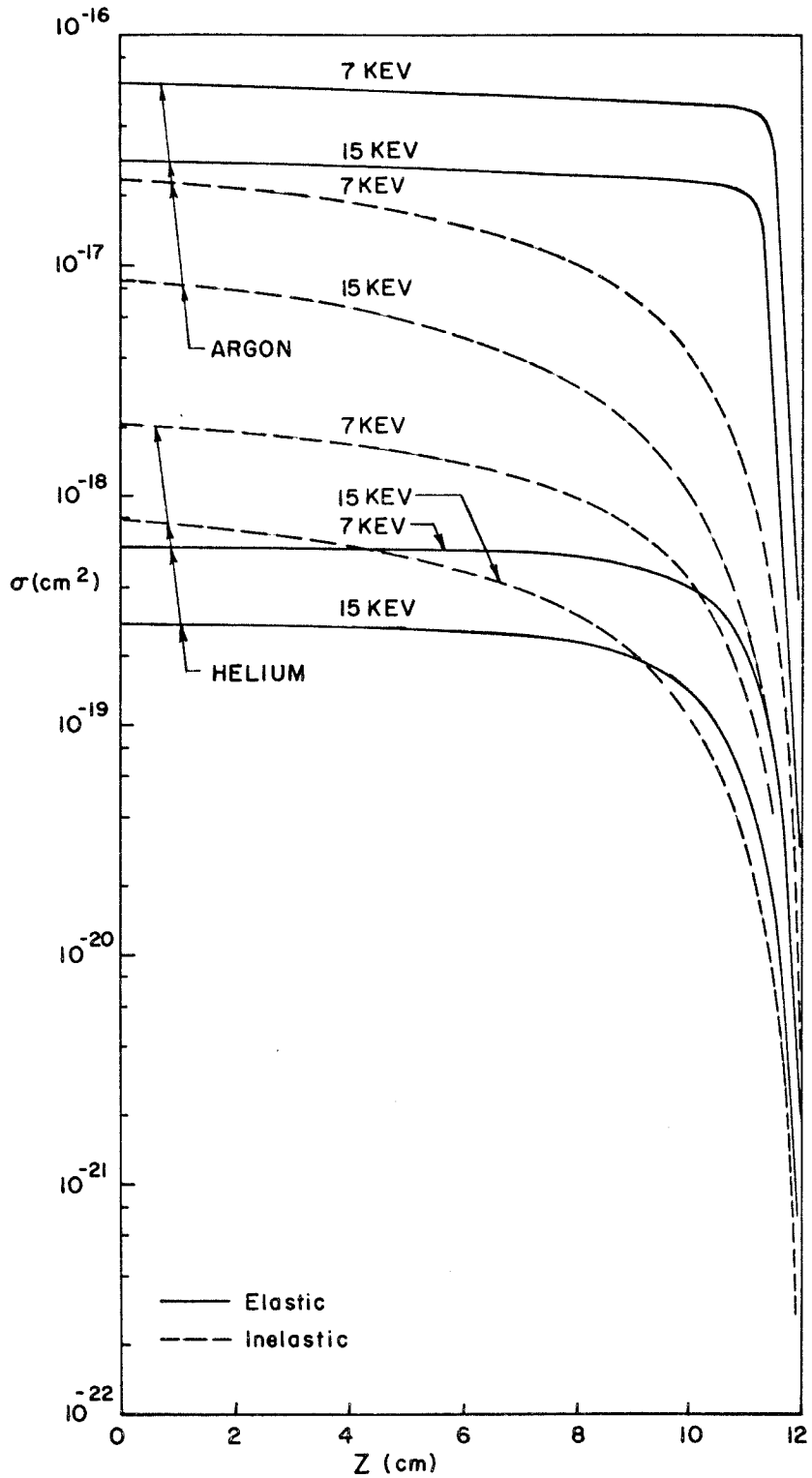

TOTAL CROSS-SECTION

Figure 29

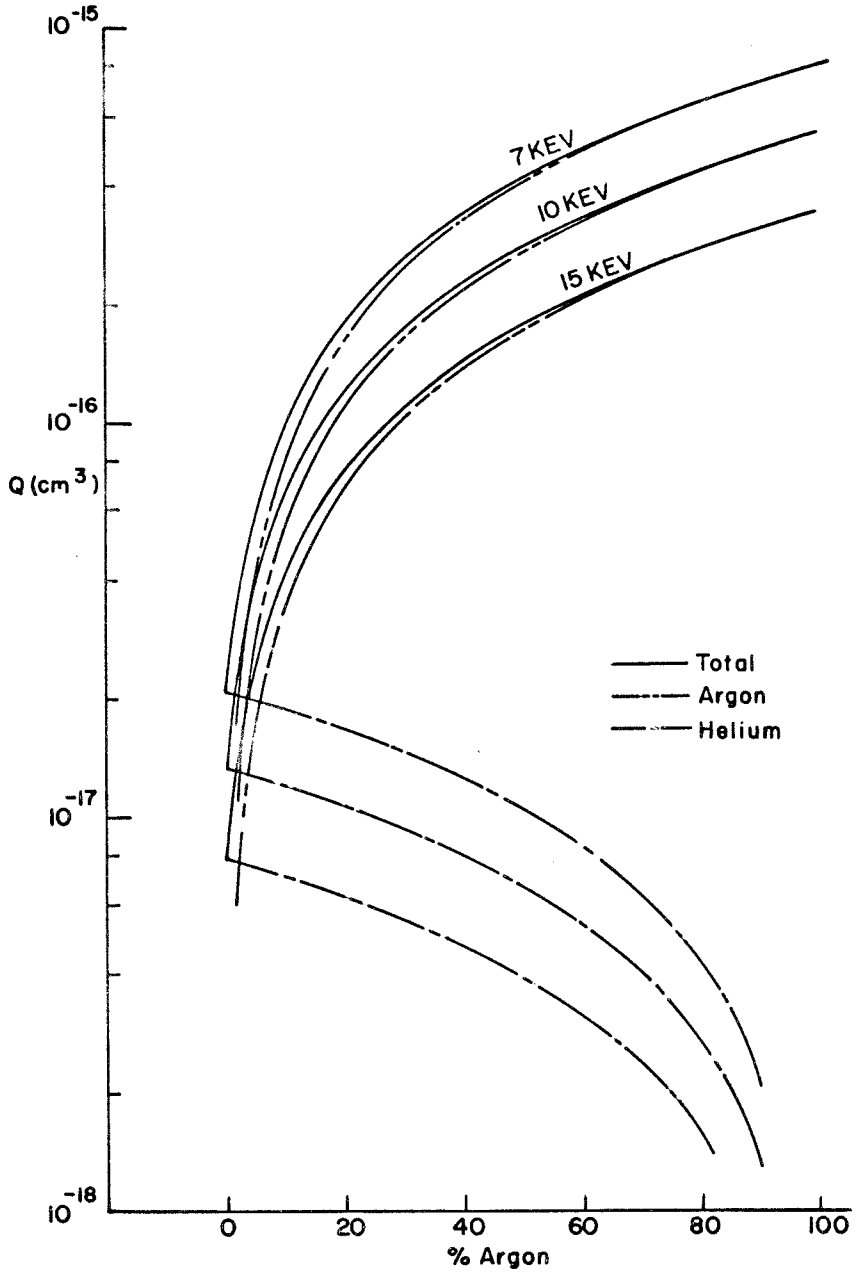

CROSS SECTIONAL MOMENT

Figure 30

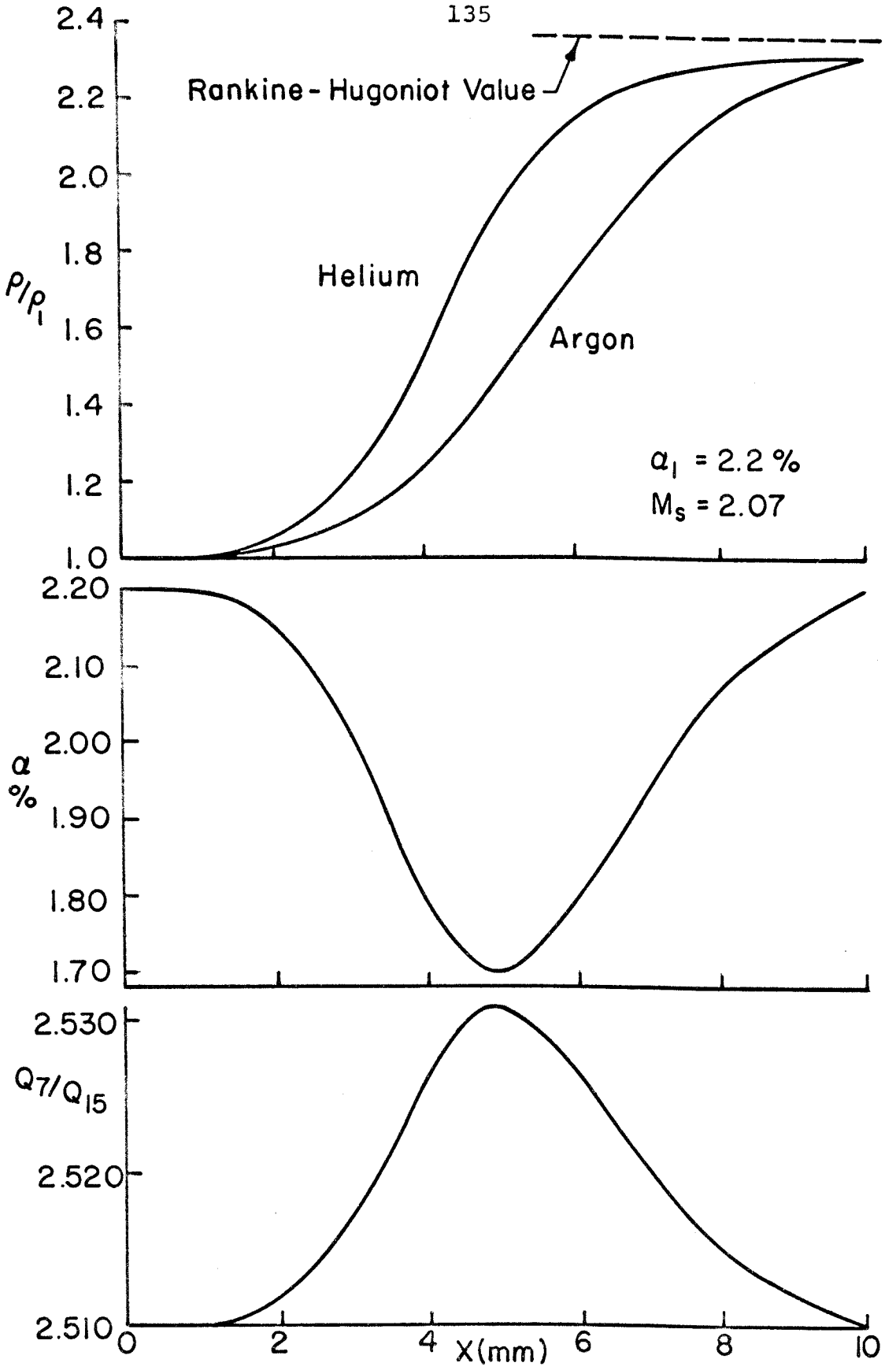

Figure 31. Density, Concentration, and Moment Ratio Variations for a 2.2% Argon Shock Wave

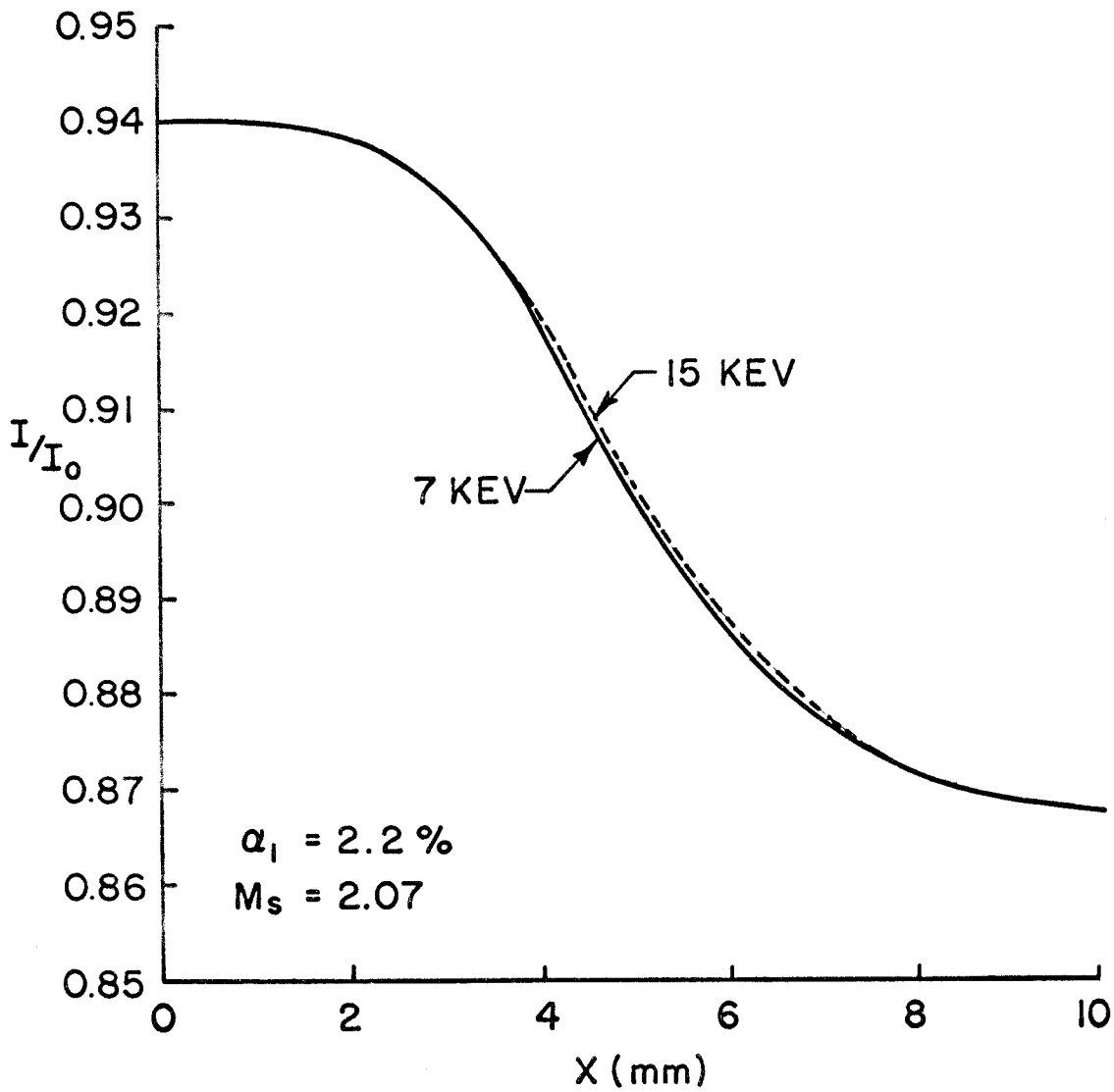

Figure 32. Theoretical Collector Current for a 2.2% Argon Mixture

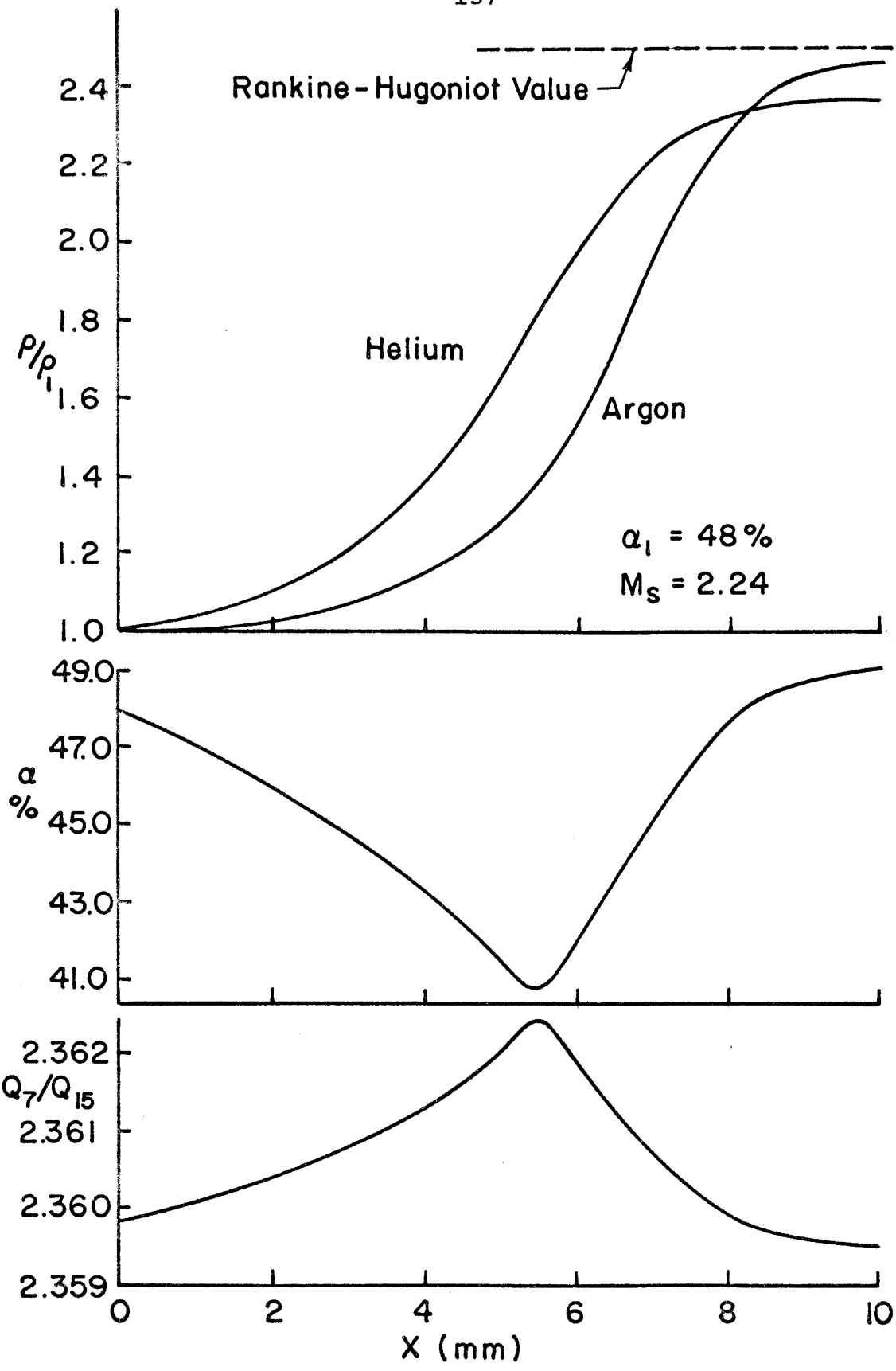

Figure 33. Density, Concentration, and Moment Ratio Variations for a 48% Argon Shock Wave

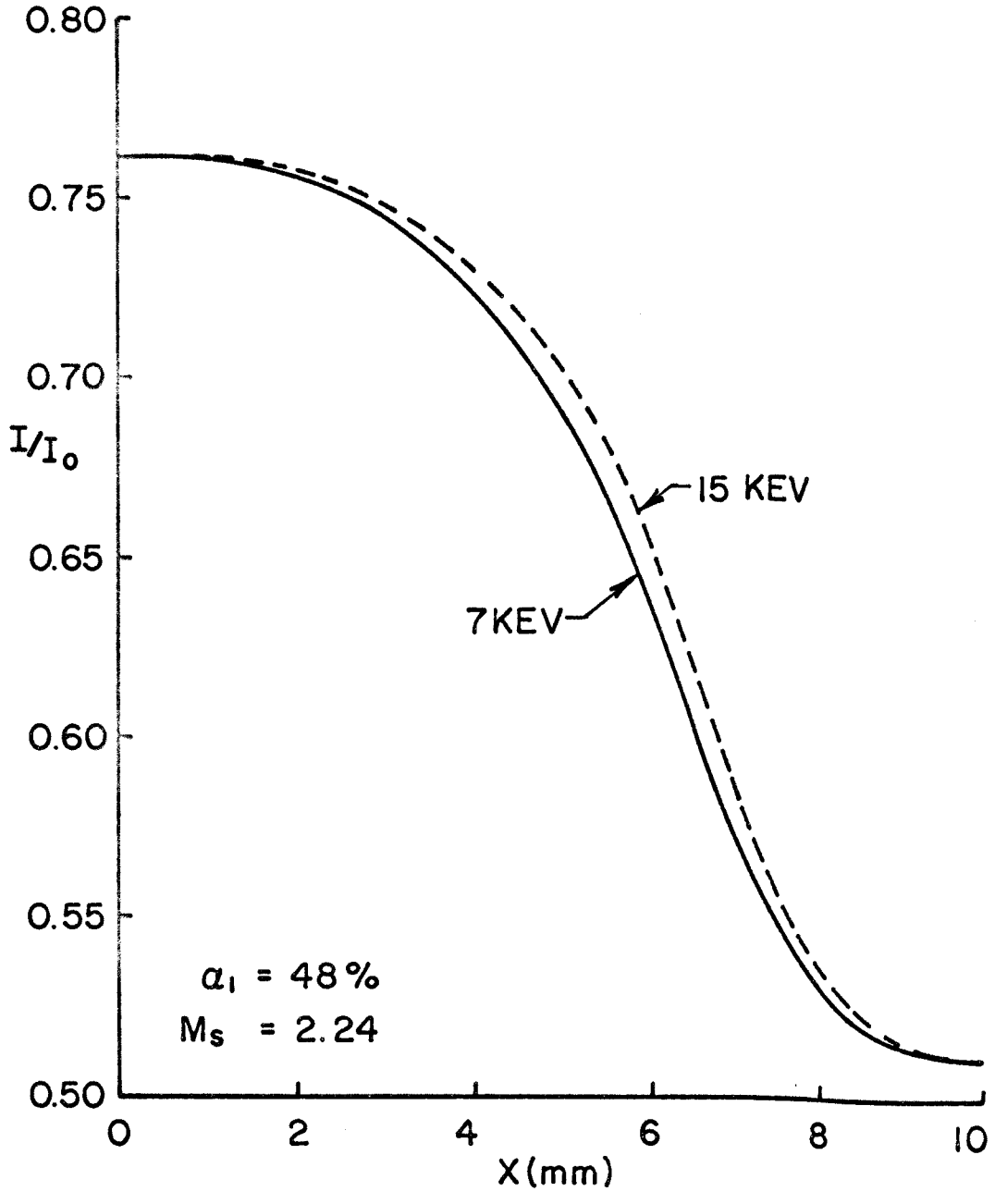

Figure 34. Theoretical Collector Current for a 48% Argon Mixture

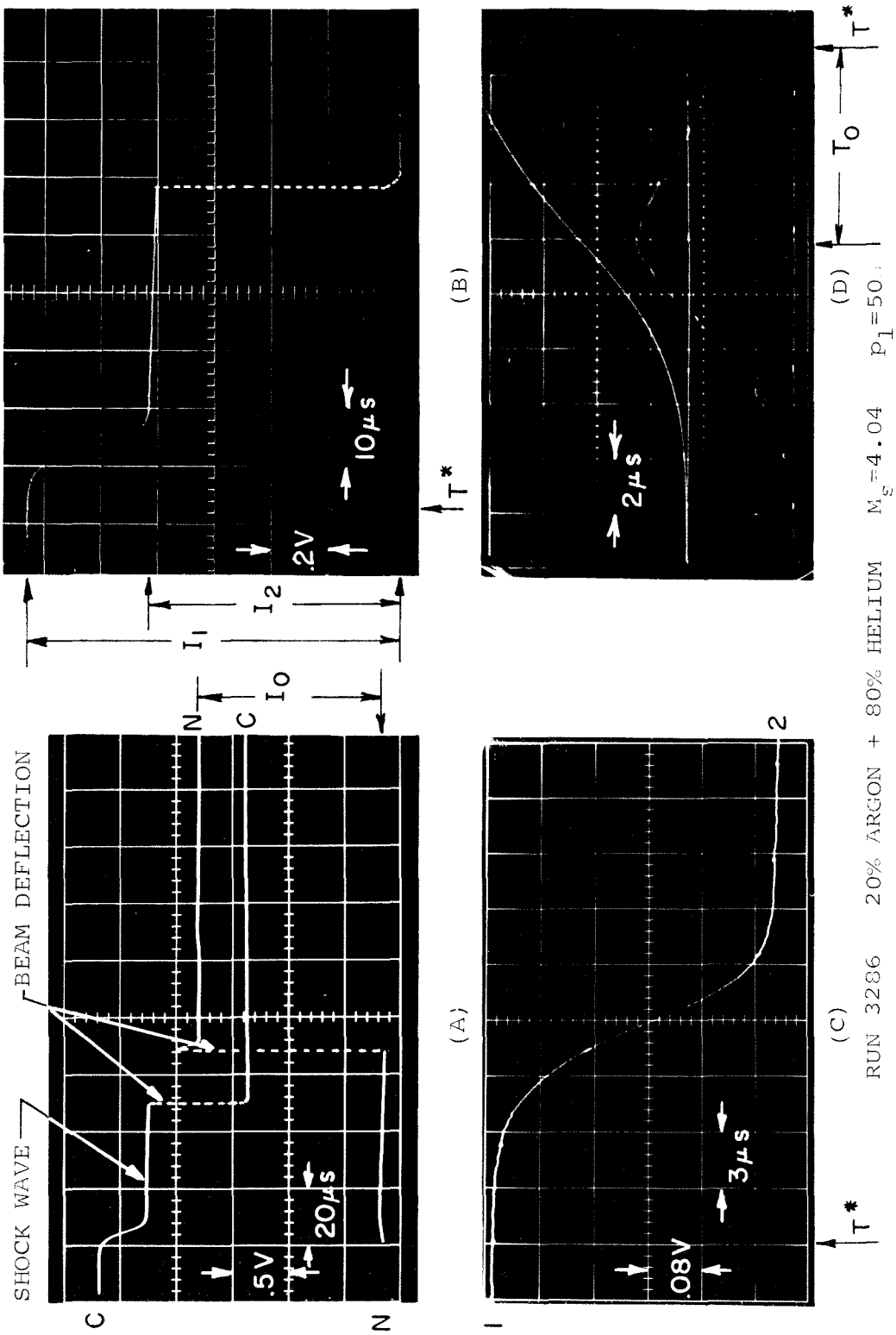

Figure 35. Typical Electron Beam Oscillograms

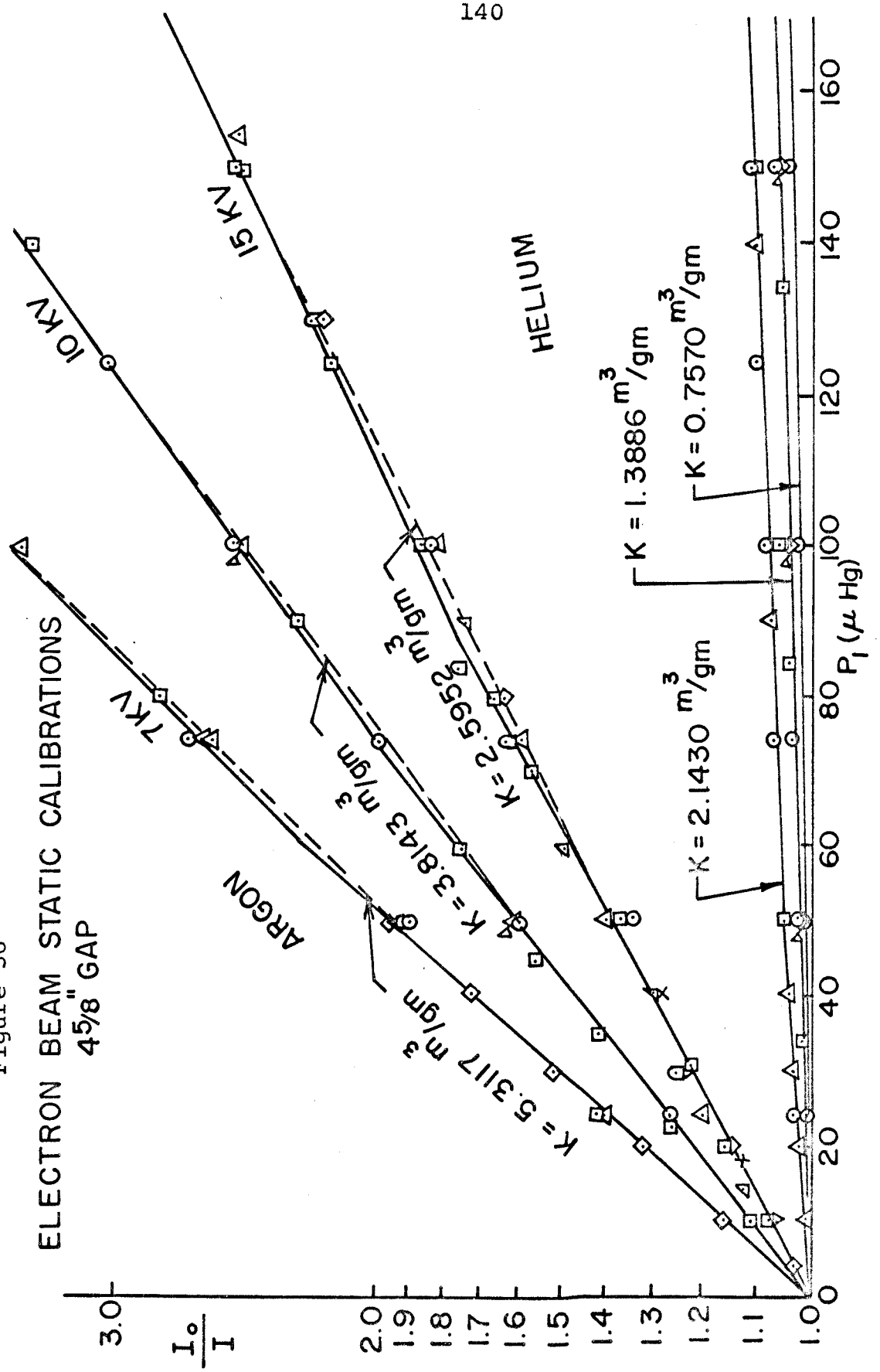
ELECTRON BEAM STATIC CALIBRATIONS
45/8" GAP
ARGON
HELIUM
7 KV
10 KV
15 KV
K = 5.3117 m³/gm
K = 3.8143 m³/gm
K = 2.9552 m³/gm
K = 2.1430 m³/gm
K = 1.3886 m³/gm
K = 0.7570 m³/gm
I₀/I
P₁ (μ Hg)
3.0
2.0
1.9
1.8
1.7
1.6
1.5
1.4
1.3
1.2
1.1
1.0
0
20
40
60
80
100
120
140
160

Figure 36

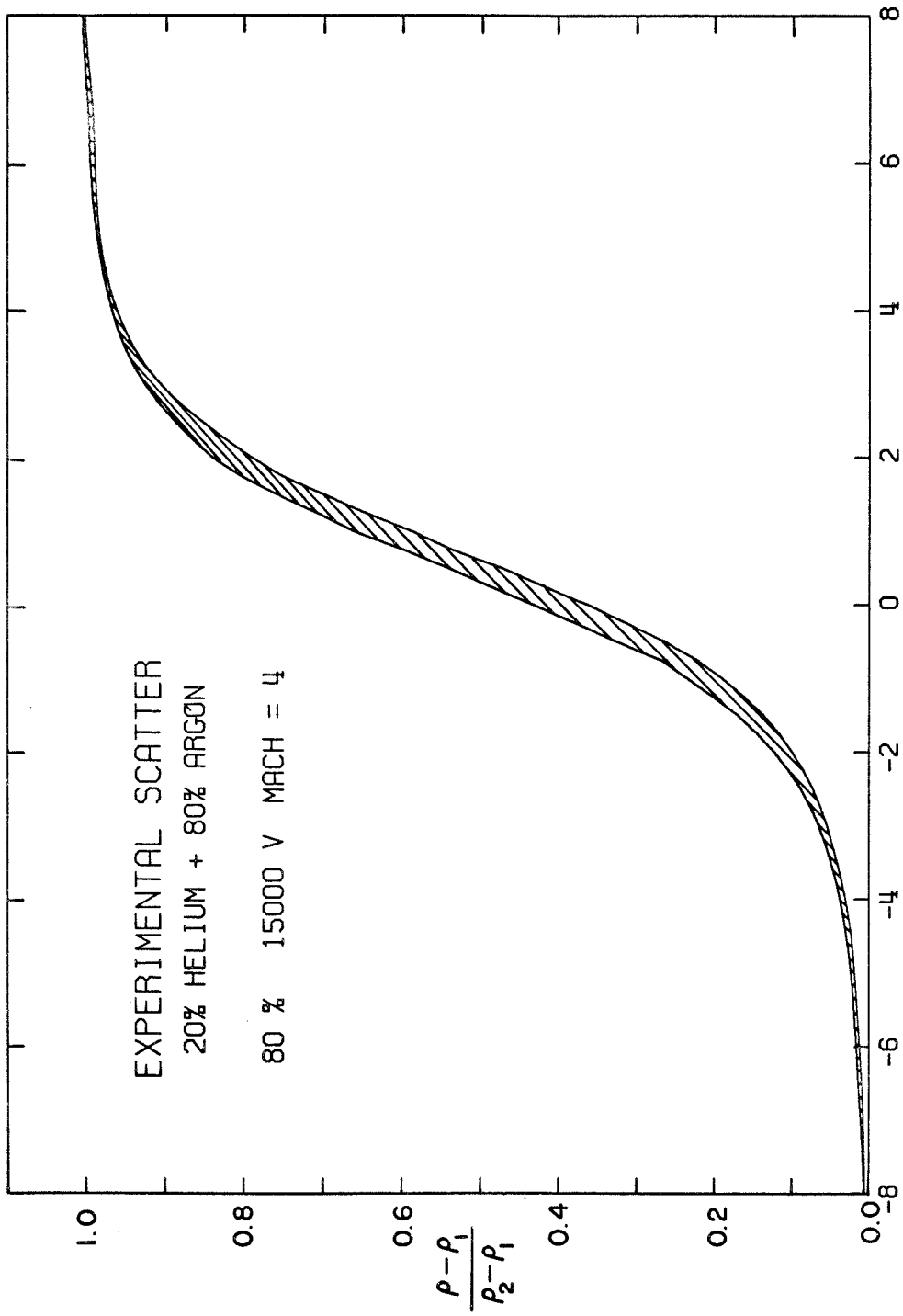
EXPERIMENTAL SCATTER
20% HELIUM + 80% ARGON
80 % 15000 V MACH = 4
1.0
0.8
0.6
0.4
0.2
0.0
$\frac{\rho-\rho_1}{\rho_2-\rho_1}$
-8
-6
-4
-2
0
2
4
6
8
$\frac{x}{\lambda_1}$

Figure 37

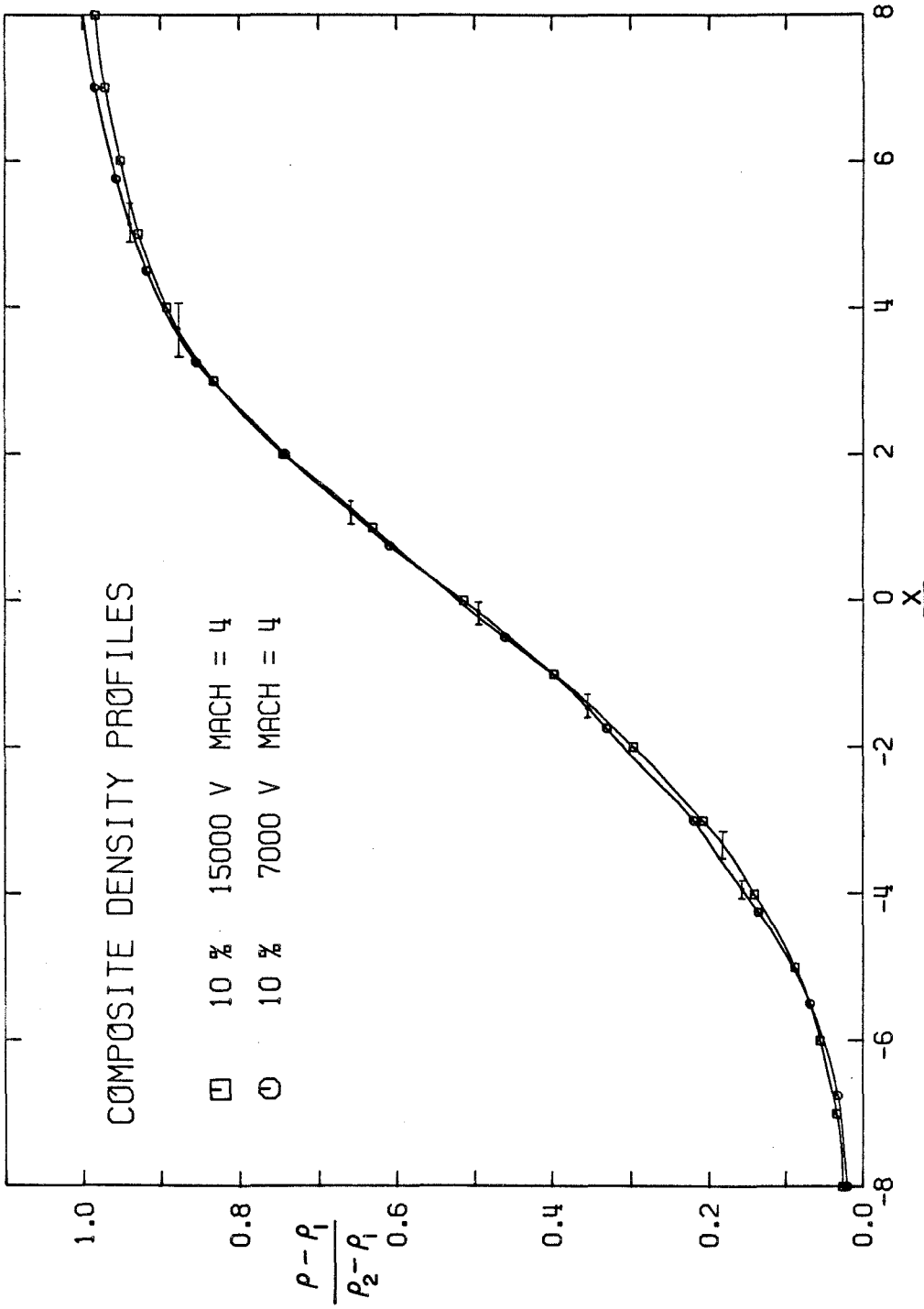
COMPOSITE DENSITY PROFILES
10 % 15000 V MACH = 4
10 % 7000 V MACH = 4
$\frac{\rho - \rho_1}{\rho_2 - \rho_1}$
$\frac{x}{\lambda_1}$
1.0
0.8
0.6
0.4
0.2
0.0
-8
-6
-4
-2
0
2
4
6
8

Figure 38

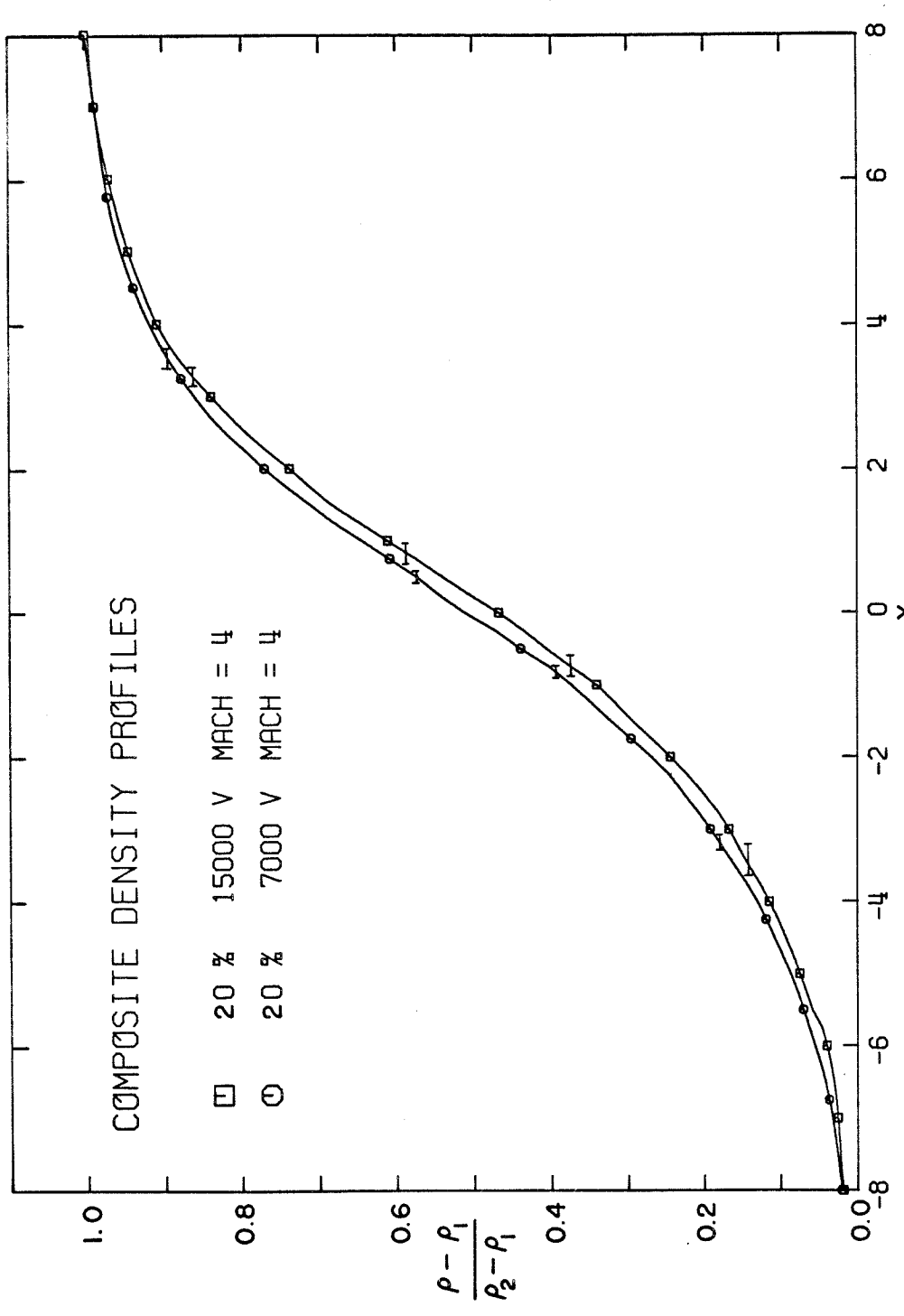
COMPOSITE DENSITY PROFILES
20 % 15000 V MACH = 4
20 % 7000 V MACH = 4
$\frac{\rho - \rho_1}{\rho_2 - \rho_1}$
$\frac{x}{\lambda_1}$
1.0
0.8
0.6
0.4
0.2
0.0
-8
-6
-4
-2
0
2
4
6
8

Figure 39

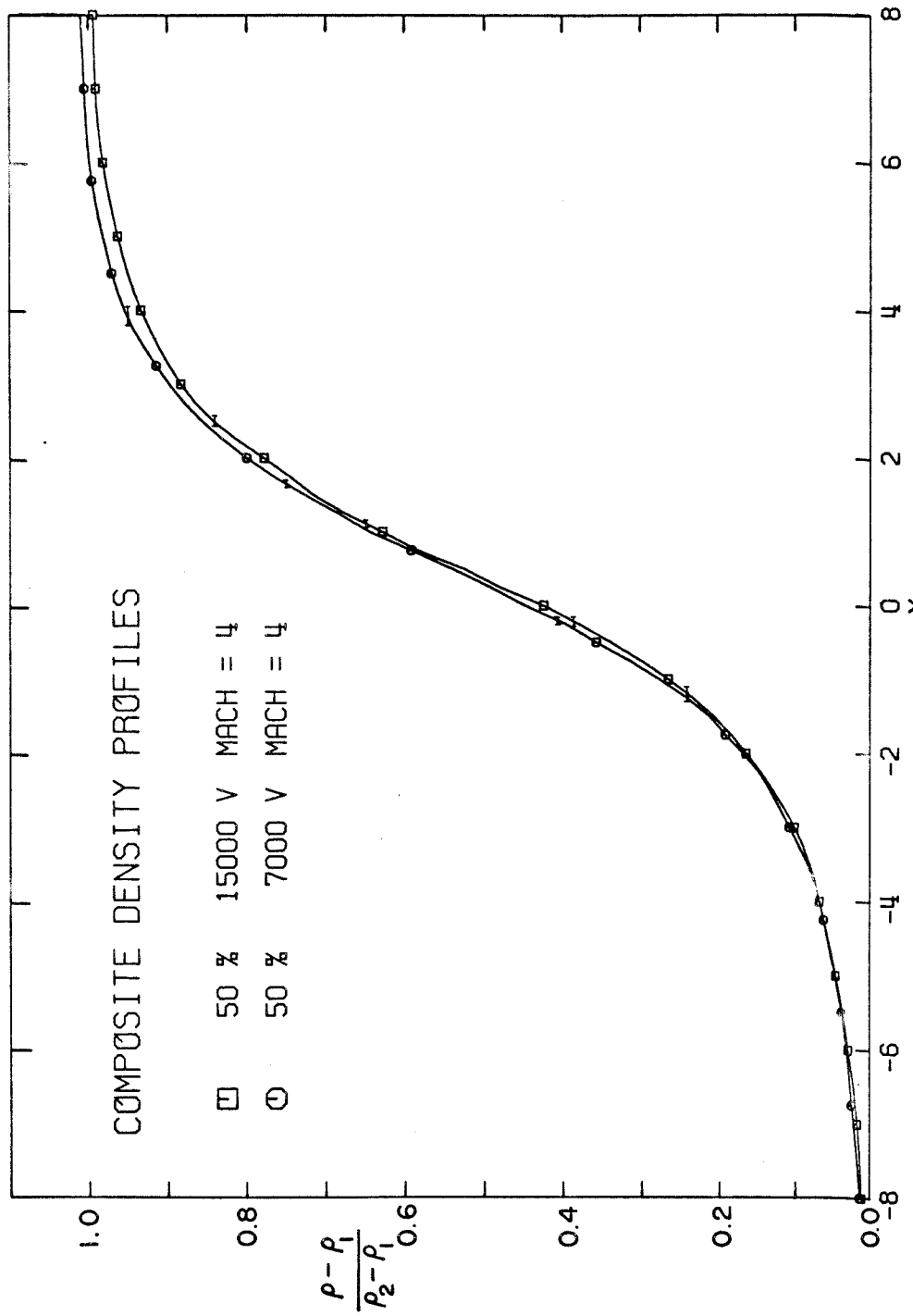
COMPOSITE DENSITY PROFILES
□ 50 % 15000 V MACH = 4
○ 50 % 7000 V MACH = 4
$\frac{\rho - \rho_1}{\rho_2 - \rho_1}$
$\frac{x}{\lambda_1}$
1.0
0.8
0.6
0.4
0.2
0.0
-8
-6
-4
-2
0
2
4
6
8

Figure 40

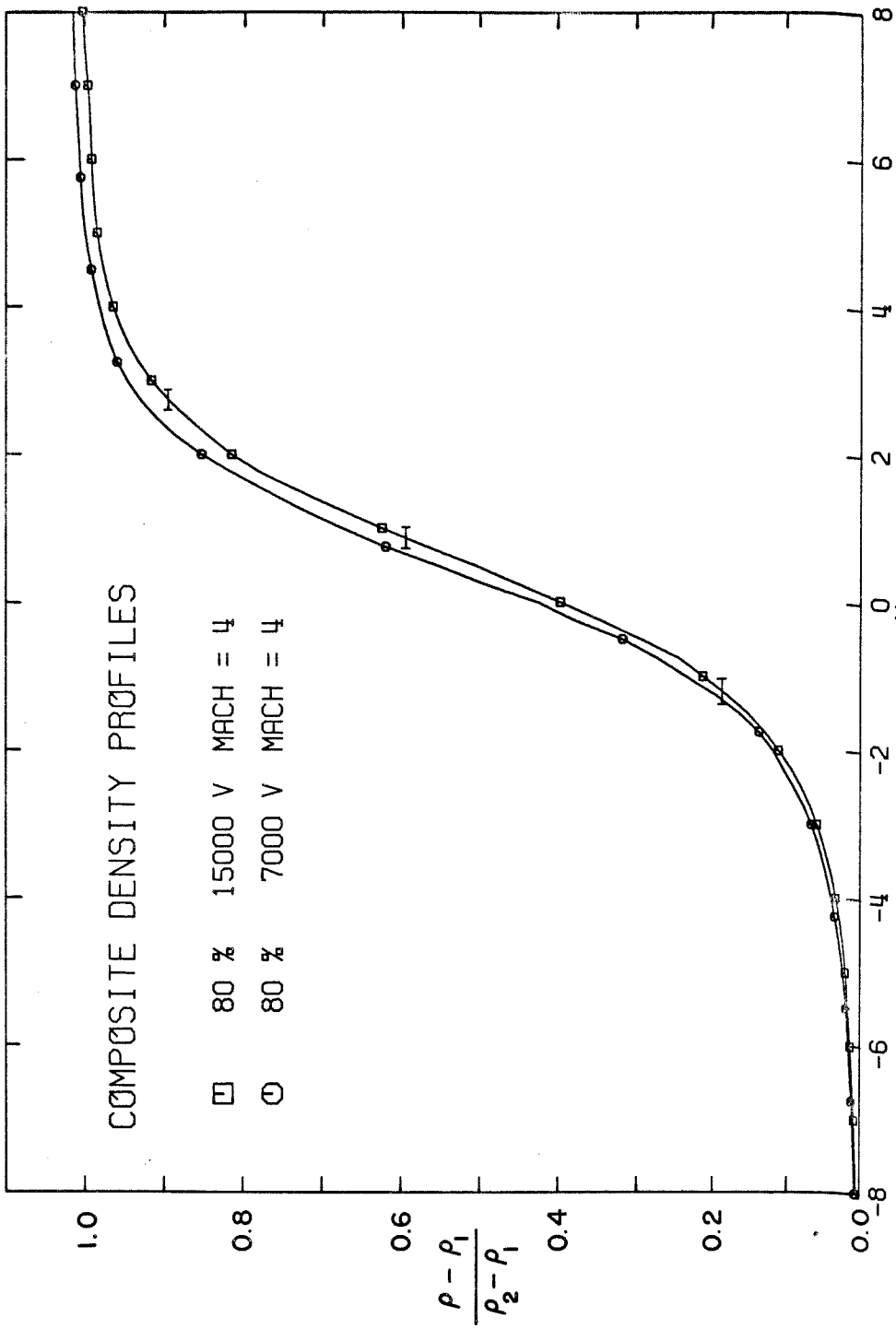
COMPOSITE DENSITY PROFILES
80 % 15000 V MACH = 4
80 % 7000 V MACH = 4
$\frac{\rho - \rho_1}{\rho_2 - \rho_1}$
$\frac{x}{\lambda_1}$
1.0
0.8
0.6
0.4
0.2
0.0
-8
-6
-4
-2
0
2
4
6
8

Figure 41

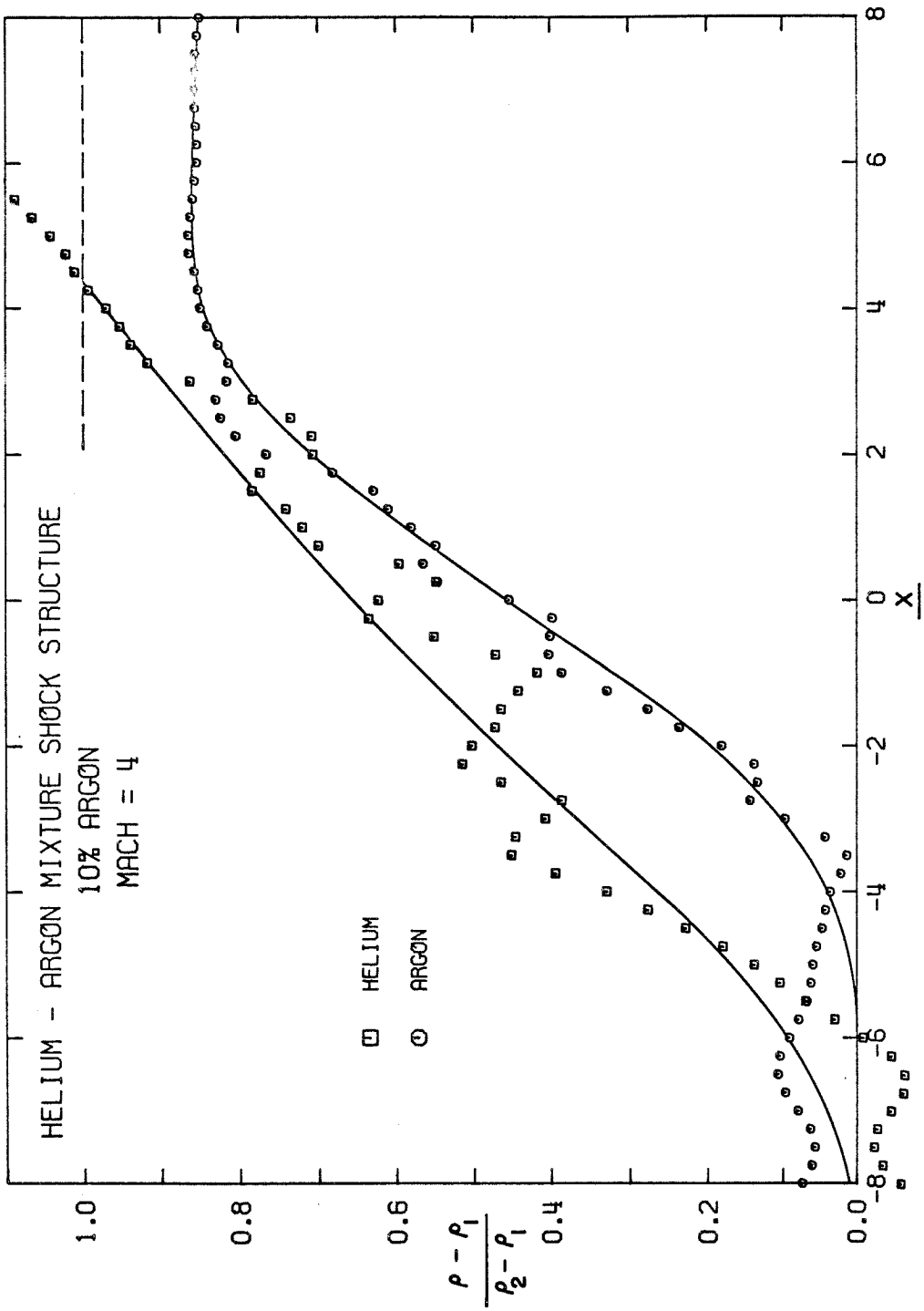
HELIUM - ARGON MIXTURE SHOCK STRUCTURE
10% ARGON
MACH = 4
HELIUM
ARGON
$\frac{\rho - \rho_1}{\rho_2 - \rho_1}$
$\frac{x}{\lambda_1}$
1.0
0.8
0.6
0.4
0.2
0.0
8
6
4
2
0
-2
-4
-6
-8

Figure 42

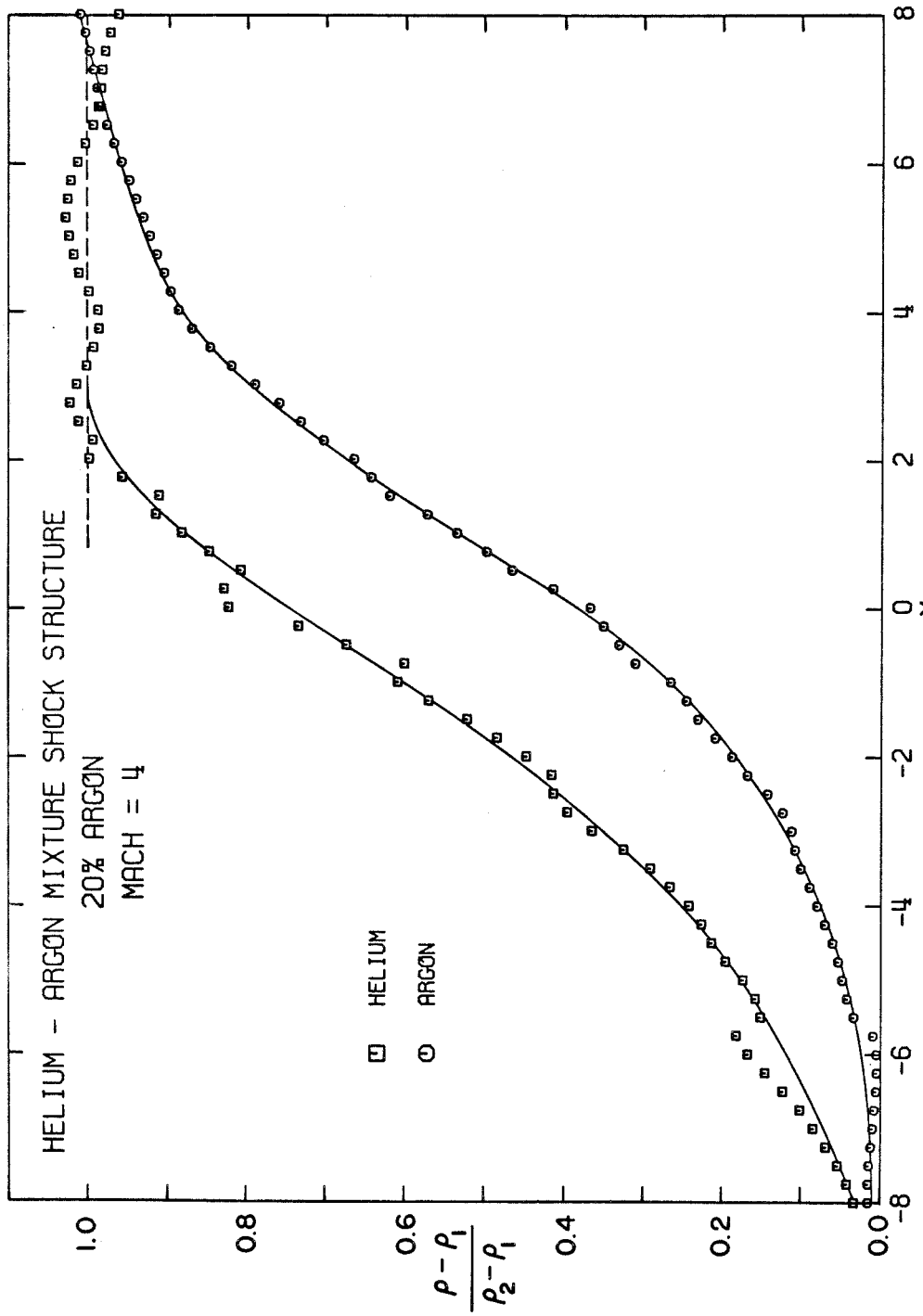
HELIUM - ARGON MIXTURE SHOCK STRUCTURE
20% ARGON
MACH = 4
HELIUM
ARGON
1.0
0.8
0.6
0.4
0.2
0.0
$\frac{\rho-\rho_1}{\rho_2-\rho_1}$
-8
-6
-4
-2
0
2
4
6
8
$\frac{x}{\lambda_1}$

Figure 43

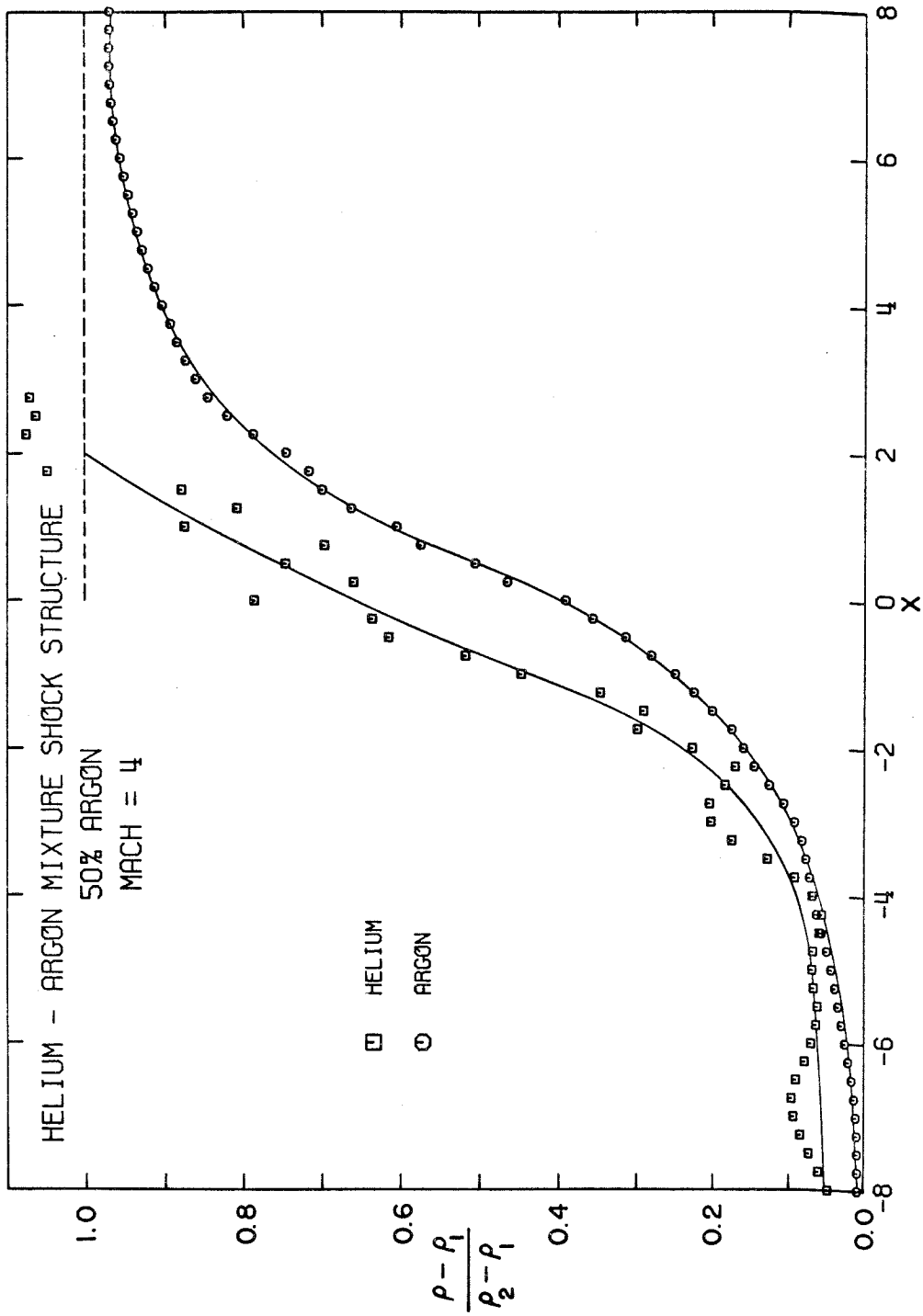
HELIUM - ARGON MIXTURE SHOCK STRUCTURE
50% ARGON
MACH = 4
HELIUM
ARGON
1.0
0.8
0.6
0.4
0.2
0.0
-8
-6
-4
-2
0
2
4
6
8
$\frac{\rho - \rho_1}{\rho_2 - \rho_1}$
$\frac{x}{\lambda_1}$

Figure 44

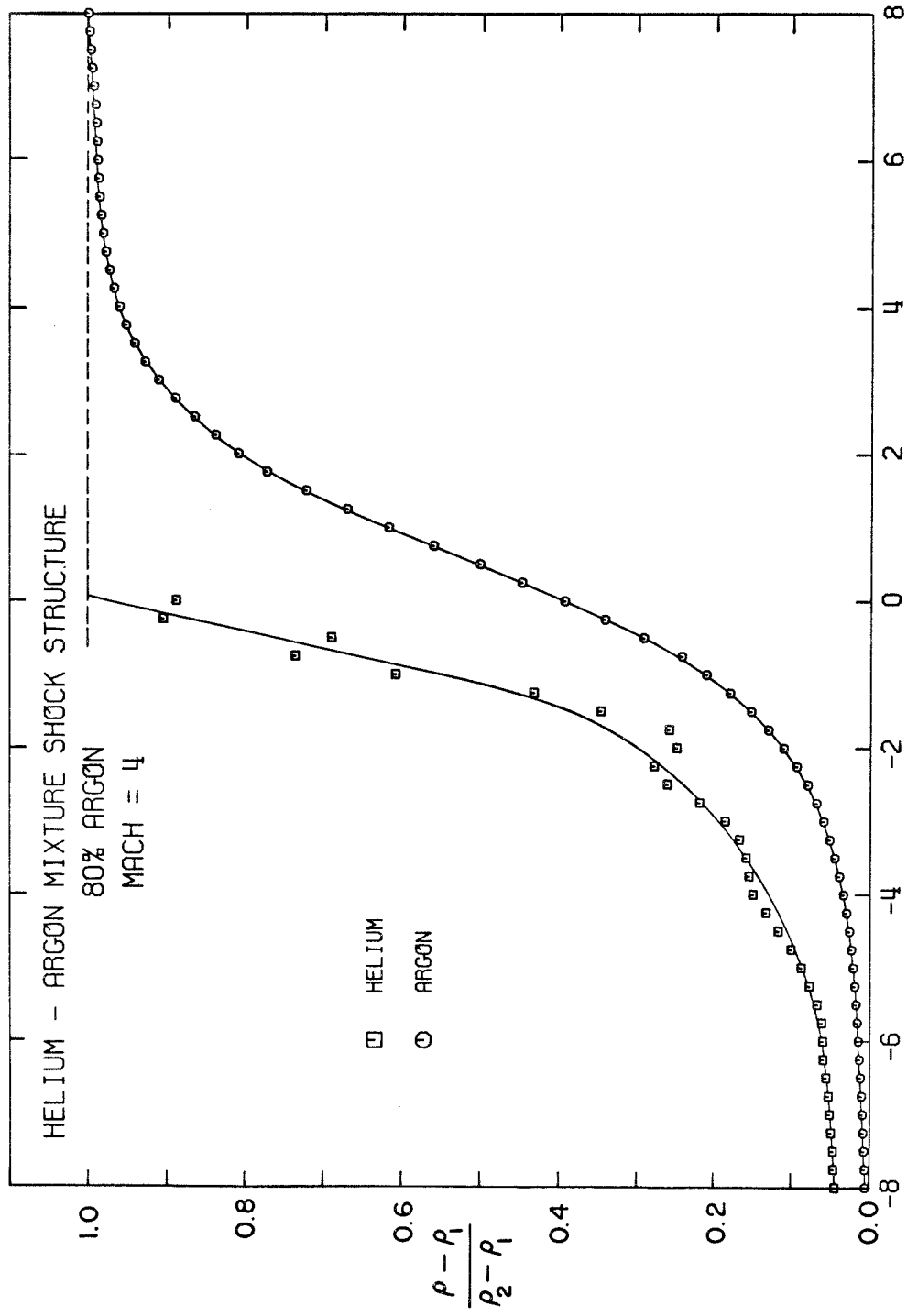
HELIUM - ARGON MIXTURE SHOCK STRUCTURE
80% ARGON
MACH = 4
HELIUM
ARGON
1.0
0.8
0.6
0.4
0.2
0.0
$\frac{\rho - \rho_1}{\rho_2 - \rho_1}$
-8
-6
-4
-2
0
2
4
6
8
$\frac{x}{\lambda_1}$

Figure 45